

Dissertation  
submitted to the  
Combined Faculties for the Natural Sciences and for Mathematics  
of the Ruperto-Carola University of Heidelberg, Germany  
for the degree of  
Doctor of Natural Sciences

presented by  
Xavier Heiligenstein

born in: Paris, France  
Oral-examination: .....

Electron microscopy and new technological approaches to investigate structural elements of the mitotic apparatus in *Saccharomyces cerevisiae* and *Xenopus laevis*

Referees:  
Dr. François Nédélec  
Prof. Dr. Oliver Gruss

***A ma Mamie***

*«L'esprit qui invente est toujours mécontent de ses progrès, parce qu'il voit au-delà.»*  
*Jean le Rond d'Alembert - Extrait de l'Encyclopédie*

# Acknowledgments

---

When I started my PhD, people told me: "it's a marathon, but you can't start gently". I wish I knew how hard this would be. The hardest part is that no matter how hard you work, it's never going to be enough. And that's exactly why you need to have help, support, trust and hope coming from outside, to help you believe in what you are doing. Through the successes and fails, these people keep believe in you and they bring you to the end.

Many people I met this past 4 years made it a nice journey for me. But most of all, I would like to thank Claude Antony, my supervisor who dared two times to trust in me. When I first sent him a mail, in 2005, I was looking for an internship for my fourth year of university and he gave me the chance to come, discover EMBL and electron tomography. He transmitted his passion to me and reinforced my will to do research. I had a wonderful time working with him and because of this, I applied to do my PhD two years later.

There, I got selected by Achilleas Frangakis who gave me the possibility to deeper understand and learn about the world of electron microscopy. Under the supervision of Ashraf Al-Amoudi, I became one of the few people able to handle the cryo-sectioning technique. He has been a great teacher and a great friend. Always present and answering questions, but also always happy to share a coffee and discuss about science, the world and joke about them.

At the time I started, Anne-Marie was finishing her PhD and Margot got started six month earlier. I think no one understands you better than someone who's on the same boat as you are.

Anne-Marie rapidly finished her PhD and moved far away from our lab, in the building next door but I still remember one of the first thing she told me when I presented my PhD project to the lab: "it is very nice for once to hear about real biology in this lab". It is true that the lab had mainly equations problems, eventually about biology. And thanks for this brunch, I owe you much!

Margot was doing stuffs that seemed complicated to me and after her first group-meeting, I felt lost. Actually, I still wonder how she can do what she is doing. Also b-dance. Margot have been around from the very beginning and until the very end. Discussions with her were always challenging and I'll always be in debts with her for writing me scripts in a way that I could somehow understand. So Margot, please keep your open heart and your smile as they are the sun you missed so much from SA.

Also from the Frangakis lab was the famous "Austrian crew". They were all very helpful and especially Mathias Mayr who did a lot of image processing for me. Trying all the various ideas I had regarding image processing of my cryo-electron tomograms. He was extremely patient and many tests wouldn't have been possible without him. Talking about programming, what would have been also the Frangakis lab without Dany and Sandra? Our Spanish representatives were also of a great support, personally, scientifically and

informatically. So were Mikhail and Anja, always here to propose solutions to my naive questions regarding biology or technique.

Then, came the time where I joined Claude's lab for the second time. Again, he opened his arm to me and entrusted me for the final 2 years of my PhD. What a challenge for both of us this Xenopus project... and what an exciting project. So many pitfalls were to be overcome but he always believed we could do it with Erin. Erin started the Xenopus project with me. Although it hasn't been always easy, she has been supportive and has accepted my moods. I haven't been an easy predoc to supervise, I admit.

From the team was also Sabine, the last representative of the "Austrian Crew". Her knowledge in microscopes and Imod were essential for this project and without her, we would still be wondering for many tomography problems. Uta, Rachel and Charlotta completed the EMCF with their kindness. Thank you so much you all 4 girls for being there.

I would also like to thank Christian Boulin, who believed in the risky cryo-capsule project, although it wasn't initially a biological project. He supported me and encouraged me to continue while supervising the developments of my third and last PhD project.

Gilles Régnier also was a key person in the cryo-capsule project and his support has been major to achieve the production of the cryo-capsule.

Et qu'aurait été cette deuxième moitié de doctorat sans Romain. Ta compréhension de mon sujet m'a toujours bluffée. Ton sujet était déjà suffisamment compliqué et tu réussissais encore à nous apporter des suggestions intéressantes sur le notre. Partager mon bureau avec toi aura été vraiment un plaisir quotidien. Ta bonne humeur, ton humour et ta patience à m'écouter râler m'auront été d'un grand secours. Merci sincèrement.

Ludo et Manu, merci aussi pour votre soutien. Nous n'aurons pas fait suffisamment de dîner ensemble au final, mais comme disais Ludo, c'était notre faute d'être expérimentalistes... Bah, on a survécu quand même.

I also would like to thank the predocs 2007 and the PhD program organisers; Milanka and Helke you were incredible, many thanks.

Mais arriver à l'EMBL pour faire un doctorat ne se fait pas comme ça. Il faut de nombreux amis qui vous soutiennent dans votre démarche. Les EPHYsards en font partie, et ce depuis le tout début, quand j'ai décidé de faire mon stage de M1 à l'EMBL : mon Vice-Préféré, Junior, Monsieur Meuble, Gaétan, Rouba et la p'tite Caro. Vous m'avez soutenu et cru en moi dans toutes mes entreprises et avez été source d'inspiration. Merci à vous tous.

Meinen « animaux allemands », vielen Dank an allem. Was für eine Witze den Bier und Wurst an meinem Geburtstag. Das war ihr alle zusammen: lustig und voll mit Energie, immer, irgendwie, irgendwo, irgendwann. Ich verspreche ihnen das ich werde mein Deutch noch mit euch verbessern!

Dam, je sais, faut qu'j'entre à Panam'. La Guilia nous attend et t'as les tan-gi. Merci pour tout. Ton soutien m'aura été précieux et ta façon de relativiser indispensable. J'boirais un coup à ta santé ce soir et embrasse meuf de ma part. T'inquiètes, j'entre bientôt.

Moune, ces derniers temps la Gelbique n'était plus sur ma route, mais Panam' le sera bientôt de nouveau. Alors à très bientôt.

Bérengère et Sébastien, ça va faire une éternité qu'on ne s'est plus vu. J'aurai dû rentrer plus souvent. Mais je vais y remédier. A très bientôt j'espère.

Amélie, Nolwenn, nous ne nous sommes pas beaucoup vu pendant ces 4 années, mais ce fût à chaque fois un plaisir renouvelé.

Enfin, il y a 4 personnes en particulier que je veux remercier :

Tout d'abord mes parents : ça n'a pas dû être facile pour vous ces 4 années. J'ai pas toujours été au mieux de ma forme et ça ne doit pas être facile pour des parents de voir le fiston à la peine. Mais c'est aussi grâce à votre soutien que ça a été faisable. Maman, merci d'avoir été si compréhensive et si patiente. Papa, on dit que l'expérience ne profite pas aux autres, la tienne m'aura été indispensable. Tu m'as permis de garder espoir sur mon troisième projet parce que tu y as encore plus cru que moi-même.

FA... que dire et par où commencer ? Je crois que je pourrai tout te résumer autour d'un gros Wopper, mais ici, je te dirais tout simplement merci du fond du cœur, pour ne pas réécrire une thèse entière.

E finalmente che devo dire a Claudia. Sempre con me, ache quando era difficile per te, tu sei con me. Tanti grazie et mile bacci, *p'tit machin*.

# Abstract

---

The mitotic cell cycle is a complex process which leads to the chromosome segregation from the mother cell to the two daughter cells and transmit the full genetic background necessary to grow and adapt to the permanently evolving environment. The equal partitioning of the duplicated chromosomes is finely regulated by the cytoskeleton which on purpose organises into a mitotic spindle. In eukaryotes like *Xenopus laevis* and *Saccharomyces cerevisiae* the mitotic spindle is mainly composed of three components: first the microtubules (MT) are organised in a spindle emanating from the chromosomes and focusing at the poles. Second they connect to the chromosomes via the kinetochore complexes (KT) and third focus at the microtubule organising centres (MTOC), also called centrosomes. We have focused our interest on structural analysis of the *S. cerevisiae* centrosome, called the Spindle Pole Body (SPB), at the molecular level, and on the MTs organisation in the meiotic spindle midzone of *X. laevis*.

With *S. cerevisiae* we have used cryo-electron tomography on vitreous sections (CETOVIS) to investigate the three dimensional (3D) molecular structure of the SPB. The samples were vitrified by high pressure freezing (HPF) and sectioned in vitreous state. Acquiring instant snapshots close to native state of the SPB in vivo, we confirmed previous observations done on plunge frozen or freeze substituted material. The Spc42 central crystal protein are organised with a defined spacing of 107Å, but the plaques composing the SPB could not all be identified. Mainly, the central and the outer plaque were visible, in contrast with the plastic tomography results where the inner plaque appeared dense and compact. Unfortunately, the very low signal to noise ratio prevented us from extracting details structural information about the SPB in its native state.

The project concerning the *X. laevis* meiotic spindle focused on the 3D organisation of the MT within the spindle. Their interactions with the MTOC and the KT have been extensively studied over the past, but a high resolution structural map is still missing and has long been awaited by scientists to put all the knowledge into a 3D context. Furthermore, information about the individual MT is missing like their average length distribution, the existence of short MTs and the end morphologies distribution. To study this complex and large structure, we have developed a novel correlative light to electron microscopy (CLEM) approach combined with electron tomography. We cryo-fixed by HPF, for the first time to our knowledge, spindle assembled in *X. laevis* egg extracts and prepared them for a structural electron tomographic study. We reconstructed three quarter of a meiotic spindle midzone and identified three subcategories of MT bundle organisation.

Finally, we have used our CLEM method to develop a new technology that should facilitate future CLEM work. Recent advances in plastic polymer transformation and micro-injection moulding ( $\mu$ IM) allowed us to create a cryocapsule designed for an easy correlative microscopy and transfer for HPF.

# Zusammenfassung

---

Der mitotische Zellzyklus ist ein komplexer Vorgang, der zur Aufteilung der Chromosomen von der Mutterzelle auf die beiden Tochterzellen führt. Er überträgt damit den vollständigen genetischen Hintergrund der notwendig ist um zu wachsen und sich an das ständig verändernde Umfeld anzupassen. Die gleichberechtigte Teilung der verdoppelten Chromosomen ist durch das Zytoskelett, das sich absichtlich in eine mitotische Spindel organisiert, fein geregelt. In Eukaryoten wie *Xenopus laevis* und *Saccharomyces cerevisiae* setzt sich die mitotische Spindel vor allem aus drei Komponenten zusammen: erstens die Mikrotubuli (MT) sind in einer Spindel, die von den Chromosomen ausgehen und sich an den Polen konzentrieren, organisiert. Zweitens sie verbinden sich mit den Chromosomen über die Kinetochor-Komplexe (KT) und drittens sie bündeln sich an den Mikrotubuli Organisationszentren (MTOC), auch Zentrosomen genannt. Wir haben unser Interesse einerseits auf die strukturelle Analyse des *S. cerevisiae* Zentrosoms, des so genannten Spindelpolkkörpers (SPB), auf molekularer Ebene, und andererseits auf die Organisation der MTs in der Mittelzone der meiotischen Spindel von *X. laevis* konzentriert.

Bei *S. cerevisiae* haben wir Kryo-Elektronen-Tomographie auf amorphen Dünnschnitten (CETOVIS) verwendet, um die dreidimensionale (3D) Molekularstruktur des SPB zu untersuchen. Die Proben wurden mittels Hochdruckgefrierens (HPF) in amorphes Eis eingebettet und anschließend in amorphe Dünnschnitte geschnitten. Anhand von Momentaufnahmen nah am nativen Zustand des SPB *in vivo*, konnten wir frühere Beobachtungen, die an schockgefrorenem oder gefriersubstituiertem Material durchgeführt wurden, bestätigen. Die Spc42 zentralen Kristallproteine sind mit einem definierten Abstand von 107 Å organisiert, aber die Platten, aus denen sich der SPB zusammensetzt, konnten nicht alle identifiziert werden. Hauptsächlich waren die mittlere und äußere Platte sichtbar, im Gegensatz zu den Kunststoff-Tomographie Ergebnissen, wo die innere Platte dicht und kompakt erscheint. Leider verhinderte das sehr niedrige Signal-zu-Rauschverhältnis einen Gewinn von detaillierten strukturellen Informationen des SPBs in seinem nativen Zustand.

Das Projekt über die *X. laevis* meiotische Spindel wurde auf die 3D-Organisation der MT in der Spindel ausgerichtet. Die Wechselwirkungen zwischen MT und MTOC und KT wurden ausführlich in der Vergangenheit studiert, aber eine strukturelle Karte mit hoher Auflösung fehlt noch und wird seit langem von Wissenschaftlern ersehnt, um all das Wissen in einen 3D-Kontext zu stellen. Darüber hinaus fehlen Informationen über die einzelnen MT, wie ihre durchschnittliche Verteilung der Länge, die Existenz kurzer MTs und die Verteilung der Endmorphologie. Zur Untersuchung dieser komplexen und großen Struktur, haben wir einen neuen korrelativen Licht-Elektronenmikroskopie Ansatz (CLEM) entwickelt, der mit Elektronentomographie kombiniert wird. Es war uns möglich, Spindeln die sich in *X. laevis* Eiextrakten geformt haben mittels HPF zu kryofixieren, was unseres Wissens nach noch niemandem vorher gelungen ist. Diese Spindeln wurden nach der Kryofixierung für eine strukturelle elektronentomographische Untersuchung aufbereitet. Wir rekonstruierten drei Viertel der Mittelzone einer meiotischen Spindel und identifizierten drei Unterkategorien von MT-Bündel Organisation.

Schließlich haben wir unsere CLEM-Methode verwendet, um eine neue Technologie zu entwickeln, die in Zukunft die CLEM Arbeit erleichtern sollte. Jüngste Fortschritte in der

Kunststoff-Polymer-Transformation und im Mikro-Spritzgießen ( $\mu\text{IM}$ ), erlaubten uns eine Kryokapsel für eine einfachere korrelative Mikroskopie und einen einfacheren Transfer für HPF zu entwickeln.

# Table of content

---

A-	Mitosis, Meiosis and Chromosome Segregation .....	18
a.	The cell and the cytoskeleton .....	18
b.	The mitotic spindle .....	19
c.	The microtubules and the dynamic instability .....	20
d.	The microtubule associated proteins and the motor proteins .....	21
e.	The microtubule organizing centres .....	24
f.	The kinetochores .....	28
g.	Cryo-immobilization of the biological specimens .....	29
h.	Correlative microscopy .....	30
B-	Material and Methods .....	34
a.	<i>Saccharomyces Cerevisiae</i> .....	34
i.	Yeast Culture .....	34
ii.	High pressure freezing with the Leica EMPACT2 .....	36
iii.	Cryo-ultramicrotomy on <i>in situ</i> spindle pole bodies .....	37
iv.	Spindle pole bodies purification, fixation and observation .....	40
v.	Cryo-electron imaging / data collection .....	40
vi.	Electron tomogram reconstruction with Alignator .....	42
b.	<i>Xenopus</i> spindle egg extract .....	42
i.	Meiotic spindle self-assembly in a cell free system .....	42
ii.	High-pressure freezing of <i>Xenopus</i> meiotic spindle .....	45
iii.	High pressure freezing with the Baltec HMP010 .....	52
iv.	Freeze substitution .....	52

v.	Ultramicrotomy .....	53
vi.	Data collection .....	55
vii.	Electron tomogram reconstruction with the IMOD suite.....	59
viii.	Microtubules Modeling.....	62
C-	The Mitotic spindle in <i>Saccharomyces cerevisiae</i> .....	69
a.	The mitotic spindle is organized by the Spindle Pole Body .....	69
i.	The Spindle Pole Body structure .....	69
b.	Detailed observation of the wild type: the first step towards high resolution of molecular complexes' interactions.....	73
i.	Wild type cell synchronization with $\alpha$ -factor .....	73
ii.	Thermo-sensitive mutant synchronization by temperature shift.....	73
iii.	Cell behaviour in cryo-protectant solution.....	75
c.	Data collection.....	77
i.	Choice of the HPF .....	77
ii.	Grid selection.....	77
d.	The use of mutants to observe selected time points in the cell cycle .....	79
i.	Cdc20 mutant .....	79
ii.	Cdc4 mutant, one mutant to bind them all.....	80
e.	Tomographic results.....	81
i.	Cryo-electron tomograms from CEMOVIS sections .....	81
f.	Plunge freezing of isolated of SPBs or Nucleus.....	87
g.	Discussion.....	88
D-	The meiotic Spindle in <i>Xenopus laevis</i> .....	94
a.	The Meiotic spindle self assembly in the egg extract .....	94
b.	High Pressure Freezing of an in vitro system sensitive to pressure.....	96
c.	Identification of the spindles.....	98

d.	Selection of the acquisition parameters .....	99
e.	Data acquisition of the midzone of a precisely identified spindle .....	100
i.	The correlative microscopy proof of principle .....	100
ii.	Montaging and joining of the tomograms .....	102
f.	Acquisition of the full spindle.....	113
i.	Super montaging at low magnification .....	113
g.	Summary of the biological outcomes and interpretation/discussion .....	115
h.	Perspectives.....	124
E-	The cryo-capsule: a new versatile tool to facilitate correlative microscopy approaches.	127
a.	Introduction.....	127
b.	The design .....	129
c.	The material selection.....	130
d.	Cell growth .....	131
e.	Correlative microscopy.....	131
f.	High Pressure Freezing.....	132
g.	Physical properties of the material used in the cryo-capsule.....	134
h.	Conclusion and perspectives.....	136
F-	General discussions on the three projects, their limitations and their potential .....	139
G-	Bibliography.....	142
H-	Table of Illustrations:.....	153



# List of abbreviations

---

μIM: micro-injection moulding	128
AFS1: automated freeze substitution 1	52
BSA: bovine serum albumine	36
<i>C.elegans: Caenorhabditis elegans</i>	24
CCD camera: charge-coupled device camera	55
cMT: cytoplasmic microtubule	25
cMTs: cytoplasmic microtubules	69
CP: central plaque	25, 69
DNA: deoxyribonucleic acid	28
EB1: end binding protein 1	95
EM: electron microscopy	28
EtOH: ethanol	37
FEG: field emission gun	55
FRET: Förster resonance energy transfer	71
FS: freeze substitution	31
FS1: freeze substitution 1	52
FS2: freeze substitution 2	52
Gb: gigabyte	118
GDa: giga dalton	69
GDP: guanosin diphosphate	95
GTP: guanosin triphosphate	95
H <sub>2</sub> O: distilled water	34
HB: half-bridge	25, 69
HCl: hydrochloric acid	45
HDPE: High Density Polyethylene	130
HPF: high pressure freezing	29
HxD: hexadecene	46
IP: inner plaque	25, 69
kMT: kinetochore microtubule	19, 27

KT: kinetochore	19
LC: lead citrate	54, 99
LEU: leucin	35
MAPs: microtubule associated proteins	69
MMR: Marc's modified Ringer solution	43
MTOCs: microtubule organizing centers	18
MTs: microtubules	18
NaOH: sodium hydroxide	46
nMT: nuclear microtubule	26
NuMA: nuclear mitotic apparatus protein	23
OD: optical density	34
OP: outer plaque	25, 69
PBS: phosphate buffered saline	36
PhChl: phosphatidylecholine	46
PLL: poly-L-lysine	35
PMSF: phenylmethanesulfonylfluoride	35
ROI: region of interest	65
RTS: rapid transfer system	31, 35, 90
<i>S.cerevisiae</i> : Saccharomyces cerevisiae	19
<i>S.pombe</i> : Schizosaccharomyces pombe	23
SPB: spindle pole body	24
tMTs: triplet microtubules	25
ts: thermo sensitive	34
UA: uranyl acetate	54, 99
Ura: uracil	34
WT: wild type	34
<i>X.laevis</i> : Xenopus laevis	31
YNB: yeast nitrogen base	34
YPAD: yeast peptone dextrose adenine-supplemented	34

# General introduction

---

## A- Mitosis, Meiosis and Chromosome Segregation

### a. The cell and the cytoskeleton

Cells are the smallest autonomous living entity. They are able to perform an incredible amount of functions by finely regulating themselves according to the environment and to adapt constantly to the various changes occurring in it. In order to survive and to generate progeny, cells need to transmit genetic information to the following generation. The cell cycle is a biological process by which a mother cell divides to generate two daughter cells with equivalent genetic background. The process by which a cell generates two clones of itself is called mitosis and is tightly regulated by complex machinery composed of key molecular players and sub-cellular elements that are cell cycle dependent. The molecular pool that takes part in structural and regulatory elements of the cell life cycle and division is the cytoskeleton. The cytoskeleton is a highly dynamic “scaffold” on which organelles are supported to organize the cell according to the biological needs. Upon mitosis, a dramatic and rapid, yet finely regulated, remodeling of the cytoskeleton occurs to trigger the segregation of the duplicated genetic material (the chromosomes) *via* a specific structure called the mitotic spindle. This mitotic spindle apparatus is mainly composed of: microtubules (MT), microtubule organising centres (MTOC or centrosomes in vertebrates, Spindle Pole Body in yeast), actin and mechanical binders (motor proteins and bundlers).

The cytoskeleton is composed of three fundamentally different sub-classes of filamentous structures: first the actin filaments, historically called microfilaments are localised throughout the whole cell to support the cell shape and the membrane dynamics. The second class, called intermediate filaments, is composed of various filaments types: vimentins, keratins and lamins. The third class, which concerns the second focus of this thesis work, involves larger structures called the microtubules (MTs). The MTs are polymeric hollow tubes, largely involved in the mitotic spindle. In the mitotic context, these MTs are able to selectively load the chromosomes (prophase to metaphase) through molecular focal scaffold (kinetochores) and then to segregate them after duplication (anaphase). Cell cycle checkpoints coordinate the mitotic process to fine regulate the highly dynamic prone nature of the MTs into coherent segregating machinery. The MTs are mainly centrally organised during the mitotic process by the so called microtubule organizing centres (MTOCs) which greatly vary in shape among the eukaryote realm despite a strong functional redundancy. I

will elaborate on the specific composition and architecture of the MTOC from the budding yeast, *Saccharomyces cerevisiae* (*S.cerevisiae*), in the first chapter of this thesis.

### **b. The mitotic spindle**

The mitotic spindle is mainly composed of MTs, organised around the chromosomes in a poleward orientation and focused at the poles around the MTOCs. Its function consists of segregating the duplicated chromosomes during anaphase. They overlap in an anti-parallel fashion at the centre of the spindle and can be differentiated from each other by their function. The first category is composed of structural MTs. Generally focused at the poles around the MTOCs, they interact at the spindle midzone with the MTs from the opposite MTOC. The interaction is done *via* motor proteins that connect them in an anti-parallel way. The MTs arising from a common MTOC often interact via bundling proteins to form robust structures: the MT bundles. A second class of MTs, called kinetochore MTs (kMTs), emanates from the MTOC and interacts directly with the chromosome centromeres via the kinetochore complexes (KT). They serve as tension sensors during metaphase to assess the proper amphitelic attachment of the chromosomes towards each opposite pole. Later in anaphase, MT depolymerization exerts pulling forces towards each MTOC and attracts the individual duplicated chromosome to the future daughter cell. A third category of MTs are radial sensors of the cell and orientate the spindle within in the cell <sup>1-3</sup>. All these three MT sub-populations however are not static but highly dynamic during mitosis. Moreover, the spindles greatly vary in size depending on the species. Larger structures are reinforced by bundling of parallel MTs via MT bundlers which might impact the overall physiognomy of the mitotic spindle.

Despite the three main actors of the mitotic spindle, namely the MTOC, the MTs and the Chromosome mass, studies have been conducted to show that the MTs are able to self organize, given the right motor proteins, into a spindle like structure <sup>4-6</sup>. The use of chromatin beads lacking centromeric regions is sufficient to generate a spindle like structure via cytoplasmic dynein-dependant translocation of MTs and the MTOC are dispensable in the spindle generation process <sup>7,8</sup>. The spindles can therefore auto assembly by self-organization, lacking the MTOCs and the KTs by the sole presence of MTs and motor proteins.

### c. The microtubules and the dynamic instability

The fundamental unit of the spindle is the MT. It results from the assembly of dimers of tubulin  $\alpha$  and  $\beta$  in a head to tail fashion to form individual protofilaments. During polymerization, tubulin dimers are added to the MT end. The  $\gamma$ -tubulin protein complex ( $\gamma$ -Tub) initiates a 13 protofilament lattice<sup>9,10</sup>. The  $\gamma$ -Tub is a capping and an anchoring appendage of the MT minus end and is the main nucleator for MT polymerization<sup>11</sup>. The MT elongates from a sheet like form to close into the hollow cylindrical structure of the MT<sup>12</sup>. The 13 protofilaments MTs are the majority of *in vivo* MTs and have an inner diameter of 18nm and an outer diameter of 25nm<sup>13-15</sup>.

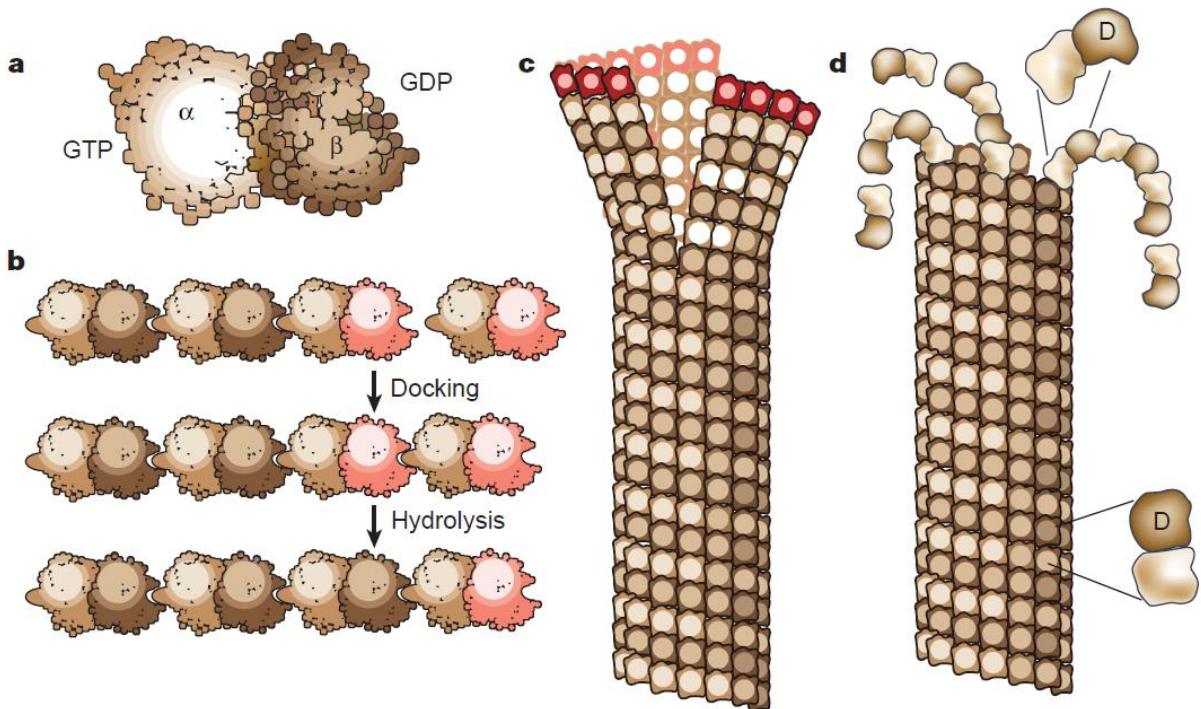


Figure 1 : Schematic view of the polymerization and depolymerization of a MT plus end<sup>16</sup>

The MT is characterized by different biological states which refer to the dynamic of the MT within a given time frame. First, the growth phase is characterized by a rapid extension of the MT and fast adjunction of GTP-tubulin dimers at their plus end where they are hydrolysed shortly after incorporation. Second, the shrink phase is characterized by the rapid subtraction of the GDP-tubulin dimers from the MT. Finally, the third stage, called rescue, corresponds to a re-growth of the MT by new polymerization. Those three stages are

happening mainly at the plus end of the MT while the minus end is often capped and stabilized by the  $\gamma$ -Tub.

The rapid change of the MT dynamic between these three stages is the dynamic instability. Constantly happening within the spindle throughout the whole mitosis, it confers to the structure a very good adaptability and plasticity<sup>16-19</sup>, yet conserving a global stability.

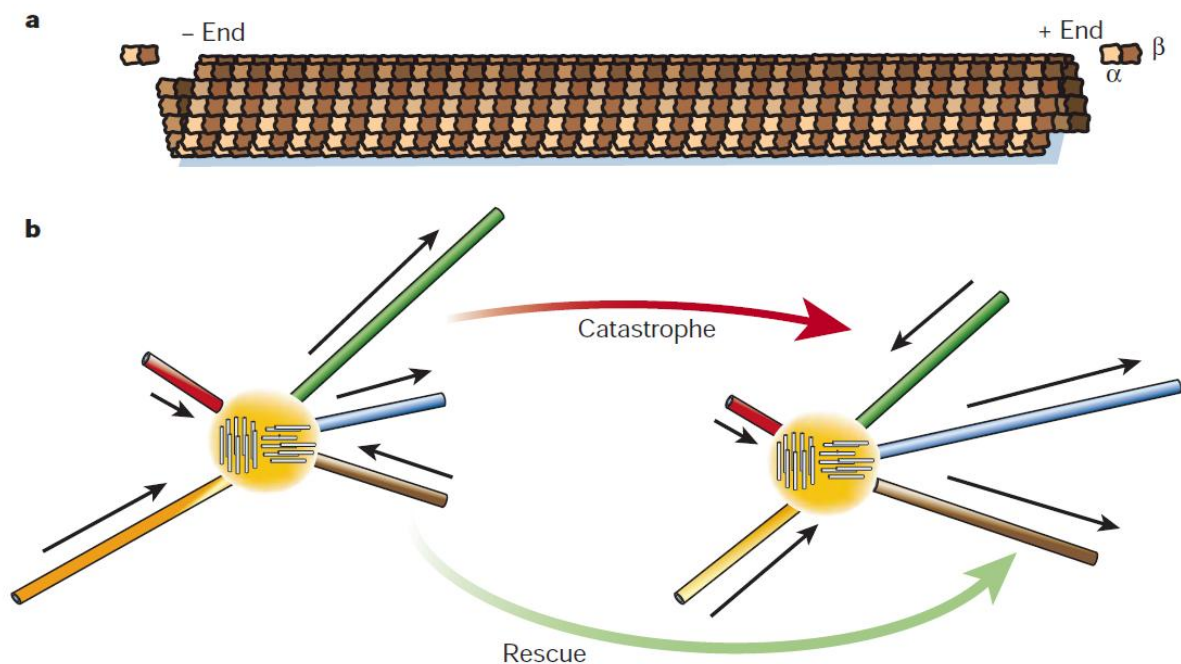


Figure 2 : Schematic view of a MT and its dynamic states<sup>16</sup>

The dynamic instability is constantly happening *in vitro* and *in vivo*. The rates of polymerization, depolymerization, the frequency of catastrophe and of rescue define the four parameters of the dynamic instability. These parameters are then modulated by microtubule associated proteins (MAPs) which stabilize or destabilize MTs, alter their speed of growth or shrinkage and mediate interactions with other cellular components. These MAPs regulate the global dynamics of the spindle, acting on single MTs, in response to regulatory signals during the cell cycle.

#### d. The microtubule associated proteins and the motor proteins

The spindle, composed of highly dynamic MTs, evolves in coordination with the cell cycle. To achieve a fine regulation on a large scale of all the MTs, microtubule associated proteins (MAPs) act on the individual MTs. The MAPs can be classified according to their functions

and properties. Five main groups can be defined: stabilizing MAPs, destabilizing MAPs, nucleating MAPs, motor proteins and bundling proteins.

Stabilizing MAPs, like XMAP215, stimulates the growth of the MT plus end and suppress the MT catastrophe. 60% inhibition of this protein leads to shorter and more dynamic MTs and total inhibition prevents MT growth at all <sup>20-22</sup>. This MAP also is part of the MTOC components and is necessary to grow MTs into asters <sup>23</sup>. This MAP is working in equilibrium with XKCM1, a depolymerization MAP. XKCM1 contains a catalytic domain that actively induces the catastrophe of the MTs. Like its human homologue MCAK, it localizes at the KT and plays a role in chromosome movements in the mitotic spindle <sup>24</sup>.

Similarly, Patronin (*ssp4*) protects the minus ends of the MTs from the depolymerization activity of the Kinesin-13. Patronin loss of activity triggers loss of tubulin subunits from the minus end of the MT, traditionally considered the least dynamic of the two ends of the MT, and leads to short disorganized mitotic spindles <sup>25</sup>.

During mitosis, MAP activity is driven to increase the dynamic of the MTs and shorten their length <sup>26</sup>. The decrease in MT length releases free tubulin and improves the ability of the cell to nucleate MTs, therefore increases the dynamic of MTs.

Other proteins, like TPX2 act as nucleating and stabilizing MAPs. Initially identified as the targeting protein for the plus end directed kinesin Xklp2 <sup>27</sup>, it is also involved in the spindle pole organisation <sup>28</sup> and the MT stabilisation through bundling of prepolymerized MTs *in vitro* <sup>29</sup>. It is also a RanGTP target responsible for chromosome-dependent and centrosome-independent MT nucleation <sup>30-33</sup>, giving insights into the formation of spindles in the absence of chromosomes <sup>8</sup>.

Finally, motor and bundling proteins are the MAPs that organise the MTs towards each other. Motor proteins are motile MAPs, able to transport cargos by a “walking” mechanism on the MT lattice, using ATP hydrolysis as energy. Motor proteins, according to their structure are able to transport proteins, vesicles and also to bind to other MTs. Kinesin like MAPs are generally composed of two arms linked together at the ends of which are located globular domains. These globular domains have a high affinity with the tubulin lattice of the MT when loaded with ADP. After binding to the MT lattice, ADP is released and replaced by

ATP. The presence of ATP changes the configuration of the globular domain and moves forward the second globular domain linked via the arm. This second globular domain, loaded with ADP will bind to the MT lattice. Hydrolysis of the ATP from the first globular domain relaxes the attachment while the second globular domain is loaded with the ATP like the first globular domain. By repeating this series of events, the motor protein moves forward in the direction of the MT plus end <sup>34</sup>. These motors are selectively progressing in a preferred orientation towards either the plus or the minus end of the MTs.

In the kinesin family, some MAPs are minus end directed proteins while other are plus end directed. The sub-classification of these kinesins is according to their molecular structure (N or C-terminal kinesins, internal motor domains and orphans). Eg5 is a tetrameric MAP with and N-terminal kinesin domain <sup>35-37</sup>. Eg5 cross-link MTs <sup>38</sup> and initiate an anti-parallel sliding essential to the establishment and preservation of a bipolar mitotic assembly <sup>5,39</sup>.

Dynein is a very well characterized minus end directed motor protein and is a component of a large multi-subunit complex involved in the orientation of the mitotic spindle <sup>40</sup>. Its structure is divergent from the kinesin like proteins beside a similar function.

Finally, bundling proteins like Ase1 in *Schizosaccharomyces pombe* (*S.pombe*), are responsible for spacing of the MTs within the cell <sup>41</sup> and help organizing the spindle structurally.

The interplay of all the motor proteins and bundling proteins establish a bipolar spindle (Eg5, Xklp2), contribute to the focussing of the MTs at the poles (dynein, nuclear mitotic apparatus protein: NuMA), organise the MTs cross-linking and overlapping at the midzone of the spindle *via* MTs plus ends and mediate the MT-chromosome interactions <sup>7</sup>.

Motor-based mechanisms of spindle assembly		Molecular motors	Localization (in red)	Proposed role	Inhibition phenotypes
Spindle bipolarity		Kinesin-3 (+) Klp38B (fly)		Connects spindle MTs to chromosome arms; promotes spindle stability	MONOPOLAR SPINDLE
		Kinesin-4 (+) Xklp1 (frog), Klp3A (fly)		Crosslinks MTs and slides antiparallel MTs outward	HALF SPINDLE
		Kinesin-5 (+) Eg5 (frog, human) Kip61F (fly)		Regulates MT dynamics and spindle stability	
Spindle pole formation		Kinesin-13 (i) Klp10A (fly) Kif2a (frog, mouse, human) Kif2b (human)		Depolymerizes MTs at spindle poles	LONGER SPINDLE
		Kinesin-14 (-) Ncd (fly) XCTK2 (frog) CH20 (hamster) HSET (human)		Slides MTs poleward; exerts antagonizing force against Kinesin-5	LOSS OF CENTROSOMES SPLIT/PLAYED POLES
		Dynein (-) (fly, frog, mouse, human)		Slides MTs poleward; generates cortical pulling force	
Chromosome positioning		Kinesin-4 (+) Klp3A (fly) Xklp1 (frog)		Promotes kinetochore-MT attachment	KINETOCHORE MISALIGNMENT, MISORIENTATION
		Kinesin-10 (+) Nod (fly), Kid (human)		Attaches chromosome arms to spindle and slides toward center	
		Kinesin-7 (+) CENP-E (mouse, human) CENP-meta (fly)		Slides unattached kinetochores along a K-fiber toward spindle center	MISALIGNED CHROMOSOME ARMS
		Kinesin-8 (+, i) Klp67A (fly) KIF18A (human)		Dampens kinetochore oscillations	
		Kinesin-13 (i) Klp59C (fly) MCAK (frog, human)		Depolymerizes kinetochore MTs	BENT SPINDLE

**Figure 3 : Motor Proteins in Spindle Assembly are involved mainly in three different activities for the spindle assembly: the bi-polarity establishment, the spindle pole formation and the chromosome positioning. The fine regulation of all these actors permits a dynamic remodeling of the spindle along with the cell cycle** <sup>42</sup>.

Several molecular motors interplay to coherently organize the spindle and act on the MT growth behaviour to regulate them. These motor proteins have their homologues in yeast but are often associated to the Spindle Pole Body (SPB: the yeast MTOC equivalent) or are attached directly to the MTs and therefore not freely moving within the cell <sup>43</sup> like in the larger *X. Laevis* mitotic spindle.

### e. The microtubule organizing centres

To organize the polymerisation, stabilisation and organisation of all the MTs, many eukaryotic cells are using a MTOC, also called centrosome. In vertebrates or in *Caenorhabditis elegans* (*C.elegans*), the centrosome is composed of one to two centrioles, according to the cell cycle phase. In yeasts, the MTOCs equivalents are the spindle pole bodies (SPBs). In higher eukaryotes, the centrioles are usually composed of singlet, doublets or triplets of MTs, radially arranged with nine fold symmetry <sup>44,45</sup>. They are surrounded by amorphous electron dense protein rich matrix called the peri-centriolar material (PCM) that contains several proteins, including  $\gamma$ -TuRC complexes which are mainly responsible for MT nucleation. It is localised in the cytoplasm during the whole cell cycle and the two duplicated

centrosomes migrate to each pole of the nucleus when the nuclear envelope breaks down to organize the mitotic spindle <sup>44,46,47</sup>. It usually measures 0.5 $\mu$ m long and 0.2 $\mu$ m in diameter (Figure 4). The MTOC serves as a signalling platform during the cell cycle, but can also be used to regulate the cell motility, adhesion and polarity in interphase. A miss-regulation of the MTOC duplication might lead to aberrant spindle organisation and chromosome segregation, until abnormal cell division and cancer. The duplication occurs at one end of the centriole, along with the cell cycle regulation, and a new centriole (daughter) is orthogonally assembled to the mother centriole in a conservative way, once per cycle. The newly formed centriole then separates from the mother centriole during mitotic exit. During S phase, the centrioles independently duplicate and the procentrioles elongate until mitotic entry and centrosomes separation to each pole of the spindle.

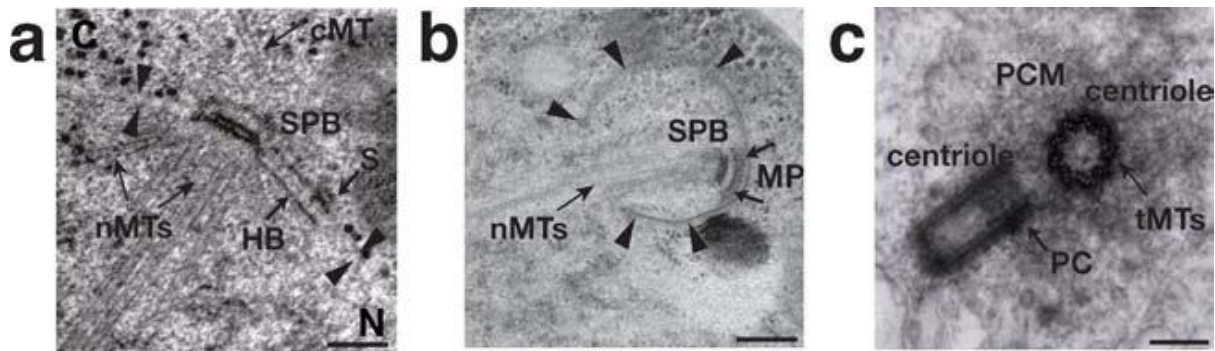


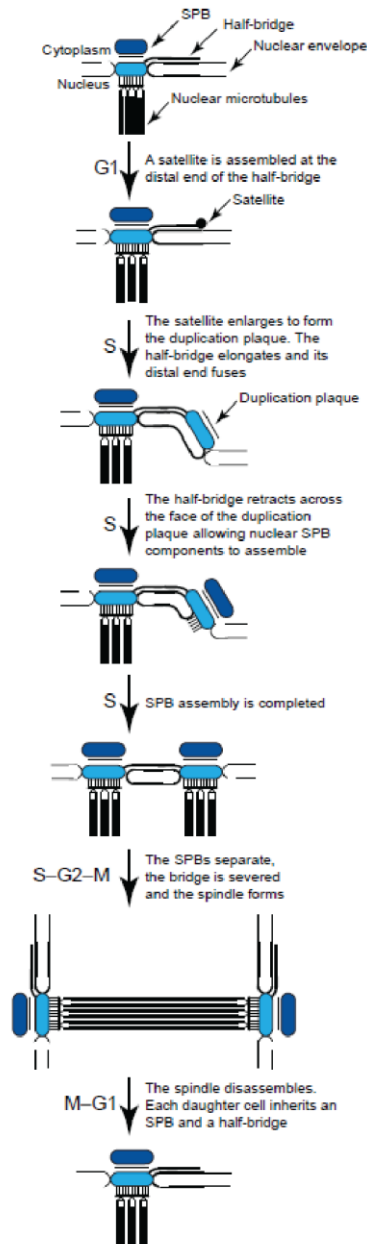
Figure 4 : The SPB is a multi-layered organelle that is morphologically distinct from the centrosome. (a) A thin-section electron micrograph shows the layered SPB structure. It is embedded in the nuclear envelope (arrowheads), which separates the nucleus (N) and cytoplasm (C). The half-bridge (HB) containing a satellite (S) can be seen associated with the SPB. The positions of nuclear (nMTs) and cytoplasmic (cMTs) MTs are also indicated. Scale bar, 0.1  $\mu$ m. (b) A thin-section electron micrograph of a meiosis II SPB shows the modified OP (MP, arrows), which is required for prospore membrane formation (arrowheads). nMTs that form the meiosis II spindle are also indicated. Scale bar, 0.1  $\mu$ m. (c) An EM image of a centrosome shows it is composed of two orthogonally oriented centrioles, seen here in transverse- (left) and sagittal- (right) sections. The position of procentriole (PC) assembly is indicated. Centrioles are formed by assembly of triplet MTs (tMTs) and are associated with peri-centriolar material (PCM). Scale bar, 1  $\mu$ m. Reprinted from (Giddings et al. 2001, Rieder et al. 1994), with permission from Elsevier. (figure 1 from <sup>48</sup>).

In yeasts the closed mitosis requires the inclusion of the SPB into the nuclear membrane. The SPB in the case of *S.cerevisiae* has the peculiarity of being embedded into the nuclear envelope during the whole life cycle. It is mainly composed of three layers connected with each other. The so called outer-plaque (OP) faces the cytoplasm and organizes the cytoplasmic MT (cMT) polymerization. The central plaque (CP) is located at the level of the nuclear envelope and links the outer plaque (OP), the inner plaque (IP) and the half bridge (HB), and moreover tethers the whole structure at the nuclear membrane (Figure 29). The duplication occurs at the distal end of the elongated HB, at the cytoplasmic side, where a

satellite is formed and organized into a layered structure. The CP and OP then insert into the plasma membrane and the duplication is completed by the formation of the IP <sup>46</sup>. The nuclear MTs (nMTs) polymerized within the nucleus from the two SPB interdigitate to form a short spindle, parallel to the nuclear membrane <sup>47,48</sup>. Motor proteins then push the MTs in an anti-parallel fashion, forcing the two SPBs to move away from each other.

A comparable process is taking place for higher eukaryotes and the MT with the motor proteins are the forces that move the MTOCs apart.

(a) Budding yeast (*S. cerevisiae*)



(c) Higher eukaryotes

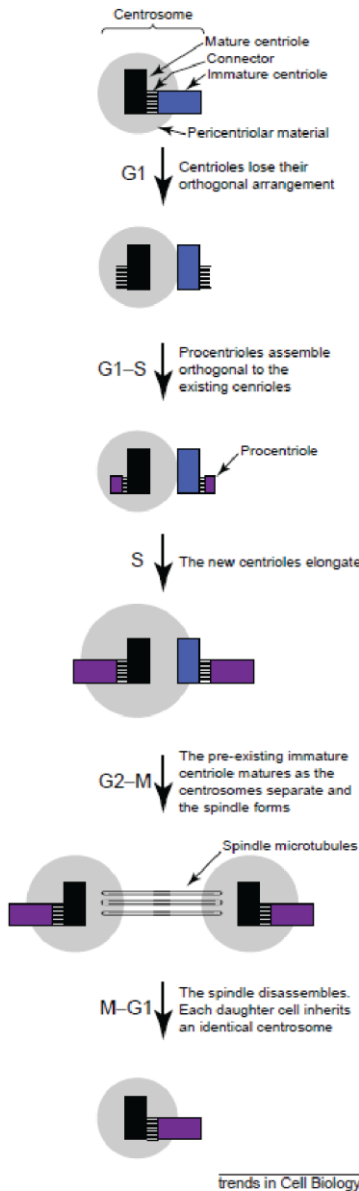


Figure 5 : Diagram of MTOC duplication in budding yeast (a) and higher eukaryotes (c), adapted from <sup>46</sup>. In the budding yeast process (a) the SPB enlarges while the satellite nucleates at the end of the HB. After the assembly of the OP and CP, the duplicated SPB progressively integrates the nuclear membrane while assembling the IP. After the duplication is completed, the MTs interdigitate and motor proteins generate the force to pull the two SPBs apart. In higher eukaryotes (c), the mature centrosomes separate and start assembling the procentrioles. Once the centrosomes are fully duplicated, the MTs interdigitate similarly to the ones in budding yeast to pull apart the two newly formed centrioles.

Once the MTOCs are facing each other and organize the MTs into a spindle structure, they become ready to operate the chromosome segregation. First, proper amphitelic attachment of the duplicated chromosomes to the opposite spindle poles is checked. The KTs, located at the centromeres, sense the attachment of kinetochore MTs (kMT) fibres towards opposite poles. By regulating the kMT depolymerization at the KTs, and at the corresponding MTOC,

the chromosomes are pulled apart toward each spindle pole. The MTOC are involved in regulating synchronous kMT depolymerization prior to the structure MT.

#### f. The kinetochores

The KT is a protein complex that links MTs to the duplicated chromosomes in a specialized deoxyribonucleic acid (DNA) region, the centromere. Their stable attachment to both MTs and DNA is a prerequisite to accurately and efficiently distribute the genetic material to the two daughter cells. The KTs are made of several building blocks including the inner and the outer KT. The outer KT is responsible for the proper interaction with the dynamic MTs while the inner KT ensures the attachment to the centromere. The KTs assemble at the centromeres, which varies in size between species. In *X. laevis*, several MTs are connected to the KTs, in the budding yeast only one MT connects to the KT while in *C. elegans*, centromeres are holocentric. The KT complex cannot be observed in budding yeast by electron microscopy (EM) but have been studied in higher eukaryotes by this technique<sup>36,49-54</sup>

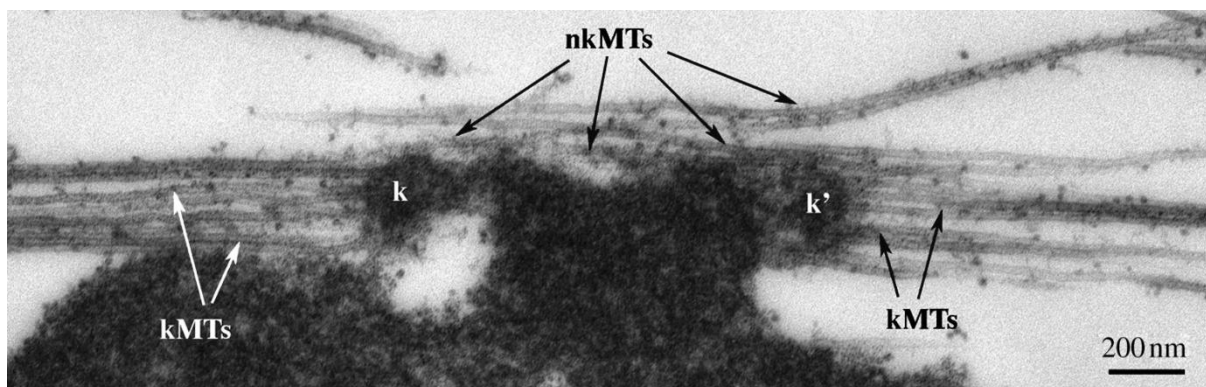


Figure 6 : Sister KT pair in a *Xenopus* extract spindle by thin section EM. The two KTs are designated k and k'. Note kMTs with their plus ends terminating at KTs, and nkMTs that interact laterally with the KT-centromere region of the chromosome and co-bundle with KT MTs. These nkMTs are of mixed polarity, and presumably make anti-parallel interaction with KT MTs. By speckle microscopy, all the MTs in this image undergo polewards flux, though kMTs may slide by approximately 10% slower, on average, than nearby nkMTs (Maddox et al. 2003). For more examples, see Ohi et al. (2003).<sup>36</sup>

To complement the number of electron microscopic studies that were done to characterize the different sub-structures of the spindle, in *X. laevis* and in *S. cerevisiae*<sup>36,55</sup>, biochemical approaches<sup>56-58</sup>, structural approaches<sup>59</sup> and light microscopic studies<sup>60,61</sup> were conducted to get both a functional and physiological understanding of the mitotic spindle in yeast and higher eukaryotes. Structural EM studies were carried out successfully on yeast<sup>55,62</sup> but were not done in natively preserved samples. In the case of higher eukaryotes, the structural

analysis is still presenting challenges that cannot be overcome yet, but physiological representative studies are now possible with the advances of new technologies.

#### **g. Cryo-immobilization of the biological specimens**

The first step in structural and physiological studies lies in the optimal sample preservation. Avoiding immobilization artefacts plays a key role in the following analysis. Structural and physiological analysis requires not over processing the biological sample before the analysis as it is difficult to evaluate the damages retrospectively. To optimally immobilize a sample, the recommended approach consists of a physical instantaneous immobilization. Chemical fixations commonly used are slow processes and the dehydration steps required for EM have strong effects on the physiology of the sample.

To instantly physically immobilise a biological specimen, the optimal solution is to vitrify it. By doing so, one could stop the biological activity within the range of milliseconds<sup>63,64</sup>. Several methods have been developed in this direction to freeze biological material in a vitrified state. Plunge-, jet-, impact- and spray-freezing were used to vitrify in the range of 10 to 20  $\mu\text{m}$  depth<sup>65,66</sup>. The freezing method should produce microcrystalline ice, or optimally amorphous ice from the specimen water. One way to achieve this is to reach freezing rates no lower than 10000°C/s. However, the low thermal conductance of the water limits the efficiency of the freezing at atmospheric pressure and the required cooling rates can only be achieved in the superficial layers of the biological specimen. To lower the nucleation point of ice, important doses of cryo-protectant have been used but these create physiological stress prior to the immobilisation.

High pressure freezing (HPF) immobilization has been developed<sup>64,67</sup> to ensure the optimal preservation of thick biological specimen up to 200  $\mu\text{m}$  without using cryo-protectants. The principle of HPF relies on studies carried out on water and its physical properties<sup>68,69</sup>. The principle is to lower the freezing point of water by increasing the atmospheric pressure surrounding the specimen. At 2100bar, the melting point of water goes to -22°C. In normal atmospheric conditions, the super-cooling and homogeneous nucleation begins at -40°C, while at high pressure (2100 bar) the water needs to reach -90°C. Another important aspect is the viscosity of water which is increased 1500 times at 2100 bar, reducing considerably the ice nucleation rate of water. Using this approach, it becomes possible to freeze water into an

amorphous state. The water molecules then have reduced the time to re-arrange into a crystalline structure (hexagonal or cubic ice). One of the most common states of icy water is a hexagonal re-arrangement. This crystalline structure gives structures like snowflakes. One could easily imagine that the rearrangement of water, intimately bound to proteins, from a liquid (amorphous) to a solid (crystalline) would lead to a phase separation of both proteins from water. At the cellular level, we would then observe regions of segregated pattern of water, surrounded by residual protein material.

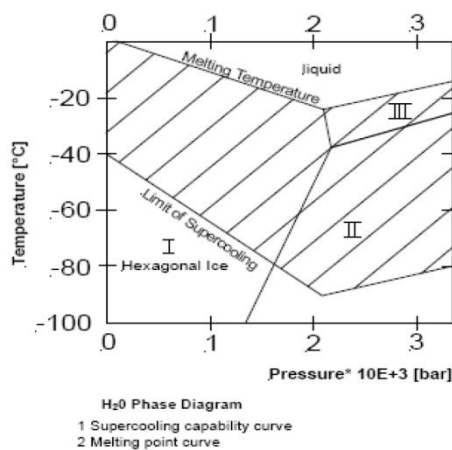


Figure 7 : Water phase diagram.

For all these reasons, the use of HPF appears to be the best option to date to optimally preserve cell structures and was therefore used throughout this whole PhD work.

#### h. Correlative microscopy

Optimal sample preservation is the first key step in any structural study. As explained previously, HPF was our method of choice. However, the HPF advantages in depth preservation are poorly specific. With HPF, vitrifying large volumes becomes possible, but preliminary identification of the sample of interest is rarely possible. In the case of densely packed yeast cells, expressing all the same mutation at the same time, the phenotype identification can be done at the EM level.

But for rare events, a more specific method is necessary. Optimally, we could identify a specific biological event using LM (high specificity of cell transfection to express fluorescently tagged proteins) and process it adequately to retrieve it at EM level. The very active field of correlative microscopy has developed several approaches over the past ten years to address

biological questions <sup>70-76</sup>. Most methods were developed to address a specific question but their generalisation was always complex. Paul Verkade <sup>71</sup> using the EMPACT2 (Leica), developed a series of tool that allowed to identify a cell of interest on a sapphire disk and to retrieve it using landmarks after HPF and freeze substitution (FS). This method was further developed by Irina Kolotuev <sup>70</sup> as well as Thomas Müller-Reichert <sup>77</sup>. The very high specificity combined with rapid freezing within a few seconds after imaging of the interesting event is very attractive. However, the reproducibility is still debated as the low success rate of freezing forces a large number of samples to be prepared.

Taking inspiration from several approaches we have developed our own method to vitrify by HPF *X. laevis* meiotic spindles and retrieve them after FS. The solution found gave positive but poorly reproducible results and to study such structure by electron tomography, it is important to reliably produce enough samples. We therefore investigated to create a technology that we could easily manipulate and would allow us to reliably produce the biological material needed to study the meiotic spindle of *X. laevis* by ET.

Currently, a very reliable machine available on the market for HPF is the HMP010 (BAL-TEC AG). However the holding system is not designed for rapid transfer unlike the EMPACT2 rapid transfer system (RTS) (Leica) and the versatility of both machines is not optimized for correlative microscopy. In the development of new strategies to cryo-immobilize the *Xenopus laevis* (*X. laevis*) egg extract spindle, we realized that the maintenance of the chamber containing the extract did not need to be as tight as suggested in most studies. Based on this observation, we decided to develop a new tool which would fit into the HPM010 clamp and facilitate all the steps from the light microscope through the HPF and to the FS. To achieve this, we focused on standardizing the correlative vector from the LM to the HPF.

One common method in industry to standardize a product in large scale with defined shapes consists in using the so called “over-moulding” technology. Some inserts with defined properties are maintained in a specific position within a mould while a cavity around is filled by a polymer. We used this technology to create a chamber where a sapphire disk and a spacer ring are held tightly together by a plastic polymer facilitating manipulation while the

optical and thermal properties of the sapphire disk are preserved. In the last part this PhD work, the preliminary results of this correlative microscopy chamber are presented.

## Part II: Material and Methods

---

*«L'esprit n'use de sa faculté créatrice que quand l'expérience lui en impose la nécessité.»*

*[Henri Poincaré ]*

## **B- Material and Methods**

### **a. Saccharomyces Cerevisiae**

#### **i. Yeast Culture**

##### **1. Plates and mediums**

###### **a. SC plates**

300mL distilled water (H<sub>2</sub>O), 6,7g yeast nitrogen base (YNB) without amino acids and 2g of amino acid powder without uracil (-ura) were stirred for 30 minutes, and autoclaved. 500ml of H<sub>2</sub>O plus 20g of Agar were added and autoclaved. 100mL of 20% Galactose plus 100mL of 20% Raffinose were added in sterile conditions after cooling.

###### **b. Liquid synthetic medium**

The same procedure was done without the Agar powder.

##### **2. Cell synchronization with $\alpha$ - factor**

Colonies were grown at 30°C on yeast peptone dextrose adenine-supplemented (YPAD) plates selective for ClonNAT, Hygromycin and Geneticin.

ESM 356-1 : Mat a ura3-53 leu 2 $\Delta$ 1 his 3 $\Delta$ 200 trp 1 $\Delta$ 63, was used as wild type (WT) strain for the comparisons with the Cdc4 thermo sensitive (ts) mutant strain.

*S. cerevisiae* yeast were grown in YPAD medium at 30°C for 24 hours until they reached an optical density (OD) of 0.7. Followed a dilution to 0,3OD and addition of  $\alpha$ -factor to yield a final concentration of 5 $\mu$ g/mL at t=0. A second and a third addition were done at t=1 hour and t=3 hours. The cells were spun down and washed 3 times with YPAD to release them from the  $\alpha$ -factor. Freezing were processed at 40 minutes and every 4 minutes thereafter for 40 minutes.

##### **3. Cdc 20 galactose sensitive mutant**

These mutants were kindly prepared by Ashraf Al-Amoudi prior to my arrival in the laboratory.

GALCdc20: Mat a, cdc20 $\Delta$ leu2 trp1+ ade2+

*S. cerevisiae* yeasts were grown on 2% raffinose, 2% galactose plates or equivalent liquid medium. From the Galactose/Raffinose growth medium the cells were washed 2 times by spinning and resuspended in water then spun and resuspended into a 2% glucose medium.

Liquid medium: 2g/L without leucin (-LEU) drop out powder, 6.7g/L YNB without amino acids. Autoclave followed by the sterile filtered add of 100mL 20% Galactose and 100mL of 20% raffinose.

#### ***4. Cdc4-1 thermo sensitive mutant***

Colonies were grown at 25°C on YPAD plates selective for ClonNAT, Hygromycin and Geneticin.

RH207-1: Mat a Cdc4-1ts, ade1 his3 leu2 trp1 ura3

*S. cerevisiae* yeast were grown in YPAD medium at 25°C for 24 hours until they reached an OD of 0.7. They were then transferred at the restrictive temperature of 35°C. After 2h30, the cells were either chemically fixed or High Pressure Frozen, using the Leica EMPACT2 HPF with the rapid transfer system (RTS).

#### ***5. Yeast growth in YPAD + Dextran***

Yeasts were mixed with 20% Dextran (w/v) or 20% Ficoll. The assessment of the viability of the yeasts in Dextran was done by culturing them in Dextran and OD measurement during 5 hours. Every 10 minutes until 80 minutes and then every 30 minutes until 300 minutes.

#### ***6. Immunofluorescence imaging***

The cells were grown in synthetic media in suspension to avoid auto fluorescence.

1mL of cells at OD 0.6 was typically used. They were fixed for 90 minutes with 1M KPi and 5mL Formaldehyde (37%). Washed 3 times in SP (gentle re-suspension). Digestion in 1mL SPβ with 200μg/mL of Zymolyase 100T at 30°C on rotating wheel between 25 and 75 minutes (control of the digestion by phase contrast microscopy: approximately 90% of the cells should appear dark). Cells were washed 3 times with SP and resuspended in 0.5mL SP with 2nM PMSF.

Immunofluorescence: coating of the slides by Poly-L-lysine 0.1% (PLL) for 3-5 minutes, washed 5 times with H<sub>2</sub>O. Cells in SP were added and left settling in a humid chamber for 20

minutes. The excess of medium was removed by gentle vacuum from the side (avoid removing the cells, just the medium). 10 $\mu$ L of PBS-1%TX100 were added and removed immediately. A second drop was added and incubated for 5 minutes. The slides were gently washed 3 times with PBS-1%BSA and incubated in a humid chamber for 20 to 60 minutes.

The Tub2 rabbit antibody 1/5000 in PBS-1%BSA was incubated for 60 minutes then washed 5 times with PBS-1%BSA. Donkey anti-rabbit 1/1000 in PBS-1%BSA was added for 60 minutes.

The slides were washed 8 times with PBS (one or two washes were left for 5 to 10 minutes in a humid chamber) then left for drying 5 minutes. 2.5 to 4.5 $\mu$ L of mounting medium were added prior to nail polish sealing.

Buffer used:

KPi: 1M KPi pH 6.5, 0.5mM MgCl<sub>2</sub>

SP: 1,3M Sorbitol, 100mM KPi pH6.5, 0,5mM MgCl<sub>2</sub>

SP $\beta$ : SP + 1.4 $\mu$ L/mL of  $\beta$ MercaptoEthanol (added fresh).

Formaldehyde 37%: Sigma F-1268

Zymolyase 100T: stock 10mg/mL in SP stored at -20°C

PMSF: stock 200nM in DMSO

Poly-L-lysine: stock from Sigma

Mounting medium: 55% Glycerol in PBS with Hoechst or DAPI)

## **ii. High pressure freezing with the Leica EMPACT2**

The yeasts were filtered through membrane filters (NC45 Whatman, Cellulose Nitrate) by vacuum to collect a yeast paste. The filter was placed onto an YPAD plate to keep the yeast paste humidity level homogeneous until enough samples were frozen.

The yeast paste obtained from filtering was collected with a sterile tooth peak and stuffed into the 200 $\mu$ m deep copper gold plated platelet from Leica, maintained by the RTS clamp. The RTS maintaining the sample carrier was then quickly transferred into the EMPACT2 machine for freezing of the sample <sup>78</sup>.

### iii. Cryo-ultramicrotomy on *in situ* spindle pole bodies

#### 1. Frozen hydrated sectioning – CEMOVIS

##### a. Pre-requisite to sectioning

The high pressure frozen samples were transferred in liquid nitrogen into the precooled ultra-cryo-microtome at -140°C. It has been already established that the vitreous water started devitrification under normal atmospheric pressure at -135°C<sup>79</sup>. Therefore, to prevent the crystallization of the water, special care of the temperature was taken. Proper pre-cooling of every tool that would approach the sample was necessary. A convenient solution was to keep a small volume of liquid nitrogen near the cryo-ultramicrotome where the tweezers could be pre-cooled. The use of self made isolated tweezers might be advisable, to prevent a heat transfer between the tweezers and the user's fingers. The main advantage of the samples prepared with the EMPACT 2 was that the carrier (copper gold plated carrier) is very soft and could be trimmed directly with a 45° trimming diamond knife (Diatome). The HMP010 uses aluminium carriers that cannot be trimmed as previously described. The samples therefore were extracted from the carrier and glued either into a Leica carrier or on top of a freezing pin. The glue used in that case was a mix of ethanol (EtOH) and 1-propanol (1:2 v/v) that is viscous at -140°C and solidifies at -160°C<sup>80</sup>. This way, both HPF machines could equally be used for the freezing.

##### b. Trimming

The sample was held as close as possible to the jaws of the sample holder to avoid chattering during the sectioning, though far enough from block face to avoid risking damage to the knife during the sectioning.

In the case of a sample kept into a Leica carrier, the surrounding metal was trimmed away at high cutting speed and feed (100 mm/s, 500 nm) until the sample was reached. There, the trimming was done to obtain a square or rectangular pyramid: the opposite sides were parallel, using both corners of the trimming knife. Once the first two sides were done, the sample was rotated 90° and the remaining part of the pyramid was trimmed (cutting speed: 100mm/s; feed: 200nm)

The depth of the pyramid did not exceed 50 µm to avoid damage due to fragility and the width was between 80 and 110 µm when working with a homogeneous yeast paste. A 45°

trimming knife is advisable because it produces a large base pyramid, making the block more stable during sectioning.

### *c. Sectioning*

The sections were cut at a feed between 30 nm and 120 nm (nominal) and a speed of 0.4 to 1 mm/s. We used 45° and 35° diamond knives (Diatome) set at a clearance angle of 6°.

To identify the structure in the sections, thin sections were prepared for screening. If the pyramid was properly made, the sections attached to each other, forming a ribbon of sections that could be manipulated with the help of an eyelash fixed on a wooden stick (with some nail polish for example). Once a ribbon of the desired length was obtained, it was carefully detached from the edge of the diamond knife by sliding delicately the eyelash along the cutting edge.

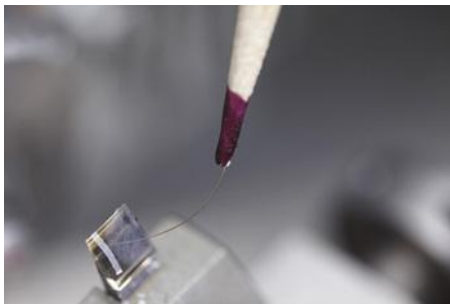


**Figure 8 :** Collection of a section ribbon using an eye-lash prior depositing it on an EM grid. Courtesy EMBL Electron Microscopy Core Facility.

The ribbons have the tendency to get static charging during the sectioning by friction forces<sup>81-83</sup>. This resulted sometimes in making them “jump” and increased the “self-folding” of the sections. As vitrified material is an insulator, the charges remained and accumulated on different areas of the ribbon. A solution was to use an antistatic ionizer that electrically broke down the air molecules around the sections into positive and negative ions. The sections attracted the necessary charges to neutralize the charge on the section. This resulted in obtaining more stretched and less static ribbons, facilitating their manipulation.

### *d. Section attachment*

Once the section ribbons are collected on an EM grid, it is necessary to attach them on the grid to avoid losing them when storing into LN<sub>2</sub> or transferring them to the TEM. The attachment of the ribbon was done by two means: a mechanical pressing or an electrostatic charging. By the mechanical pressing, the ribbon deposited on the EM grid was laid on a very

flat surface (polished metal or ceramic plate). A second pre-cooled flat tool (polished metal or a second ceramic plate) was used to apply a strong mechanical pressure, “sticking” the ribbon on the EM grid. A new method based on electrostatic charging developed by J. Pierson<sup>84</sup> was tested in our group. This method is based on ionizing a grounded EM grid (Figure 9) and helped to firmly stick the sections to the grids.

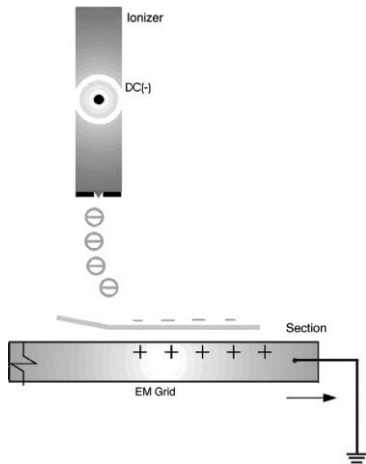


Figure 9 : Schematic representation of the CEMOVIS sections attachment on EM grids by electrostatic charging. Taken from the paper of J.Pierson.

To ensure the proper attachment of the ribbon onto the grid, both methods were usually combined by first attaching the grid using the ionizer/charging device and followed by a gentle press in between two clean ceramic plates.

The grids were then placed into a grid box where they could be stored in LN<sub>2</sub> until the imaging inside the TEM.

#### *e. Fiducial gold marker deposition*

Some trials were done to deposit fiducial markers onto vitreous sections to improve the later tilt series alignment. Quantum dots were used (PbS Core EviDots Espresso quantum dots, Evident Technologies, USA), dissolved in toluene (5mg/mL), diluted into isopentane to a final concentration of 2-4%. The solution was sonicated for 10 to 20 minutes in a water bath prior to the transfer into the cryochamber. The grids were dipped into the solution between -140°C and -155°C (isopentane solidifies at -160°C), briefly rinsed into liquid ethane and blotted onto a filter paper inside the cryo chamber. The grids were left for 2 to 5 minutes outside the grid boxes to let the ethane evaporate.

## ***2. Electron microscopy grid selection***

Three different types of vectors were used, with different coatings, to transfer the sections into the microscope according to the specimen that was being imaged. The first one, being the “Lacey film” coated grids, was a heterogeneous carbon network with large free areas. They are optimal for 2 dimensional imaging but presented a limited attachment surface for the ribbons, thus not optimally stabilizing the sample during multiple imaging (e.g. tilt series acquisition for tomography).

The second and third types of coating were the “C-flat film” coated grids. They are composed of homogeneous carbon layer with known size of pores that allowed us to do direct imaging. The sizes of the pores were either 2 or 4  $\mu\text{m}$  in diameter, spaced by 1 or 2  $\mu\text{m}$  (C-flat, 200b mesh, Protochips Inc, CF-21-2C or CF-42-2C <http://www.protochips.com/products/c-flat.html>).

## **iv. Spindle pole bodies purification, fixation and observation**

### ***1. Purification***

This was done by our collaborator Linda Gombos, from the Elmar Schiebel’s lab, following the protocol established by Michael Rout and John Kilmartin, and refined by Esther Bullitt<sup>62,85</sup>.

### ***2. Plunge freezing with the FEI vitrobot***

The solution containing the SPB was dialyzed against PBS overnight to reduce the amount of sucrose in the preparation prior to the plunge freezing. The lacey grids were glow discharged shortly prior to the experiment. 2 $\mu\text{L}$  of solution were added onto one side of the EM grid. An offset of 5 degrees and 1.5 second blotting were typically used prior to plunging<sup>62</sup>.

## **v. Cryo-electron imaging / data collection**

### ***1. Cryo electron microscopy***

For cryo electron microscopy, the samples were transferred under liquid nitrogen into a Gatan Cryo-holder (Warrendale, PA, USA) prior to their transfer into a Biotwin Ice CM120 cryo-electron microscope (Philips) equipped for low-dose imaging at an accelerating voltage of 100kV. The images were recorded onto a bottom mounted 1K CCD Keen View camera (SIS), between 1000x and 25000x magnification. The images at high magnification were done

using a typical defocus of -1 to -2  $\mu\text{m}$  and the total electron dose was kept between 1000 and 2000  $\text{e}^-/\text{\AA}^2$ , well below the burning dose (3000  $\text{e}^-/\text{\AA}^2$ )<sup>79,86</sup>.

For tomography, the grids were inserted into the cartridge holder of the Tecnai G2 Polara cryo-electron microscope, equipped for low-dose EM with a post-column GIF 2002 energy filter and a 4K CCD camera (GATAN). The images were typically taken at 12500x, 15000x and 20000x. The dose was spread along the tilt series to reach a maximum total dose of 2000  $\text{e}^-/\text{\AA}^2$ . The typical defocus used was 6 to 8  $\mu\text{m}$ .

## *2. Selection of areas to optimize the high resolution imaging*

To reduce the electron dose on the sample prior to the tilt series acquisition, very low magnification and low intensity were used to briefly identify potential regions of interest. Once such location was identified, a low exposure picture was taken to identify the presence of MTs in the nucleus. When such region was found, the acquisition of the tilt series was started. This “semi blind” approach allowed limiting the dose prior to the data collection, preserving the high frequency information (fine structures), but also resulting in acquiring “non-informative” tilt series.

## *3. UCSF tomography (UCSF, San Francisco)*

The FEI Polara microscope (FEG, 300kV) was equipped with a 4K CCD camera (GATAN), physically binned by 2, resulting in a 2K frame camera. The automated tilt series acquisition was controlled with the UCSF tomography program (UCSF, San Francisco<sup>87,88</sup>). To obtain the maximum of information from the first images, the first image was normally acquired at 0° and continued up in one direction (+60°) before returning to 0° and finishing the tilt series in the other direction (-60°). The sensitivity of the sample to the electron dose could be therefore optimally used with the images giving the best signal to noise ratio (SNR). The typical defocus used was -6 $\mu\text{m}$  to -8 $\mu\text{m}$ , and the total dose of electron was kept within the range of 2000  $\text{e}^-/\text{\AA}^2$ .

Film Magnification	Unbinned Pixel (nm)	Binned x 2 Pixel (nm)	Dose ( $e^-/\text{\AA}^2$ per 1000 counts)
13500	0,982	1,964	2,94
18000	0,755	1,51	5,67
22500	0,597	1,194	8,74
27500	0,494	0,988	13,3

#### vi. Electron tomogram reconstruction with Alignator

The alignment of tilt series and the reconstruction the tomograms that were acquired, was exclusively done using Alignator<sup>89</sup>, a program created and developed in our research group to reconstruct tilt series without fiducial markers. The technical explanation of this program is precisely described in the paper. In essence, after a coarse alignment of the tilt series, the user is asked to define the region of interest where the alignment procedure should be focused (drawing of the snake). Trails of small image areas are detected along the tilt series and used to iteratively create a refined 3D marker model (replacing the fiducials traditionally used). After classification of the trails, the user defines the markers with the best shift accuracy and uses it to perform the 3D reconstruction.

This work has inspired strongly the patch tracking method implemented in IMOD in 2010<sup>90</sup>, and played a major role in our working method on the *Xenopus* Project that will be described in the following part.

#### b. *Xenopus* spindle egg extract

##### i. Meiotic spindle self-assembly in a cell free system

The preparation of the *X. laevis* cytostatic factor (CSF) extract was first described in<sup>92</sup>. Since, many papers used this frog egg extract to address questions concerning cell division and spindle function. We used the standard protocol we learned from the Dr Karsenti and the Dr Nédélec laboratories, and adapted it in order to optimally produce the samples needed for our project.

The female frogs were primed by injection of 100 unit of Pregnant Mare Serum Gonadotropin (PMSG) by Kresimir Crnokic or by Erin Tranfield. A second injection of 1000

units of Human Chorionic Gonadotropin (HCG, Sigma) was done the day before (16-18 hours prior to the experiment) to stimulate the egg production. Injected frogs were kept overnight in Marc's modified Ringer solution (MMR) buffer at 16°C. Usually, 5 frogs were prepared for each experiment. The eggs were collected and inspected to select the 2 best looking ones out of the 5 batches (in some rare cases, 2 batches could be mixed to reach a proper amount of eggs). The selected two batches were rinsed two times in 1 litre of MMR buffer (total) directly into the beakers used for collection to clear them from the skin and other detritus. During this step, the abnormal eggs (odd shape, more than 50% white or grey) were removed using a plastic pipette. The eggs were left to settle while preparing the CSF-XB buffer and the dejellying solution. The eggs were re-inspected and dejellyied for 2-5 minutes in a 2 steps wash or until they tightly packed together. They were then washed twice with XB buffer, followed by one wash in CSF-XB. A last wash was done in CSF-XB + Protease Inhibitor (PI).

The eggs were transferred with a soft-edge cut plastic Pasteur pipette into a Beckman SW50 centrifuge tube prefilled with 500µl of CSF-XB+PI (for the experiments without Actin, the solution was CSF-XB+PI+ cytochalasin D). A gentle packing was done at RT on a bench top centrifuge for 30 seconds at 800rpm and 30 seconds at 1600rpm. The excess of buffer was removed.

The eggs were crushed by centrifugation (Sorval Centrifuge, Rotor HB-4, no brake) 12 minutes at 10000rpm, 4°C to isolate the cytosolic part. The cytosolic part was collected on ice by piercing the centrifuge tube with a 18-gauge needle and aspirated in a syringe from the side of the tube then transferred into two separate eppendorfs containing 10µL of PI (100x from stock). After a few inversions of the tubes, they were stored on ice.

CyclinBΔ90 (1:100 stocks) was added in an eppendorf, to half of the extract (1:100000 dilutions). After few inversions, the tubes were stored on ice.

The cycling of the extract should lead to some of the CSF-extract going into interphase. In eppendorfs 100 µL of CSF-extract were added sperm nuclei (15µL from 10<sup>7</sup> sperm nuclei/mL stock) and calcium (1.2µL from 100x stock). To optimize the chances to get cycling extracts, a second interphasic extract was set with concentrated sperm nuclei (3µL from 10<sup>8</sup>sperm nuclei/mL stock). These extracts were incubated at 20°C.

At this time of the experiment, a timer was started and all the subsequent timings refer to this time point (t=0).

After 60 minutes, a test of the extract was set up. In new eppendorfs, 1,5µL of sperm nuclei ( $10^7$  stock), 0,6µL of Cy3-labeled tubulin and 20µL of corresponding extract were mixed and then placed at 20°C for 30 to 45 minutes.

After 120 minutes, the samples were checked at the light microscope: 2µL of FIX was added to 2µL of extract. On the interphasic test, the DNA masses that were in interphase (distinct round DNA mass) were selected for the next step.

In the test extracts, the tubulin was arranged in hemi-spindles or what looked like full spindles (2 hemi-spindles facing each other). The extract with the best structures were used in the further experimental procedures.

The interphasic extract needed to be brought back into mitosis. To do so, as many combinations as possible were set-up to have a chance of one working. The combinations were set as follow: 1 volume (typically 20µL) of CSF-extract from ice was added to 1 volume of interphasic extract plus 1µL of fluorescently labelled tubulin. They were placed at 20°C for approximately 45 minutes. The evolution of the spindle formation was observed with 2µL of sample plus 2µL for FIX on the microscope. If one of the combinations showed the appropriate physiology, the sample was processed further for freezing.

List of buffer used for this experiment:

MMR 20X (Marc's Modified Ringer's solution): pH 7.8, stored at RT, 2M NaCl, 40mM KCl, 20mM MgCl<sub>2</sub>, 40mM CaCl<sub>2</sub>, 2mM EDTA, 10mM HEPES, pH adjustment with NaOH. Sterile filtered

XB 20X, Stock prepared by the EMBL kitchen: 2M KCl, 20mM MgCl<sub>2</sub>, 2mM CaCl<sub>2</sub>.

HEPES 1M pH7.7: 59.6g HEPES, 200mL H<sub>2</sub>O, pH adjustment with 10N KOH, final volume completion with H<sub>2</sub>O to 250mL.

EGTA 0,5M pH 7.7: 47.5g EGTA, 200mL H<sub>2</sub>O, pH adjustment with 10N KOH, final volume completion with H<sub>2</sub>O to 250mL.

CSF-XB: 2mM MgCl<sub>2</sub>, 5mM EGTA, XB 1X, pH adjustment with KOH

CSF-XB + PI: 100mL of CSF-XB + 2 Roche protease inhibitor tablets (EDTA-free)

Dejelling solution: 2% cystein (w/v), 0.5X MMR, pH adjustment with NaOH 10M.

Protease Inhibitor 100x: 1 Roche tablet in 500μL CSF-XB. Make 12μL aliquots and store at -20°C only for a few months.

Fixative mix (FIX): 30% of 37% formaldehyde, 60% of glycerol 80%, 10% of 10X MMR, 10μg/mL Hoechst. Aliquots in 100μL and store at -20°C

Ca<sup>2+</sup> 100X stock solution: 40mM CaCl<sub>2</sub>, 1M KCl, 10mM MgCl<sub>2</sub>.

## ii. High-pressure freezing of *Xenopus* meiotic spindle

### 1. *A correlative microscopy approach*

Electron tomography is a powerful comprehensive method to understand 3D organisation of a biological sample. However, the necessary time to conduct the analysis requires a careful selection of the sample used for the study. Correlative light to electron microscopy allows us to identify a meiotic spindle with the desired characteristics for the project prior to acquire the data at electron tomography resolution. We have developed a method where we can image individual spindles between two sapphire disks and localize them using carbon landmarks. We used a specific assembly composed of sapphire disks and gold spacer rings to individually image spindles. Sapphire is a crystal with good thermal conductivity, good imaging properties and good mechanical resistance. We used these properties to vitrify the *X. laevis* meiotic spindles using HPF.

#### a. *Sapphire disk cleaning*

If the sapphire disks were new (Rudolf Brügger SA, Minusio, Switzerland), they were washed in Acid EtOH (70ml 100%EtOH + 3ml 1M Hydrochloric acid (HCl)), rinsed extensively in H<sub>2</sub>O, washed in acetone, rinsed extensively in distilled H<sub>2</sub>O and dried on filter paper while separating them under a binocular. These steps were repeated until the sapphire disks were adequately clean.

If the disks were already used for a sapphire disk assembly (but not frozen or freeze substituted, in that case, the sapphire disks were discarded according to their chemical

treatments), the sapphire disks assembly were opened in EtOH and the disks and the gold spacer rings separated. The disks were washed in chloroform to remove the phosphatidylcholine (PhChI) or the hexadecene (HxD), and extensively rinsed in H<sub>2</sub>O. They were then sonicated in concentrated H<sub>2</sub>SO<sub>4</sub> or sodium hydroxide (NaOH) for approximately 30 minutes to remove the carbon (if used). Then they were cleaned as described above (new sapphire disks). The gold space rings were sonicated in soap and then in 70% EtOH for 30 minutes.

*b. Landmarking by carbon evaporation*

*i. Use of an electron microscopic finder grid*



Figure 10 : Schematic view of the carbon evaporation projection through the EM finder grid mask.

Once the sapphire disks were adequately cleaned, the landmarking of the second sapphire disk needed to be prepared. A first option was to lay a Fullam Finder Grid (No. 62200)

upwards on top of a clean sapphire disk in a support dish (ensured a proper alignment and facilitated the moving of the sapphire disks into the carbon coater). A thick layer of carbon was evaporated on top of the assembly (Figure 10) in a carbon coater.

To reduce the amount of carbon but keep the finder pattern identifiable, a second grid (No. 28110: 100 Mesh Grids) could be placed on top of this assembly, and skewed with an angle of 45° relative to the finder grid prior to the carbon evaporation.

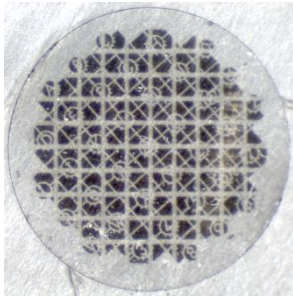


Figure 11 : Top view picture of a carbon land-marked sapphire disk using 2 EM grid masks super-imposed, skewed with a 45° relative angle to reduce to carbon coated surface.

*ii. Use of a PDMS stencil to reduce the carbon surface*

A third innovative option for the carbon patterning was also considered and consisted in creating a stencil of PDMS<sup>93</sup> : A 50-300µm coat of SU8-2075 photoresist (Microchem Co., Newton, MA) was spun (lag time after pouring : 30 sec/v=3000 rpm with acceleration = 005 for 1min,05seconds) on a test-grade Si wafer (2 inch) coated with 1500Å of Si3N4 and softly backed (3 min at 65°C and 7 min at 95°C) on a levelled hot plate. It got exposed to collimated UV light for 14 seconds through a high resolution transparency mask pressed against the photoresist layer. A post-exposure bake was made (1 min at 65°C and 4 min at 95°C) prior to development where the unexposed areas were dissolved in SU8-developper and rinsed with isopropanol. This resulted in a wafer with a depth of 42 microns (profilometry)<sup>94</sup>.

The PDMS prepolymer was prepared by mixing the silicon polymer with its reticulant (1:5) (Sylgard 184 kit, Dow Corning) and degassing at low vacuum (-30 Torr) for 30 minutes. Breaking the vacuum periodically accelerated the process of breaking the bubbles from the surface of the mixture.

The wafer and the glass plate<sup>93</sup> were pre-treated with silane (TMCS Sigma) to reduce the attachment of the PDMS to the glass and the wafer, facilitating thereafter the separation of

the assembly. The PDMS was poured onto the wafer, spin coated (1100rpm; Acc=02; 35 seconds). The glass was laid on top of it and the assembly was tightly held in a press at 50°C for 4 hours.

The separation of the wafer and the glass was done using a scalpel as a lever, with isopropanol wetting. The PDMS mask was mounted onto a large PDMS frame for further handling.

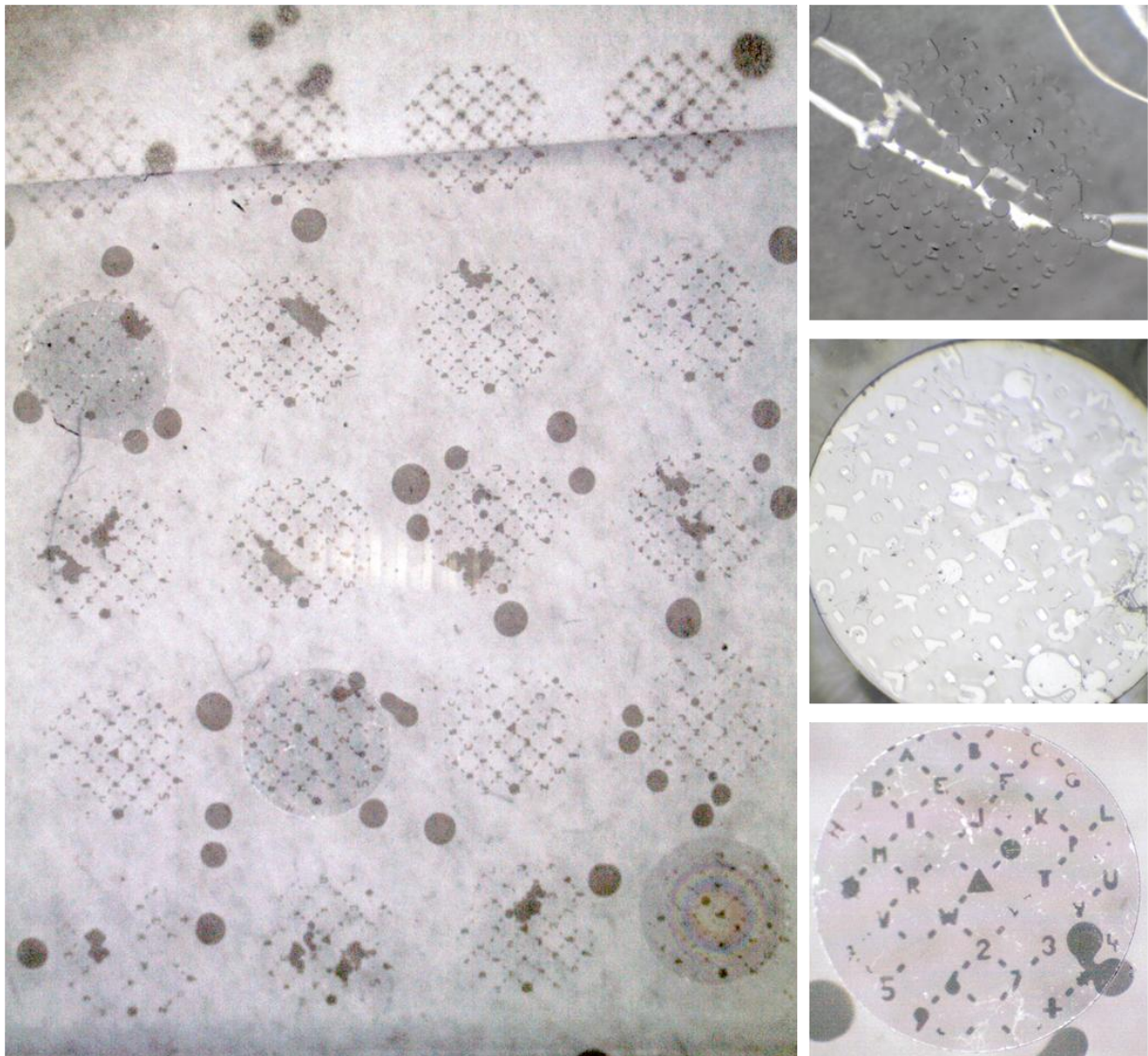


**Figure 12 : The PDMS stencil is poured around 25 correlative patterns. On top of each pattern, a sapphire disk is placed prior to the carbon evaporation. After evaporation the sapphire disks are labelled for proper correlative microscopy.**

The pattern of the high resolution transparency mask was designed manually using Qcad (RibbonSoft GmbH, [www.qcad.org](http://www.qcad.org)), printed at 25000 dpi, on a transparent with a white background, mirrored (Selba S.A. Versoix, Switzerland; [www.selba.ch](http://www.selba.ch)).

The stencil was maintained on a rigid frame. The sapphire disks were then laid on each correlative pattern and the carbon evaporation was done as previously described.

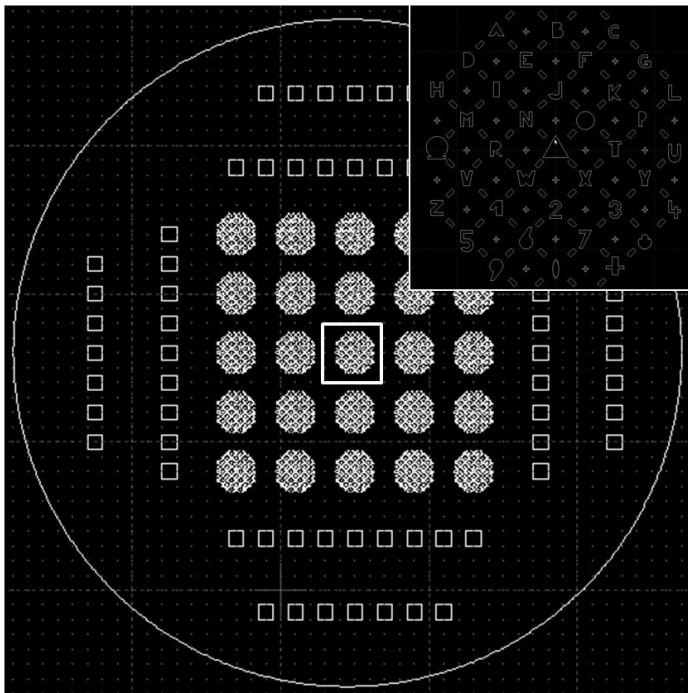


Figure 13 : 25 correlative patterns were designed to cover the centre of a silicium wafer. Once the lithography done, the PDMS stencil was made to create a membrane used later on for the carbon evaporation

### *c. Sapphire disk coating*

The carbon coated sapphire disks were freshly coated with 1/100 diluted solution of PLL on the carbon side for 2 minutes, followed by a quick rinse on water and blotting. They were then stored onto a glass slide covered with parafilm, carbon coated and PLL face up.

The clean sapphires disks were placed on a fine filter paper (No. 50) in a 10cm Petri dish. A drop of  $\sim 5\mu\text{L}$  of 0.5% PC in chloroform at room temperature (storage at  $4^\circ\text{C}$ ) was deposited, forming a large meniscus on top of the disk. The Petri dish was then partially closed to prevent dust falling onto the disks, but let the chloroform evaporate.

Another coating was done by quickly dumping a clean sapphire disk, glow discharged face down, onto a pad soaked with HxD just before closing the assembly.

### *d. Glow discharging*

The elements composing the sapphire disk assembly were placed onto a glass slide covered with parafilm the morning of the experiment while preparing the *Xenopus* egg extract, the coated side of the sapphire disks facing up. Enough elements were prepared to make up to

15 assemblies (15 carbon +PLL coated sapphires disks, 15 gold spacer rings, 15 PhChl coated or clean closing sapphire disks for subsequent HxD coating). They were glow discharged for ~14 seconds, to render them hydrophilic.

*e. Sapphire disk assembly*

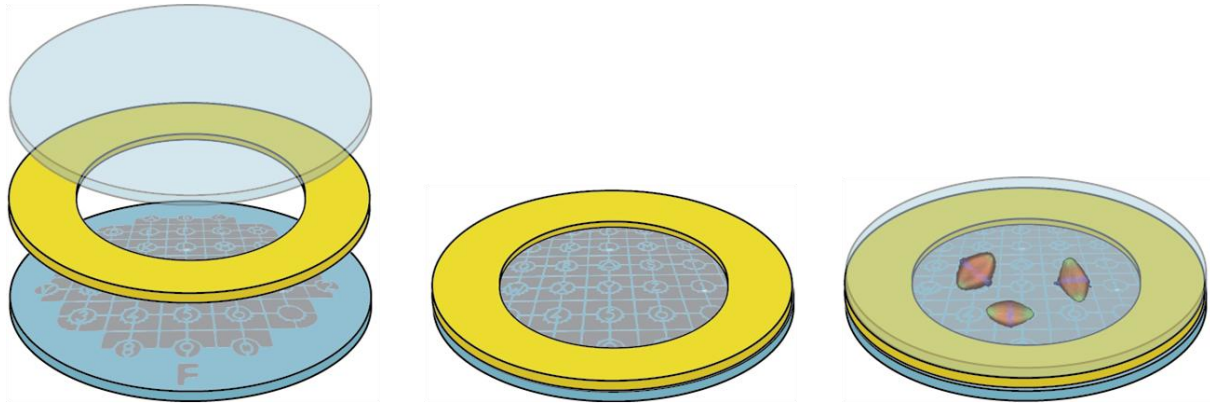


**Figure 14 :** Sapphire disk assembly. The gold spacer ring is first laid and maintained with tweezers on top of the landmarked sapphire disk. 1.5 $\mu$ L of egg extract is deposited in the centre of the ring and the chamber is closed by a second sapphire disk freshly coated with HxD.

Inspired from <sup>95</sup>.

The carbon + PLL coated sapphire disk and the gold spacer ring were maintained by tweezers on a filter paper (No. 50) under a stereomicroscope while loading a 1.5 $\mu$ L drop of extract on it with a cut-ended tip. The assembly was then covered by the closing sapphire disk. A gentle press was done on the closing sapphire disk to evacuate any excess sample. The sapphire disk assembly was then transferred into a bottom glass Mattek dish, containing small stripes of filter paper humidified with filtered water for imaging. This humid chamber allowed the imaging of the sample without drying.

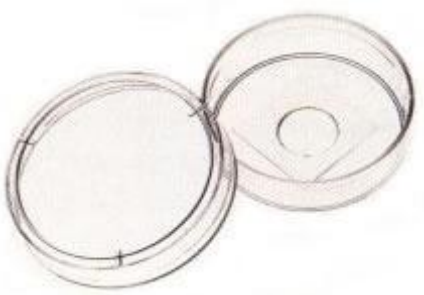


**Figure 15 :** Mattek dish used to image the mitotic spindles within the sapphire disk assembly for correlative microscopy purpose.

### *f. Imaging*

The sapphire disk assembly described above in the section *a.* were blotted (Whatman paper No. 50) before being deposited into a glass bottom Mattek dish. The images were taken with an Axiovert (Axiovert 100, Lumen 200 mercury, objective 10 and 20x, Hamamatsu c8484 camera) inverted microscope through the Mattek dish imaging glass and the bottom carbon coated sapphire disk.

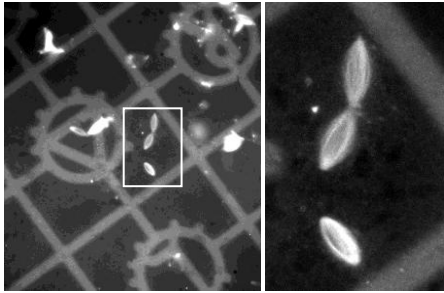


Figure 16 : Low magnification (left) and high magnification pictures (right) of meiotic spindles, within the sapphire disk assembly, related to the carbon land marking.

### *g. Freezing of the specimen in the sapphire disk chamber*

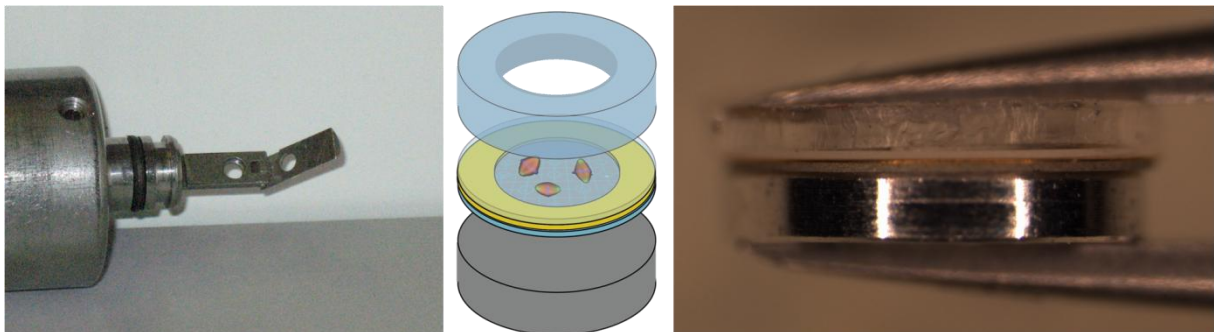


Figure 17 : The sapphire disk assembly is enclosed into the HMP010 clamp, between a B-type aluminium carrier coated with 1-Hexadecene and a dry PDMS ring.

A B-carrier with the cavity facing down (500 $\mu$ m thick, depression 300 $\mu$ m, Wohlwend GmbH, Bifig 14, CH-9466 Sennwald, Switzerland) was first deposited at the bottom and coated with HxD, of the 1mm deep clamp of the Baltec HPM010. The sapphire disk assembly (approximately 150 to 190 $\mu$ m, depending on the sapphire disk thicknesses) was then deposited on top. In order to fill the remaining gap to reach the 1000 $\mu$ m, a PDMS ring manually punched with a 3mm outer diameter and 1,4mm inner diameter from a sheet of various thicknesses from 300 $\mu$ m to 350 $\mu$ m was used. The right thickness was roughly estimated by user observation during the assembly prior to the freezing.

### **iii. High pressure freezing with the Baltec HMP010**

The sample holder of the Baltec HPM010 was used, with the commercially available clamp of 1mm depth. Once the sample is placed into the clamp, the clamp is screwed into the handle and inserted into the HPF specimen chamber for freezing. After the HPF shot, the sample holder is quickly transferred into LN<sub>2</sub>. There the clamp is unscrewed and the sample is released for storage.

One B-carrier thinned down to 350 μm can be used instead of PDMS ring or another setup can be tested.

### **iv. Freeze substitution**

#### ***1. EPON flat embedding***

The FS cocktail was always prepared fresh prior to the FS procedure. We chose a protocol used for optimal MT protofilament preservation. The first FS solution (FS1) contained 2% glutaraldehyde (EMS#16530, from a 10% solution in acetone), 0.1% of Tannic Acid (EMS #21700) in acetone (EMS#10015) <sup>96</sup>. 4ml of the FS1 was placed into a freeze-substitution modified en-block device (the wells have been thinned by cutting the superficial part with a razor blade) and left floating on LN<sub>2</sub> until freezing.

The samples were then transferred under liquid nitrogen into the sample holder. The sample holder was transferred into the precooled Automated Freeze Substitution 1 (AFS1) machine at -90°C. The samples were fixed for 8 hours at -90°C, and then temperature raised 5°C per hour up to -30°C (6 hours) and kept at -30°C.

After 3 hours at -30°C, the samples were gently washed 3 times with distilled acetone (EMS#10015). The acetone was then replaced by the FS2 solution: 1% OsO<sub>4</sub> (1 vial of crystalline OsO<sub>4</sub>, Serva#31251) + 0.1%UA (2% stock in H<sub>2</sub>O) in acetone (final volume of 10mL). After 1 hour at -30°C, the samples were washed 3 times carefully with acetone and transferred onto ice.

Under the stereomicroscope, the sapphire disk assembly were collected from the tubes of the sample holder and quickly dunked into freshly prepared EPON. The covering sapphire disk was removed and if possible without damaging the sample, also the spacer ring. The carbon coated sapphire disk was then dunked into 2 successive reservoirs of fresh EPON

before deposited onto a frame of Aclar®33C. The frame was filled with fresh EPON and closed with a second sheet of Aclar®33C. The Aclar frame was then pressed in between 2 glass slides and left 1 hour at room temperature for infiltration. Afterwards, the whole block was put to polymerize at 60°C for 24 hours.

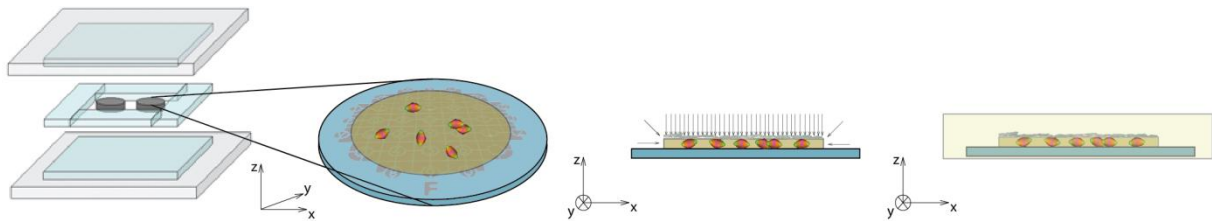


Figure 18 : The landmarked sapphire disk, supporting the biological specimen, is embedded into EPON within a frame made of Aclar. The thin sample is efficiently embedded into the resin.

## v. Ultramicrotomy

### 1. Sectioning of flat-embedded samples

#### a. Sapphire disk removal

The assembly of glass slides was opened and the sample released from the Aclar frame. The excess of EPON below the sapphire disk was trimmed with a sharp razor blade (FEATHER CO, LTD, Osaka, Japan) and the sapphire disk cleared from the sample by gentle mechanical force. No heat shock was used to preserve the carbon pattern, used later on for correlating the location of the spindles (Figure 19).

#### b. Re-embedding

The sample, cleared from the sapphire disk, was re-flat embedded into a second Aclar frame to give more rigidity to the assembly during the sectioning.

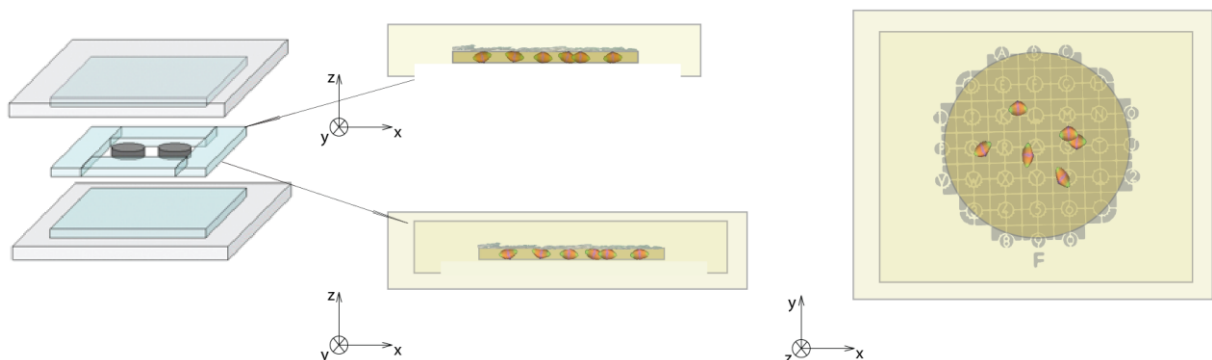


Figure 19 : After releasing the sample embedded into EPON from its sapphire disk (the supporting medium has been changed from the sapphire disk to the EPON resin, the sample is re-embedded into a comparable apparatus. This allows us to manipulate a thicker and less flexible specimen

### *c. Trimming the sample using the carbon mask*

The location of the identified spindle of interest is made by rough trimming with a razor blade, then refined with a glass knife and finally a fine and precise trimming is done with a trimming diamond knife (Diatome AG, Biel, Switzerland). (Figure 20)

### *d. Laser etching option*

To facilitate the trimming, laser etching was attempted onto the flat embedded sample to help identifying the regions of interest during the trimming and the sectioning.

## **2. Serial sectioning and sample collection for electron microscopy acquisition**

Serial sectioning was done with a diamond knife (Diatome AG, Biel, Switzerland). The sections were collected on a formvar (0.7% in Chloroform) coated slot grid (Plano GmbH, Wetzlar, Germany).

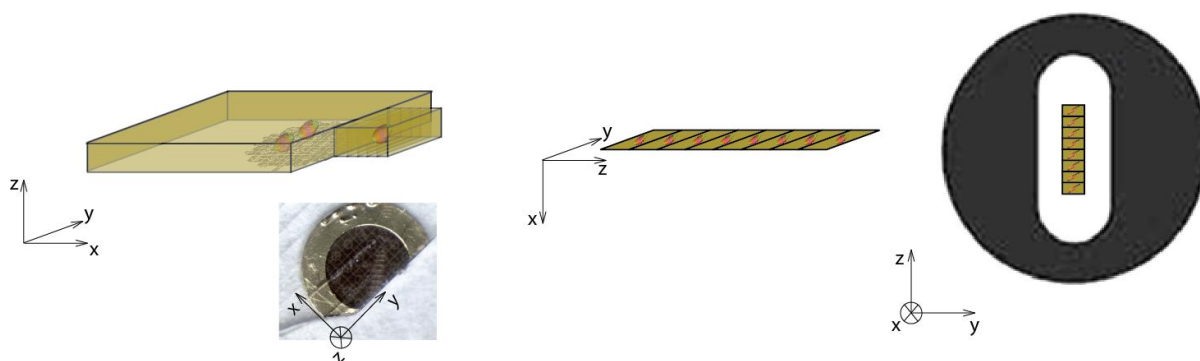


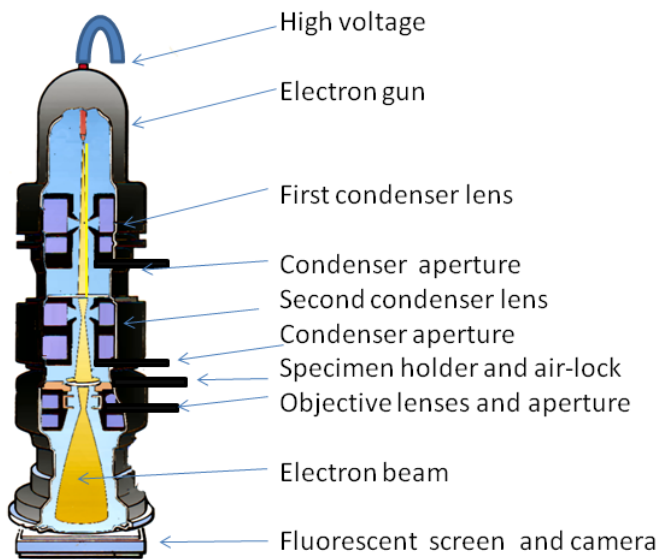
**Figure 20 :** Once the flat block is trimmed according to the correlative carbon landmarks, the sections are collected on a slot grid coated with 0.7% formvar.

## **3. Contrasting and application of fiducial markers**

Serial thick sections (300–310 nm) were cut with a Leica Ultra-cut UCT microtome. Sections were collected on formvar-coated, palladium-copper slot grids. Protein-A gold particles (15nm, CMC Utrecht) were applied to both sides of the grids to be used as fiducial markers. Then the sections were post-stained with various time combinations of uranyl acetate (UA) (0.5% or 2% in MeOH) and of lead citrate (LC) (from 0' to 20' each in cross combination, final protocol: no UA, 12 minutes LC).

## vi. Data collection

### 1. Transmission electron microscopy



## Transmission Electron Microscope

Figure 21 : Transmission Electron Microscope schematic representation (Wikipedia/Electron microscope) and image formation.

Transmission electron microscopy is a microscopy technique where a uniform beam of electrons is projected through an ultrathin specimen. While passing through the specimen, the electrons interfere with the material and form a negative image by electron absorption. The image is collected on a charge-coupled device camera (CCD camera) and computationally stored for later use. The small de Broglie wavelength of the electrons enables significantly higher resolution than light microscopes. The nature of the electron requires also a different technology to create the uniform electron beam. Instead of using glass lenses to correct the light path, electro-magnetic lenses are used, also called condenser lens. Subtle changes in the electric intensity of the condensers enable instant changes in the beam path without mechanical vibrations.

### 2. Electron tomography

Electron tomography was done using a FEI F30 transmission electron microscope, equipped with a field emission gun (FEG) operating at 300kV. The basic principle of electron tomography consists of acquiring a series of samples under scrutiny tilted inside the microscope at different tilt angles with a given increment. The sample is coupled to a goniometer for the tilting. The tilt series acquisition procedure is done using the automated

program SerialEM<sup>97</sup>. The collected tilt series is aligned *in-silico* using the ETomo package<sup>90,98</sup> and the images are back projected into a 3 dimensional space, creating a 3 dimensional electronic reconstruction of the sample.

During the acquisition of the tilt series, the sample thickness increases according to the following rule:

$$t = t_i / \cos \alpha$$

Where  $t$  is the increased thickness,  $t_i$  the thickness of the sample (typically 300nm) and  $\alpha$  is the tilt angle. For example the sample thickness increases two times at 60° tilt compared to 0° tilt. To compensate for this increase and keep constant the number of electrons reaching the camera (typically a mean of 11000e<sup>-</sup>/pix), we increased the intensity of the beam by focusing it at the C2 condenser.

### 3. Large area acquisition at high resolution

#### a. Montaging

To acquire large areas at high resolution (1 or 2nm/pixel), several parameters were considered. The surface that could be imaged was dependent on three parameters. The first one, fixed along the whole study, was the frame of the camera. We used in house a 4096<sup>2</sup> pixel frame camera (Eagle, FEI), defining our maximum surface acquisition. The second parameter was the magnification at which the images were taken. The combination of the magnification and the number of available pixels on the camera defined the surface that was imaged per single frame and we deduced from it the pixel size.

Film Magnification	Unbinned Pixel (nm)	Binned x 2 Pixel (nm)	Acquisition surface(nm)
3900	2,94	5,87	12042
4700	2,483	4,97	10170
9400	1,267	2,53	5190
12000	0,997	1,99	4084
15500	0,750	1,499	3072
20000	0,590	1,179	2417

Our biological specimen (the *X. laevis* mitotic spindle) could be schematized as a double cone contained in a cubic volume of 15x15x30 μm. To cover a defined sub-region like the spindle

midzone, a frame of at least 12x12  $\mu\text{m}$  was required (the shrinkage of the sample under the beam reduces the overall sample size<sup>99,100</sup>). As the required resolution to resolve our structure of interest was a fixed parameter (2nm/pixel for identification of the MT ends), the solution consisted in making a so called montage frame, our third parameter.

The electron microscope is composed of electromagnetic lenses that are focusing the electron beam. This gives the capacity to modify the electron beam path by simply changing the current intensity of the condensers, without any mechanical intervention. It becomes therefore possible to instantly and precisely shift the beam a few microns away from the central path, and bring it back to focus in line with the fixed camera. By repeating this process adequately, it becomes possible to acquire 3x3 frames (in our case) without mechanical interference. Each of the 9 frames covering 4.09 $\mu\text{m}$ , using an overlap of 300 pixels between the frames, the final covered area was 11.5 $\mu\text{m}$ x11.5 $\mu\text{m}$  (Figure 22).

To efficiently realize this large dataset acquisition, the ETomo program was given landmarks to refer to during the imaging procedure. Prior to the montage tilt series acquisition, we acquired a low magnification map (3900x) of the region of interest (Figure 22). Each frame of the montage was then aligned by cross correlation to the low magnification map. Furthermore, a cross-correlation of the frames overlap was verified during the acquisition procedure. This series of controls avoided inappropriate image acquisition without human supervision.

The images were then stitched together by cross correlation within ETomo to form an image of  $\sim 11600 \times 11600$  pixels (depending on the precision of the beam shift and the cross correlation value obtained) if no binning was used.

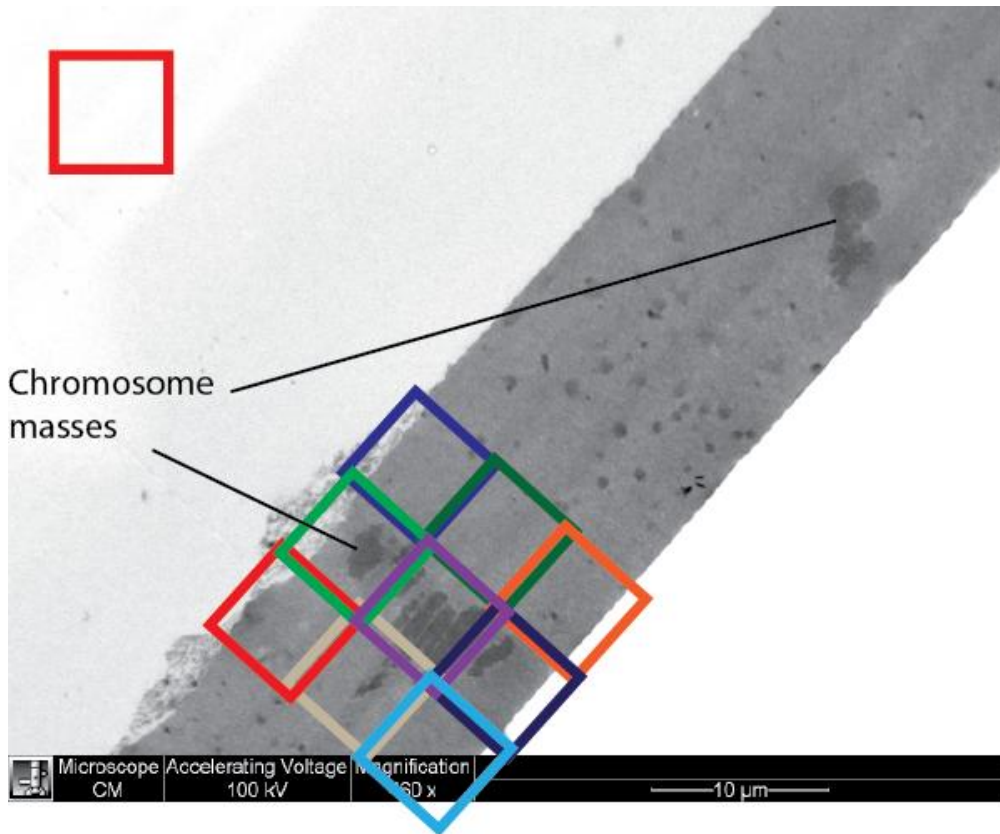


Figure 22 : 3x3 montage of 4k<sup>2</sup> frames binned by 2, resulting on 2k<sup>2</sup> frames. The final size is therefore approximately a 6k<sup>2</sup> frame with a pixel size of 2nm. The top left red-square symbolize a single frame. The mis-alignment of the frames representing the montage is representative of the raw data.

*b. Electron tomography of montages*

The expansion to ET of montages consisted in acquiring montages at every tilt angle and to back project those montage images to generate the tomogram.

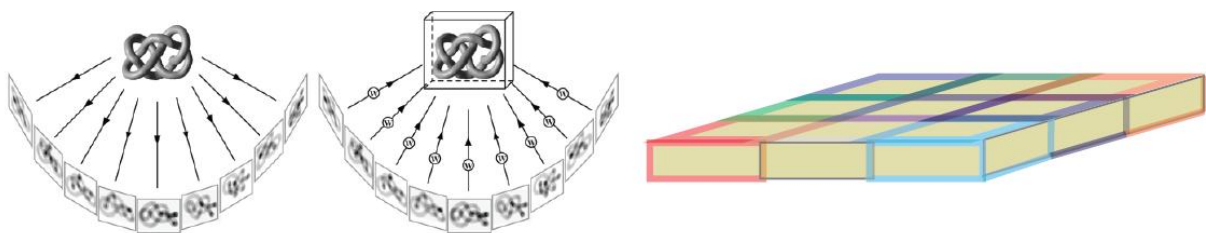


Image credit: W. Baumeister

Figure 23 : Schematic representation of the acquisition followed by a reconstruction. The final volume can also be the product of a montage.

### *c. SuperMontaging*

To cover the whole spindle length ( $\sim 45\mu\text{m}$ ), the principle of the montaging was simply expanded by acquiring 3 montages (3x3 frames each) along the pole/pole axis of the spindle, moving mechanically the specimen between each montage tilt series.

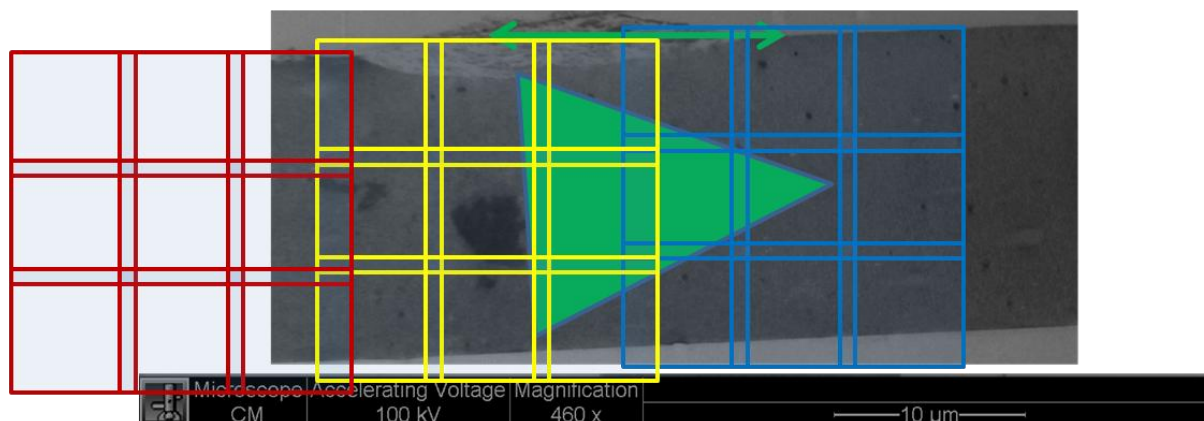


Figure 24 : Schematic representation of the super montage at 4700x.

Datasets were acquired for tests purposes but could not be efficiently used for the purpose of this work (Figure 55, vii.3).

## **vii. Electron tomogram reconstruction with the IMOD suite**

### **1. Montage reconstruction**

Once the montage tilt series were acquired, the tomogram reconstructions were done using the ETomo package from the IMOD suite. The tilt series were opened and every montage frame was stitched by cross correlation. The edges were fixed while making a distortion corrected stack then a coarse aligned stack. The alignment of the frames could be done by two different methods. The conventional one consist in selecting individual gold bead markers deposited at the top and the bottom of the section (p54 §B-b.v.3), and to track them individually along the whole tilt series. The tracking of each individually selected bead was mainly done by the program. An iterative fine alignment of the gold beads was done manually to refine the alignment accuracy<sup>101</sup>. However, this process on large volume required very time consuming corrections and was not always accurate enough.

Since March 2010, a new method, inspired from the Alignator program created by Daniel Castano et al.<sup>89</sup> allowed a more efficient tracking along large datasets. The procedure of reconstruction was comparable to the ones where beads were tracked. Only the fiducial

tracking differed. The user defined patch sizes (typically X100, Y100 for 3x3 montages), eventually defining a specific region for the tracking (boundary model), and left the algorithm track the image patches. During the fine alignment step, the patches with the largest alignment error were discarded until the alignment error reached a maximum value of 1.5 pixels for the final reconstruction.

After this fine alignment step, independently of the alignment procedure selected, the positioning of the tomogram was defined from sample tomograms, the stack with the final alignment was generated and the tomogram was generated. For post processing, the tomogram was trimmed at the top and the bottom and the gray scale re-adjusted without the gold particles to display the biological structures within the largest range of the 256 gray values of an 8bit display.

## *2. Flattening*

Once the tomogram was reconstructed and trimmed (the process is the same for single frames as for montage tomograms), an important step was the flattening. During the initial pre-burning of the sample (pre-exposition to  $2000\text{e}^-/\text{\AA}^2$ ) and the imaging, non linear distortions of the plastic resin warped the sample in the 3 dimensions. The final reconstructed tomogram represented accurately these deformations. However, as serial reconstructions were needed to answer our biological question, we had to join the sections together in a larger volume (a so called joined tomogram). Deformations were an obstacle to accurately join the tomograms: the larger the areas were, the more difficult it became (*e.g.* montages). The solution was to mathematically flatten the tomograms separately prior to the joining.

In ETomo, once the tomograms have been trimmed, the data can be flattened. In the Flatten Volume tabulation, the volume was opened along the X/Z plane to clearly draw the surface model. We then calculated the smoothing factor (from 0.5 to 4 by increments of 0.5), running "*Flattenwarp to assess smoothing*". After evaluating the appropriate smoothing factor (Open Assessment in 3dmod), the "*Flattenwarp*" was run followed by the "*Flattening*". The quality of the flattening was assessed by eye and re-run if not satisfactory.

The precise description of the flattening algorithm is made in the IMOD help file, but in essence it uses the model surface to move each part of the volume in Z to a common plane

while finding the rotation required to make the tangent to the surface flat. It also compensates for the shearing.

### *3. Super-Montages*

The super montage consisted in aligning several montages together. The first steps until the flattening of each individual montage was required as described above. The blending of the montages together was however not a linear process as we had initially imagined. During the acquisition of the first montage the regions that were later overlapped with the second montage got a quantifiable amount of electrons. These electrons continued affecting the section morphology despite the pre-burning. When the second montage was acquired, the overlapping region got another equivalent dose of electrons, resulting in an increased warping. This secondary warping was not linear and it is still not completely clear to our expert collaborators in Boulder (Colorado) how to compensate for these non linear distortions such that the stitching of these montages could accurately represent the biological dataset.

This super montage method is still under development and the actual tools are not yet completely developed. We therefore reconstructed the tomograms manually. The overlapping number of pixels was estimated by eye (although initially defined in the acquisition parameters, those happened to be often off). Patches of the edges were generated and fitted accordingly to the respective location of the three tomograms. The alignment of the stitching was calculated prior to the actual stitching of the tomograms together with the different accepted levels of error.

Below are the actual command lines used:

```
edgepatches -info rootname_info.txt -noz -root rootname -  
overlap 3900,389 -underscore -xyadd 1,3 -all -redo
```

```
fitpatches -info rootname_info.txt
```

```
stitchalign -info rootname_info.txt
```

```
tomostitch -info rootname_info.txt -target  
0.5,0.75,1,1.25,1.5,1.75,2,2.25,2.5,2.75,3
```

#### 4. Joining

Once the tomograms were reconstructed, flattened and trimmed, the joining consisted of aligning the tomograms from the serial sections together to reconstruct the whole volume. Using Midas, the top section of the bottom tomogram was matched with the bottom section of the top tomogram. The matching was done by translation, rotation and stretching.

When several tomograms were joined together, the deformation of each tomogram was done by linear transformations between the top and the bottom sections of each tomogram to create the most homogeneous deformation possible, thus limiting artefacts.

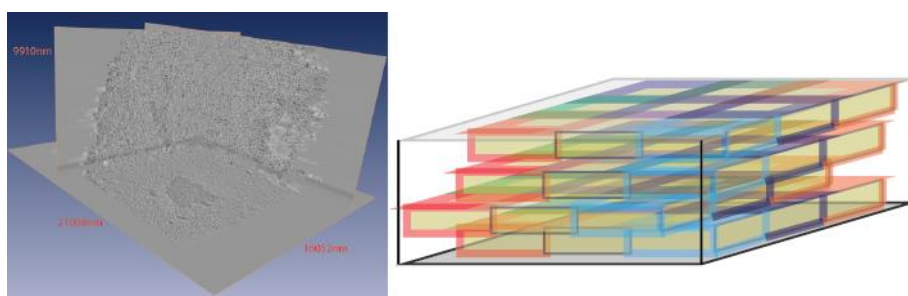


Figure 25 : 3D view of the join (a). Schematic representation of the volume after joining of the montage tomograms (b).

#### viii. Microtubules Modeling

##### 1. Manual Tracking in IMOD

To obtain quantitative measurements from the collected tomograms, segmentation of the information is required. In plastic tomography, the segmentation is commonly done manually by experts. To track all the individual MTs from the joined tomogram, sub-volumes were selected and opened using Imod. The full XY area was loaded into the memory while only parts of the sections were loaded along the Z axis. We typically loaded 450 to 500 electronic slices along the Z axis, being sufficient to fully see one tomogram, the joining regions and the beginning of the former and next tomogram in the displayed volume.

In the main window, in model mode, a region where a MT could be observed was clicked. The short-cut key “\” opened the “slicer” window, where an electronic section of the tomogram was oriented in any desired direction. Following the MT up to one of its ends by aligning the electronic section towards the longest orientation of the MT, the “start” of the desired MT was identified. Often, the MT continued out of the tomogram, resulting in tagging the end morphology accordingly (black end). After identifying the “beginning of the

MT” in the tomogram, and going reversely, the MT was carefully tracked by marking its path along the tomogram until the “end of the MT”. When possible, the MT end was tagged accordingly to its type of morphology or its exit from the tomogram.

This procedure have already been extensively described by Johanna Höög in a book chapter <sup>101</sup>.

## ***2. Ends identification at 12000 and 15500x for polarity identification of the microtubules with IMOD***

During the tracking of the MTs, the two ends of some MTs could be found within the tomogram but most of the MTs that could be isolated continued outside of the tomogram and were marked as described previously. However, when the MT ended within the tomogram, we could try to determine its end morphology unambiguously, informative about the MT polarity. The computational tomographic slice was rotated mainly around the long axis of the MT (but also along the other axes for clarity) and the MT end features carefully observed. The tags were decided by initially referring to a “MT ends gallery” as proposed by Johanna Höög <sup>102</sup>. After identification of the different ends morphologies from our sample, we created our own MT ends gallery for reference.

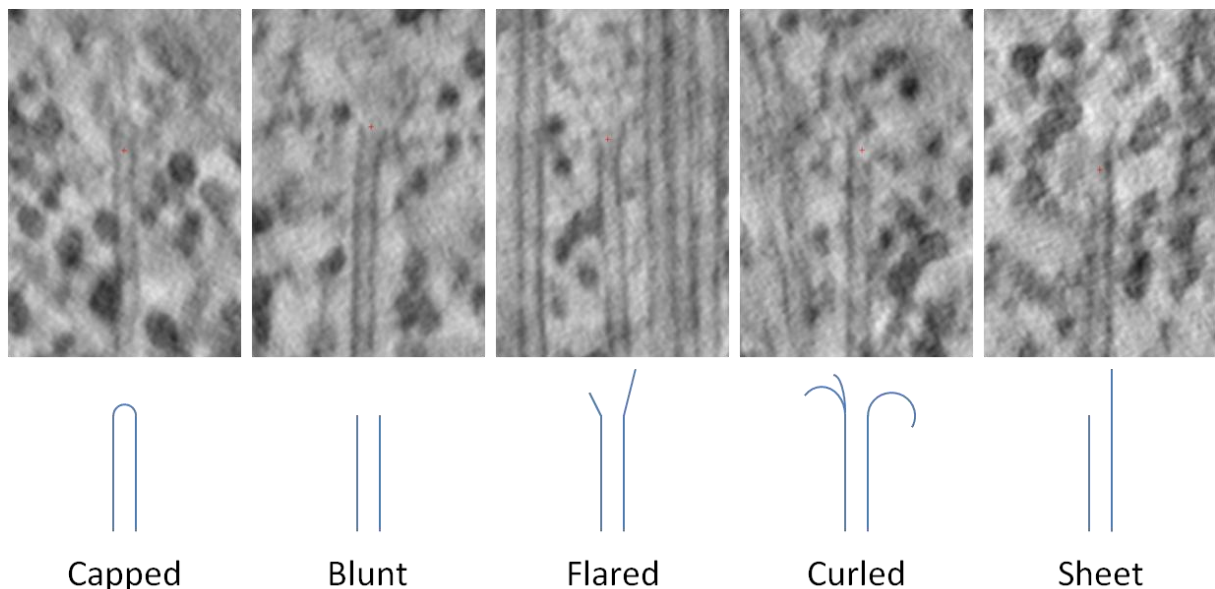


Figure 26 : MT ends gallery from *X. laevis* meiotic spindle egg extract.

## ***3. Microtubules tracking using the ZIB-Amira package***

This following paragraph corresponds entirely to work done by our collaborator at the Zuse Institute Berlin (ZIB-Amira) and most of the further developments were conducted by and

with Erin Tranfield. As this work is still under development, I have not been able to actively use this program, but the major advances this program provides shall be presented for a better understanding of the *X. laevis* project on the long term.

The large dataset that represents the meiotic spindle of the *X. laevis* egg extract is challenging and the data analysis cannot be realistically done entirely manually. For this purpose, the use of automatic or semi-automatic procedures to detect the MTs in the tomographic volumes is crucial. Britta Weber, from ZIB-Amira, developed a template matching approach to identify the MTs in the bundles. To do so, cross-correlation of an idealized cylinder is computed with the tomogram. Most likely orientation of the MTs is correlated and used to seed points for MTs. The MTs centrelines are then tracked from the seed point following the computed orientation of the MT. The optimal cylinder length was optimized to our biological sample, seed points were threshold by correlation and image value.

The semi automatic procedure requires the seeding of the MT by the user and the computer then automatically identifies the orientation of the MT and tracks it. In both cases, manual correction is required for an optimal tracking of all the MTs contained in the tomogram.

#### ***4. Data preparation for fast modeling***

Modeling of the whole dataset requires automated programs. Meanwhile, segmentation of the large structures of the tomogram could be processed. Segmentation of the chromosome mass and of the large bundles could be used to visualise the global structure of the spindle. We have developed an approach to segment these two subsets of structures within a reasonable time. However the final join volume of a full spindle or cell is too large to be analyzed directly within a conventional computer. Three quarter of the spindle midzone at 2 nm per pixel resolution corresponds to a single file of 400 Gb. Our computers (48 Gb of RAM memory at most) cannot handle this large data files without binning the data. This results in a loss of information, necessary to process the data. To handle the generated join, a stack of images from the *JoinedTomogram* was created, along the Z axis (best 2 dimensional resolution axis of the tomogram), extracting systematically one section from every 10. From an initial volume of 10504 x 8026 x 4955 voxels, a Z stack of 496 sections of 10504 x

8026pixels was obtained using the mrc2tif program from the IMOD suite. We will refer in the following part to this stack as the “*OriginalStack*”.

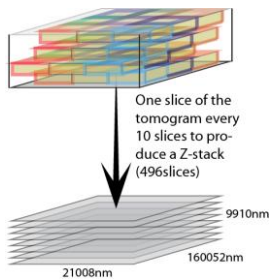


Figure 27 : From the 3D volume of a tomogram to a Z-stack of 2D images used for batch processing.

Those single images can then be processed individually (80Mb each), using batch processing, to analyze the dataset.

### 5. Fast modeling of chromosome mass using TrackEM2 package and FIJI

To segment the chromosome mass, we used the TrackEM2 package from FIJI. This programme is specially designed to handle large volumes of individual files (like large Z-stacks). The first step consisted in creating a *new project* into TrackEM2. For that, the *OriginalStack* was imported as *file -> import -> image sequence -> virtual stack*, the properties edited for the stack (*Image -> Properties*) and the pixel size given in XY and Z (10 times the XY pixel size, as the stack was generated this way). Then *File -> New -> Track2EM (Blank)*. (More details to be found on the online manual at <http://www.ini.uzh.ch/~acardona/trakem2.html>)

The chromosome mass could be identified by eye on any electronic section by its higher density. The *OriginalStack* was smoothed within FIJI, by batch processing. In FIJI, the already loaded virtual stack was selected (not the TrackEM2 project), then *processed-> batch-> virtual stack: run("Gaussian Blur...", "sigma=2");* (Figure 28)

A new virtual stack, which was smoothed, was generated and saved as an image sequence; we will refer to this stack in the following parts as the “*SmoothStack*”. Using the magic wand of FIJI (mode Legacy, Tolerance from 8 to 20 depending on the section), a Region Of Interest (ROI), defining precisely the DNA mass was outlined and stored into the ROI manager.

The regions of interest defined from the *SmoothStack* were pasted into TrackEM2 manually. This way, the whole chromosome mass was segmented within 3 days.

The chromosome mass was visualized using 3Dviewer with a down sampling parameter of 41.

The stack, for a reason that couldn't be explained was loaded in a mirrored way compared to the same stack in Amira. To match the chromosome mass outline with the model of the bundles in AMIRA, the images were mirrored adequately in FIJI (*Image -> Transform*) before the generation in 3Dviewer. The final volume surface was then saved as STL (ASCII).

### ***6. Fast modeling of the bundles of microtubules with image filtering and Amira 3D histogram segmentation***

The *SmoothStack* was further processed for variance (radius = 5) and bandpass filtered.

```
run("Variance...", "radius=5");  
run("Bandpass Filter...", "filter_large=100 filter_small=50  
suppress=None tolerance=5 autoscale saturate");
```

This processing resulted in a second virtual stack where the chromosome masses were smoothed out and the large bundles heavily marked (saved as an image sequence). We will refer in the following part to this stack as the *BundleStack*.

The *OriginalStack* and the *BundleStack* were binned 2 times and saved as "TIFF" image sequence. The image sequences were transformed into a ".rec" stack using the tiff2mrc program from the IMOD suite (mrc native format). The *OriginalStackBin2.rec* and the *BundleStackBin2.rec* were then be loaded into the computer's memory within AMIRA.

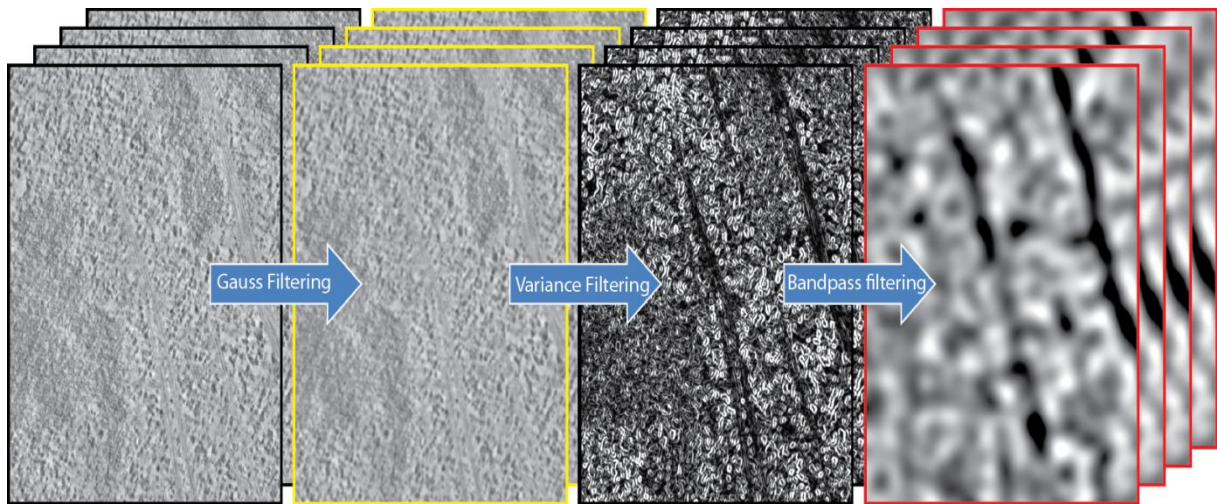


Figure 28 : Sequential filtering of batch images. The yellow framed batch will be later on used for DNA segmentation in FIJI. The red frames batch will be later on used for bundles segmentation in Amira.

Using the segmentation editor from AMIRA, on the BundleStackBin2.rec, regions of detection with a large rough paint brush (red area) were defined, within which the regions of interest were segmented by Histogram restriction (0-62, on a scale from 0-255). An area list was generated from this segmentation.

The bundles crossing several tomograms segmented separately were then grouped manually: from two area lists A and B, renaming B into A gives the opportunity to merge the two area lists into one, as a native function in AMIRA.

# Part III: The mitotic spindle in *Saccharomyces cerevisiae* is focally organized by the Spindle Pole body

---

*«Délaisse les grandes routes, prends les sentiers.»*

*[Pythagore]*

## C- The Mitotic spindle in *Saccharomyces cerevisiae*

### a. The mitotic spindle is organized by the Spindle Pole Body

#### i. The Spindle Pole Body structure

In the budding yeast *S.cerevisiae*, the SPB is required for a variety of functions such as the cell cycle regulation, chromosome bipolar segregation during mitosis and meiosis. Its function is strongly comparable to other MTOCs, although morphologically extremely different from centrosomes. This redundancy in function might explain the partial conservation of their assembly mechanisms. The SPB of *S.cerevisiae* has been studied for a long time<sup>103,104</sup> and the structure, the protein composition, the duplication, the regulation and the function were already extensively described. Our project consisted into getting a model at molecular resolution of the SPB during the cell cycle.

Over the past, many studies were conducted to understand and characterize the SPB. Several EM works were done to characterize the structure of the SPB during the cell cycle<sup>55,62,103-105</sup>. It is a cylindrical organelle composed mainly of 3 disks (called plaques) of darkly stained material. The outer plaque (OP) faces the cytoplasm and regulates the cytoplasmic MTs (cMTs). The inner plaque (IP) faces the nucleus and organizes the nMTs, while a central plaque (CP) spans the nuclear envelope and is associated to a structure called the half-bridge (HB) that is responsible for the generation of the new SPB at the cytoplasmic side during G1 phase of the cell cycle<sup>103,104,106</sup>. For the various functions of the SPB to be fulfilled a high dynamicity during the cell cycle is required. If the height of the SPB is conserved along the SPB cycle and is of about 150 nm, the width may vary from 80 nm in G1 to 110 nm in mitosis. An interesting observation is that this increases with the DNA content. In diploid cells, it has been reported that the SPB reaches a diameter of 160 nm, and this might double with tetraploid cells<sup>62,103,104</sup>. The consequence of this enlargement is the concomitant increase in the MT nucleation capacity of the SPB, necessary for the chromosome segregation. However, the size regulation pathway is still unknown.

In mitosis, the molecular mass of the diploid SPB including the MT and MT associated proteins (MAPs) has been estimated as 1 to 1.5 giga Dalton (GDa), where the core SPB represents 0.3 to 0.5 GDa<sup>62,106</sup>. Out of the estimated 30 proteins composing the SPB, 17

have been identified to date<sup>48</sup>. Deletion or mutation of any of those proteins leads to severe alteration in the SPB function and structure. The list of these proteins has been well described in table 1 of<sup>48</sup>.

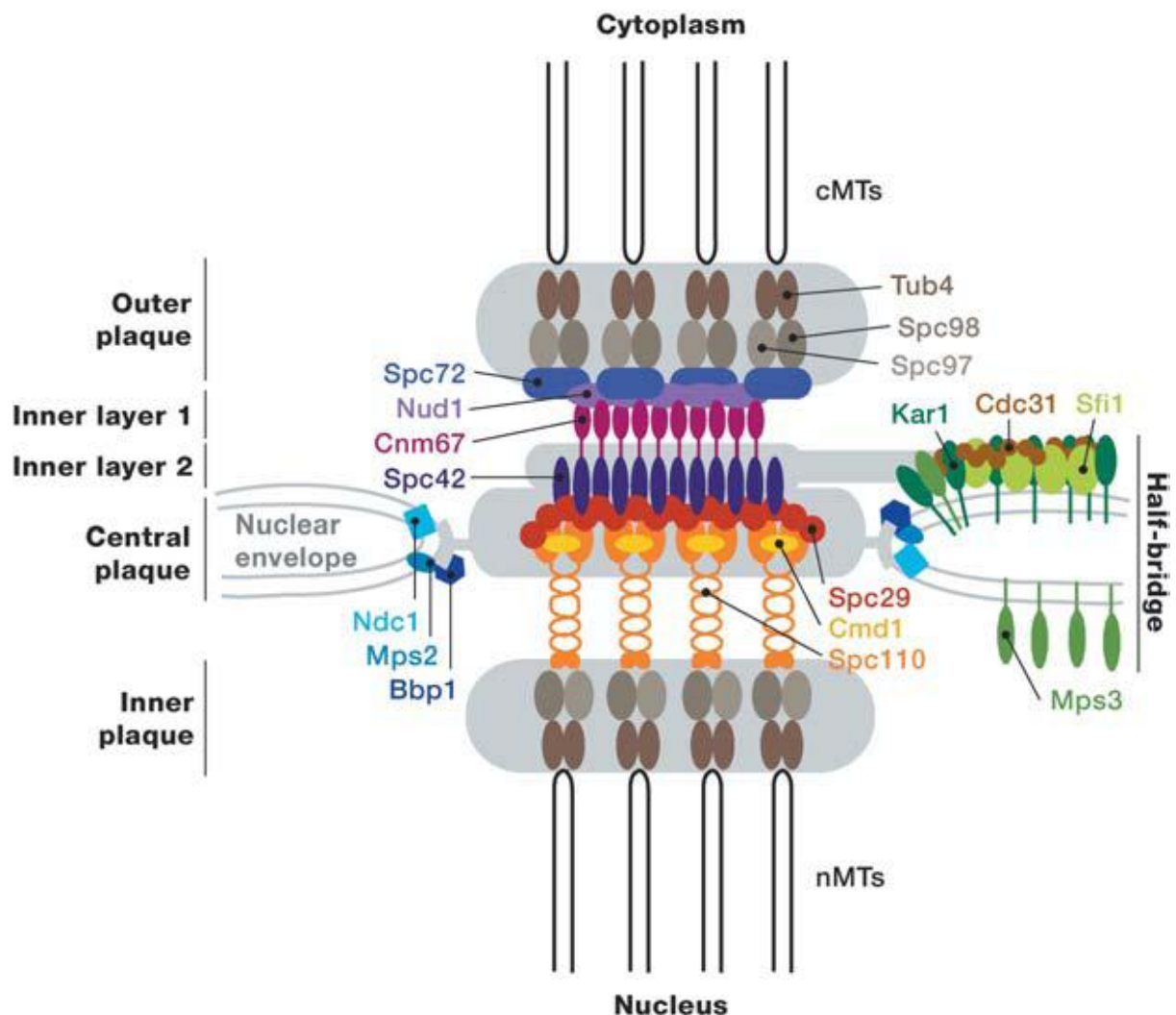


Figure 29 : Protein composition of the SPB. The positions of SPB components within the organelle are illustrated along with nMTs and cMTs and the nuclear envelope. A detailed description of protein-protein interactions within the SPB can be found in the text, and SPB components are listed in Table 1 (figure 2 from Winey and Jaspersen, 2004<sup>48</sup>).

The core proteins composing the SPB were defined as arranging mainly around a central hexagonal crystal core of the coil-coiled protein Spc42<sup>55,62,107,108</sup>; Approximately 1000 proteins are organized in trimers or dimers to form an hexagonal lattice seen by cryo-EM<sup>109</sup>. This later study also showed that the central crystal belongs to a newly defined layer of the SPB: the Inner Layer 2 (IL2). The over-expression of Spc42 used in<sup>107</sup> induced a lateral expansion of this lattice within the nuclear membrane plane resulting in the formation of a so-called superplaque. The N-terminus part of the Spc42 was described to interact in the CP with two other coil-coiled proteins at its nuclear face of the SPB: Spc110 and Spc29<sup>57,106</sup>.

Spc29 binds to Spc42 and Spc110 and was suggested as a regulator of Spc110 binding and a linker between the inner and the CP<sup>106,110</sup>. The tomographic study combined with a FRET study<sup>58</sup> suggested that Spc29 organizes under a less organized layer interconnected with Spc42. The striated region between the CP and the IPs is composed of dimmers of Spc110, which determines the distance between the plaques. The N-terminus of the coiled-coil Spc110 binds to Spc98 at the IP where the nucleation of the MTs is initiated<sup>111-113</sup>. The Spc42 C-terminus part is located in the IL2: here it interacts with the C terminus of Cnm67 that dimerise to serve as a spacer between IL1 and IL2<sup>114</sup>. In 2008, Zizlsperger *et al.* studied the coil-coiled interactions between the core proteins of the SPB<sup>115</sup> and resolved the crystal structure of Spc42. They conducted solution studies to show that coiled-coil peptides derived from Spc42 were forming parallel dimmers.

If the core structure of the SPB is inserted into the nuclear envelope, none of its proteins have been identified with a transmembrane sequence that could anchor the SPB and prevent its expulsion or help the insertion of the newly formed SPB. The study from O'Toole *et al.*<sup>55</sup> revealed the presence of 2 hook-like anchorage appendages tethered to the CP. Also attached to the CP, the HB is a filamentous multilayered structure that spans from one side of the SPB onto both sides of the nuclear membrane bilayer fused into a continuous layer at the point of SPB insertion. On the cytoplasmic side of the HB, an additional layer is connected to the CP and the IL2. A study from Sam Li<sup>59</sup> presented a convincing working model for the HB extension, the SPB duplication and the bridge separation. The Sfi1p-centrin complex they isolated is a 60 nm filamentous structure containing 15 repeats. The full-length structure containing 21 repeats would be therefore 90 nm long. This full structure could mirror itself on its C-terminal end to create a 150 nm long bridge between the two SPBs<sup>116</sup>. After the duplication of the HB, the satellite SPB is initiated at the N-terminal part of the distal Sfi1p-centrin complex, on the cytoplasmic side. However, the tethering of the satellite to the HB is still unclear.

Many EM studies were conducted to characterize the cycle of the SPB. It could be separated in four main steps: the HB elongation, the neo-formation of the SPB, the insertion into the nuclear membrane and the HB separation. Those steps were characterized with extensive use of wild-type and SPB duplication arrest mutants. First, during G1, the mother SPB organises the elongation of the HB, followed by the accumulation of amorphous material at

the distal end<sup>103,104</sup>. CDC31 MPS3, SFI1 and KAR1 mutants are arrested with a monopolar spindle lacking the HB<sup>116-118</sup> and the satellite. Second the satellite is organized in a layered structure, the duplication plaque, similar to the cytoplasmic half of the SPB<sup>103,104,106,119</sup> and the organization of the Spc42 into a crystal layer might play a critical role in this organization<sup>62,106,107</sup>. Third, the insertion of the newly formed SPB into the nuclear envelope and the assembly of the nuclear components of the SPB are triggered. The HB might partially retract underneath the duplication plaque and create a pore where the SPB could insert<sup>106</sup> and the frequent observation of nuclear pores in the vicinity of the newly inserted SPB suggests the implication of them in this process<sup>106</sup>. The organization of the IP follows to complete the formation of the daughter SPB. Finally, the separation of the bridge to let the two SPB organizing the spindle<sup>59</sup> might be physically initiated by the Cin8 and Kip1 proteins<sup>120,121</sup>.

Over the years, a large and detailed amount of knowledge has been accumulated about the SPB, its function, its structure and its dynamics. The parallel development of new high resolution *in situ* methods<sup>122</sup>, combined with advances in the protein folding prediction<sup>123</sup>, protein localization and orientation<sup>48,58</sup> and protein crystallization<sup>124</sup> methods are powerful tools to understand the functioning of its molecular mechanisms. Al-Amoudi *et al.* successfully docked the crystal structure of the cadherin protein into the native epidermal desmosome. Using a comparable approach for the SPB in *S. cerevisiae*, the precise identification of the proteins' localization through their EM densities might bring new insights into the functioning of this complex structure during the 4 main physiological steps that were previously described. The approach used for this study requires fine skills to prepare the sample and significant training was required. To facilitate the learning process while acquiring useful datasets, we selected as the first mutant, the Cdc4 ts mutant. Characterized with the two SPB side by side, it could be used as a control and as a first WT structure for the study.

At the beginning of this project, some of the parameters were already known like the use of the EMPACT 2 or the HPM010 machine for the preparation of the High Pressure Frozen samples, and the subsequent use of the cryo material, as already established in the Frangakis group (UltraCut 6 cryo-ultramicrotome, biotwin Ice and Polara microscopes).

## **b. Detailed observation of the wild type: the first step towards high resolution of molecular complexes' interactions**

### **i. Wild type cell synchronization with $\alpha$ -factor**

As previously introduced, our strategy consisted in resolving the structure of the SPB at four carefully selected time points. We aimed at imaging WT structures as a control and the best solution for that was to focus on a culture of synchronized WT cells: ESM 356-1. One of the most common synchronization is done using the mating factor  $\alpha$ , on mating type "a" cells. After the release from  $\alpha$ -factor, the cells can be followed and fixed at the desired time point. However, the preparation of the sample might take some time (filtering and yeast paste filling into the carrier) that is not conveniently quantifiable. So between the imaging and the freezing (done in two different rooms), a time lapse lets the cells continue their cycle, resulting in an imprecise time-point freezing. Therefore, we decided not to push this approach further.

### **ii. Thermo-sensitive mutant synchronization by temperature shift**

The thermo sensitive mutant *cdc4-1* (*ts Cdc4-1*) has no characterized alteration of the SPB<sup>10310456</sup> after the temperature shift and gets homogeneously synchronized after 2 hours at 37°C. The literature describes the two SPBs fully duplicated side by side, connected by their HB<sup>103104</sup>, in the direction of the newly formed yeast bud. We confirmed it with conventional plastic embedded cells, using this picture gallery as a reference for our later screening.

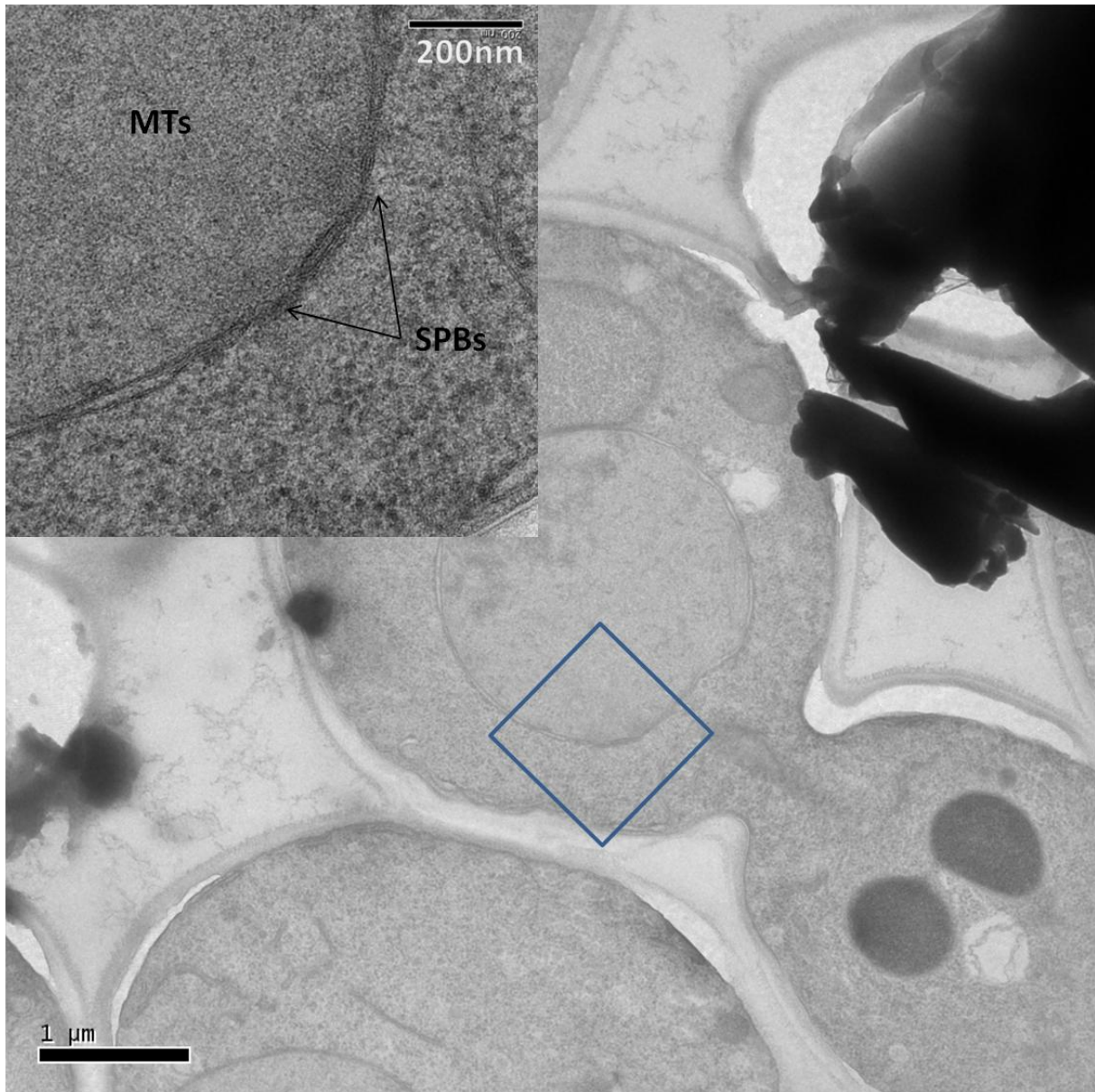


Figure 30 : The large overview of the cell shows the nucleus with the 2 SPBs side by side linked by the bridge (magnified box), facing the bud. The MTs are interdigitating prior to the SPB separation.

This particular organization facilitates the localization of potential samples by acquiring images of the cells directly at the point where we could identify from a low magnification and very low dose image, the nuclear envelope beside the bud neck of the cell. For single frame two dimensional (2D) imaging, the second image could be done using the maximum dose possible (around  $2000 \text{ e}^-/\text{\AA}^2$ ) after centring by eye the structure of interest, to obtain a good overview. In tomography, the centring of the sample could be done using the computer controls, defining the centre of the tomogram directly on the low magnification image.

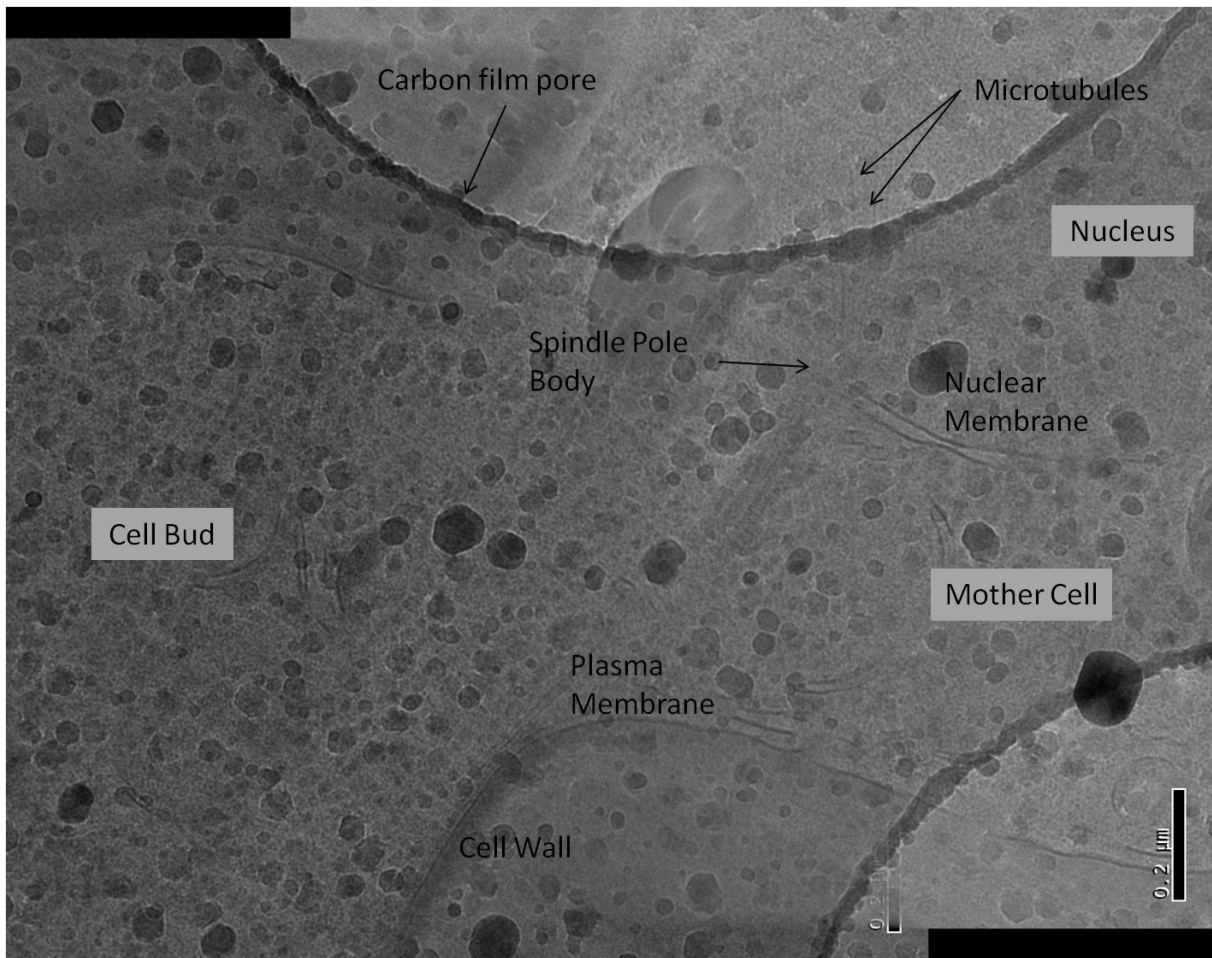


Figure 31 : Cryo electron micrograph of a budding yeast. Heavy ice contamination can be observed. The nuclear membrane is clearly distinguishable, the SPB is embedded and MTs are pointing at it. Two pores of the C-flat carbon film can be seen at the top and the bottom right.

### iii. Cell behaviour in cryo-protectant solution

Ashraf Al-Amoudi and other publications already described<sup>64,82,122,125,126</sup> the advantages of using a cryo-protectant in the sample preparation. Despite the very good freezing property of the yeast paste (see method chapter), we decided to test the advantage of using a cryo protectant in the cell culture. Several conditions were tested to avoid causing an osmotic shock, previously described as deleterious for the endocytosis<sup>127,128</sup> and therefore potentially intrusive for the mitotic spindle.

We grew the 2 yeast strains (WT ESM356-1 and mutant RH207-1) in YPAD pure or completed with dextran or ficoll as a cryoprotectant and measured their growth rate over time by OD.

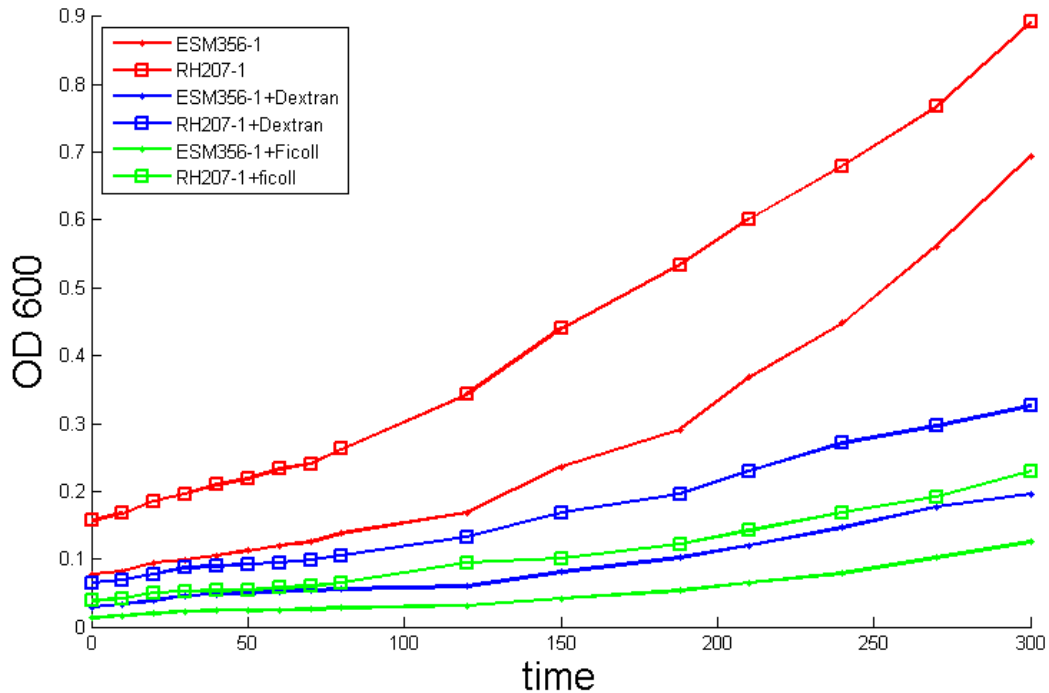


Figure 32 : Growth curves of the wild type and the mutant yeast strains at 30°C with or without cryo-protectants.

The growth rate in dextran and ficoll is comparable and they do not prevent the cell growth. However, the log phase is weaker and the cell cycle seems slowed down. We haven't analyzed in detail the reason for this slower rate, but the discussions raised the following potential reasons: the high viscosity of the medium reduces the growth rate, the 20% of dextran or ficoll lower the amount of nutrients available or the oxygen does not get renewed during the agitation of the flask due to the high viscosity. However, our discussions with yeast experts lead us to conclude that this should not alter the cell cycle as they were still growing and doubling their population every 3 hours (compared to every 90 minutes in normal conditions).

Importantly, the filtering of the cells grown in dextran or ficoll took over 7 minutes. However, we kept the cells at 37°C during the filtering, resulting in a short temperature release time prior to the freezing.

The sectioning quality didn't seem to be modified by the presence or the absence of cryoprotectant and the freezing quality was also comparable. The very good freezing property of the yeast paste, often used itself as a cryoprotectant to freeze other cell types<sup>129</sup>, might explain it.

### **c. Data collection**

#### **i. Choice of the HPF**

Two different High Pressure Freezers are available at EMBL. Those two machines use different approaches to freeze the samples, and therefore each might be suitable for different purpose. Different users had various opinions about those two machines and to appreciate which one is most adapted for this study, we tried both.

The HPM010 has large aluminium carriers, with various depths from 50µm to 300µm. The size of the carrier might appear advantageous at a first glance, allowing the user to freeze more sample per shot. However the aluminium carrier cannot be trimmed directly with the cryo-trimming knife. This forces us to break the sample out of the carrier and remount it on a pin or a Leica EMPACT2 carrier using the cryo-glue (see method chapter).

The EMPACT 2 has smaller carriers made of copper, plated with gold. The available depths are 100 and 200µm. The smaller size of the carrier, hold into the RTS made it easier to fill with the yeast paste. The possibility to directly trim the carrier containing the sample gave us 2 advantages: first, the sample was maintained by the whole carrier, facilitating the trimming and the sectioning. Second, the possibility to work directly into the carrier without remounting the sample allowed us to section at -140°C as well as -160°C.

The sectioning of the yeast paste at those two temperatures was comparable and neither could be considered to give better results.

Our observations under the electron microscope could not differentiate the quality of the freezing between the HPM010 and the EMPACT 2, and both gave us satisfying results.

Those observations naturally lead us to use the EMPACT2, easier to manipulate during the freezing and afterwards during the sectioning.

#### **ii. Electron microscopy grid selection**

The main advantage of the lacey grids is their reduced amount of support film while being very robust. For a 2D imaging, they offer many opportunities to image the structure of interest directly without interference of the support film. However, when multiple imaging is required like in our case (tomography), their use has to be pondered. In the case of plunge frozen samples (*e.g.* purified SPB) the network heterogeneity is an advantage, having the

structure on interest mainly in between the holes, trapped in ice. The larger the holes, the thinner the ice, improving therefore the imaging quality, until the holes get too large and the ice break. For plunge-frozen samples, lacey grids are preferred over C-flat grids for the following reasons: i) the surface tension inside the holes gets important, limiting the water removal from the grid ii) the blotting needs to be much longer to remove as much water as possible. Often the sample at the periphery of the grid gets too dry while the centre of the grid has still too much water.

But in the case of sections which are often distant from the support film, with sparse contact regions, the restrained amount of support from the lacey film reduces the stability of the section. The imaging is therefore more problematic than for plunge-frozen samples. In contrast, the use of C-flat film coated grids offers a larger surface of contact for the sample (ribbon), reducing its flexibility. The regular arrangement guarantees finding a region of interest (SPB) on top of a hole. This strategy obviously applies when the sample contains many regions of interest. The use of the 2 $\mu$ m diameter holes (4 $\mu$ m spacing) increased also significantly our imaging capacity over the 1-2 C-flats (1 $\mu$ m holes, 2 $\mu$ m spacing).

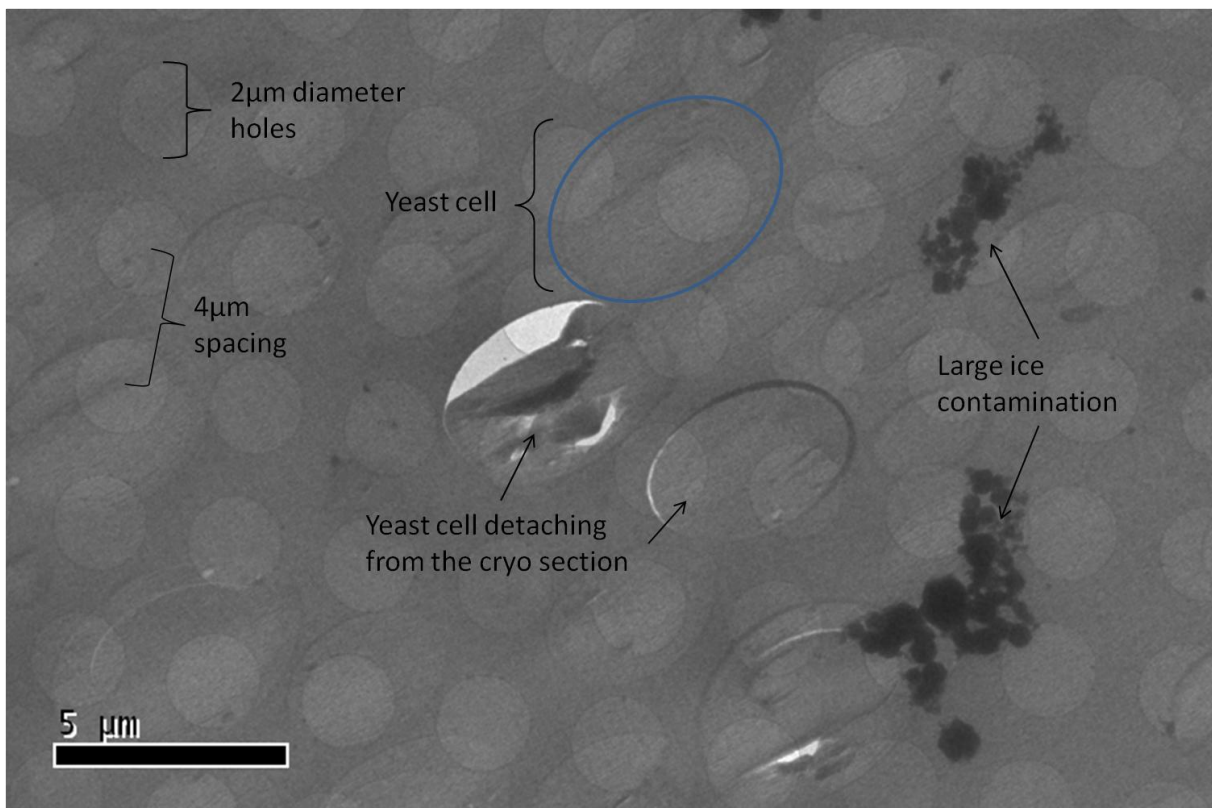


Figure 33 : Overview of a cryo section, on top of a C-flat. Some of the cells were detached from the section; we can also observe contamination of large ice crystals.

#### **d. The use of mutants to observe selected time points in the cell cycle**

##### **i. Cdc20 mutant**

At the start of my PhD work under the supervision of Ashraf Al-Amoudi, I used the *cdc20* mutant yeast strain for my training. The *cdc20* mutant has been extensively described in the literature<sup>3</sup>: it is unable to divide the aligned spindle, leading to a proper alignment along the bud axis of the cell, prior to anaphase<sup>3,104</sup>. Another known characteristic of the *cdc20* is to have an increase of the number of MTs of approximately 60%<sup>3</sup>. The increase in MT number facilitates greatly the search for the spindle in the cryosections and therefore is a very good model for training how to do cryo-EM (CEMOVIS).

The *cdc20* cells were previously grown in restrictive conditions, spun and mixed gently with fiducial gold markers before HPF with the EMPACT2. The fiducial gold gave a slight pink coloration to the frozen sample. Those gold markers were added to be later used as fiducial markers for the tilt series alignment. As they didn't penetrate into the cells, the markers were often not observable in the field of the camera. We therefore decided not to continue adding them prior to freezing.

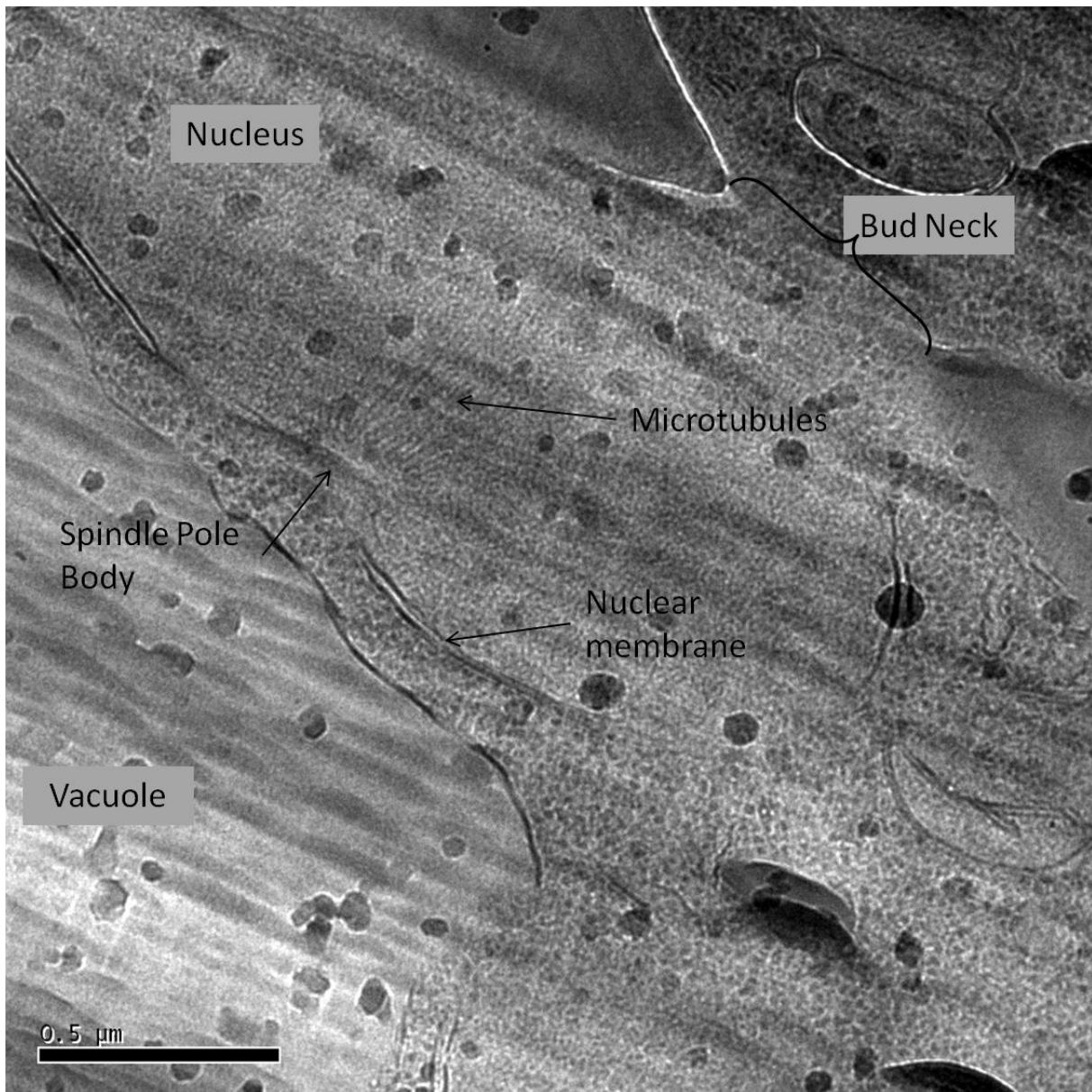


Figure 34 : A clear view of a SPB associated with the spindle. Some ice contamination is observable over the whole sample. The section is tough well preserved. The spindle is formed and aligned in the direction of the bud; the opposite SPB facing the bud is probably on the next cryo- section.

## ii. Cdc4 mutant, one mutant to bind them all

As explained previously, the first step in the project was the reconstruction of a native structure to use as a reference model on which the following steps of the study could be aligned. The physiological properties of the Cdc4 mutant were suitable to establish this first model.

## **e. Tomographic results**

### **i. Cryo-electron tomograms from CEMOVIS sections**

Over more than a year, 24 tomograms containing a structure that could be identified as SPB in the tomograms were acquired and reconstructed with alignment errors from 1.2 pixels to 2.3 pixels. After further investigation and visual inspection several aspects of the SPB could be visualized.

#### ***1. The central plaque, the outer plaque and the Spc42 central crystal***

The SPB was historically described in several steps. The first observation reported the existence of the CP and the OP only. The other structures were discovered only later. While collecting tomograms of SPBs, without image processing, the CP and the OP could already be identified when the tomogram was properly oriented.

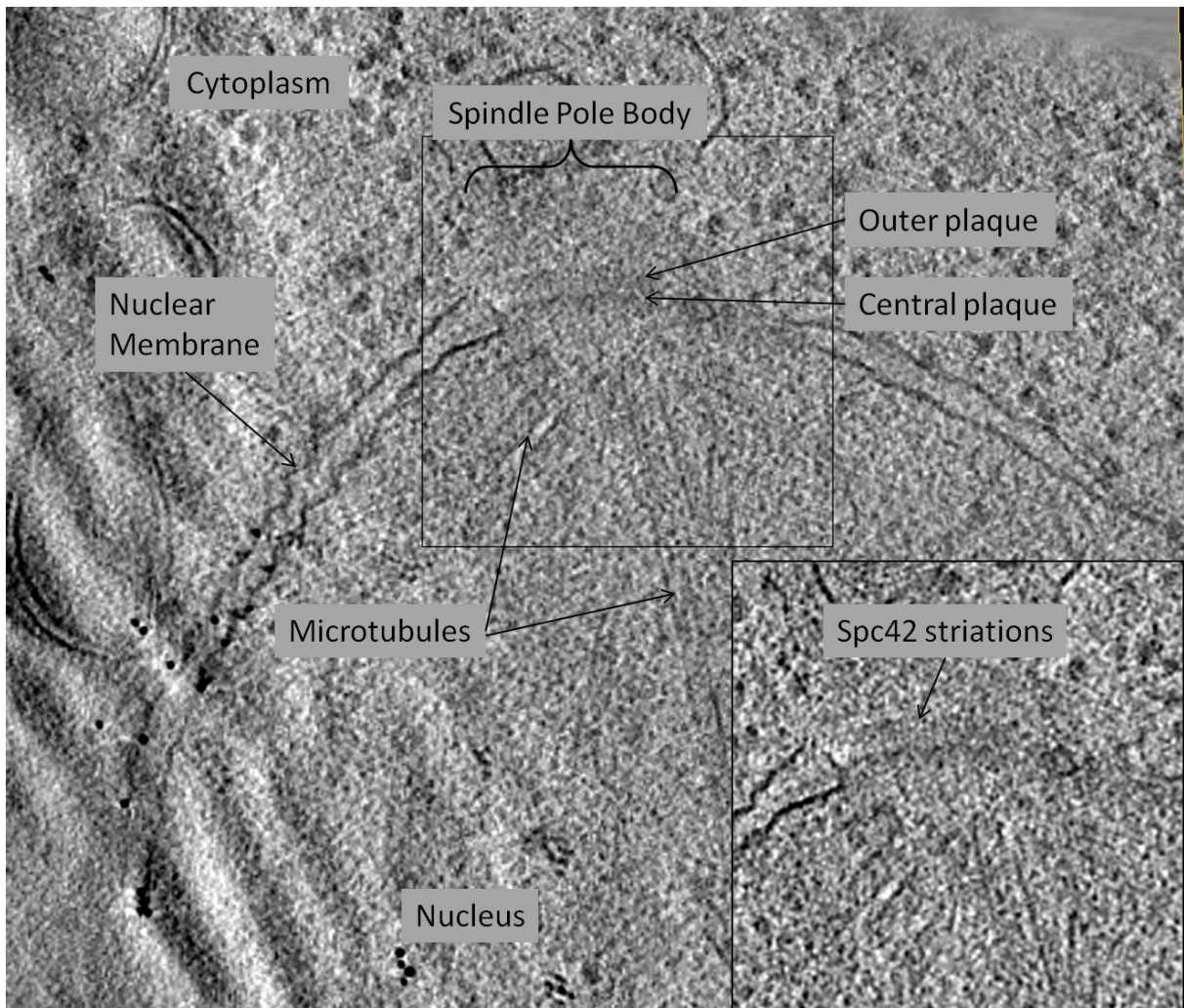


Figure 35 : Projection of 10 computational slices of a SPB. Image contrast has been adjusted for visualization purpose. The insert is a magnified, filtered and adjusted display of the SPB. Striations are apparent between the two dense CP and OP. Alignment error 1.64 pixels, defocus acquisition  $-6\mu\text{m}$ . Pixel size 1,194nm.

In Figure 35, the SPB inserted in the membrane can be localized by the MTs pointing at it. On the 2 times binned tomogram, projecting 10 slices onto one enhance the SNR and after a Gaussian filtering with a sigma of 2, it becomes possible to observe a striation with a regular spacing as described in the literature<sup>55,62,107</sup>, this corresponds to the Spc42 central crystal, located at the IL2, between the CP and the OP.

To accurately measure the spacing of the striation, a sub-tomogram was extracted from the binned data and XY slices were projected along the Z axis. After localizing the repeat, the region identified by the rectangle black box in Figure 36 was projected along the Y axis. The spacing on the plot profile between the striations is of 8 to 10 pixels. The resulting distance between the striations is therefore of 10,746 nm, corresponding to the 109Å measured by E. Bullitt<sup>62</sup>.

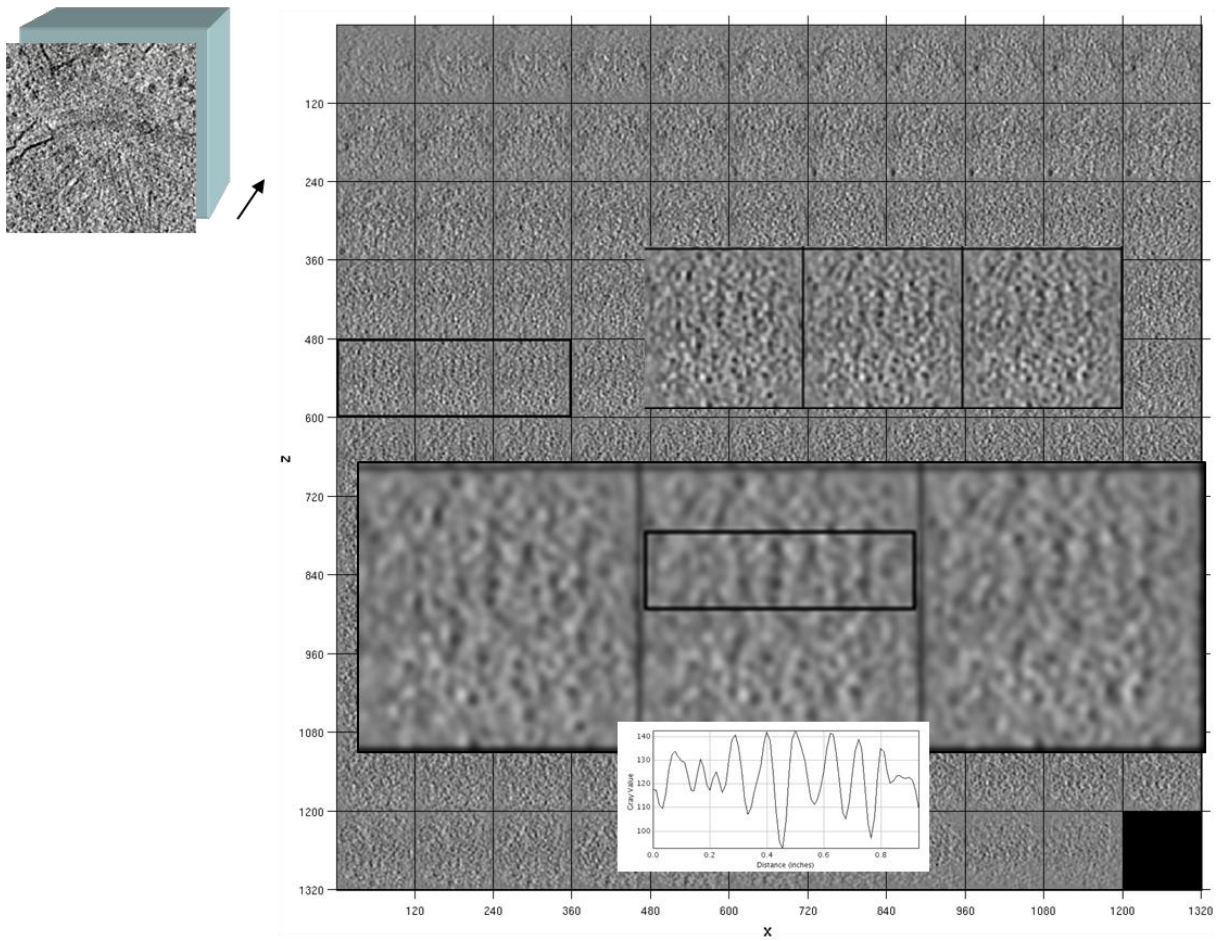


Figure 36 : Projection of the tomogram along Z around the SPB. Three electronic slices are magnified and then gauss filtered. The striation of the CP can be observed. A density plot along the X axis shows a clear repeat pattern with a spacing of 10,7nm.

To identify further proteins of the SPB, we tried using the Spc42 central crystal as a docking molecule for the sub-tomogram averaging (Figure 37). As the Spc42 crystal structure has been resolved <sup>115</sup>, we generated the EM density from the crystal.

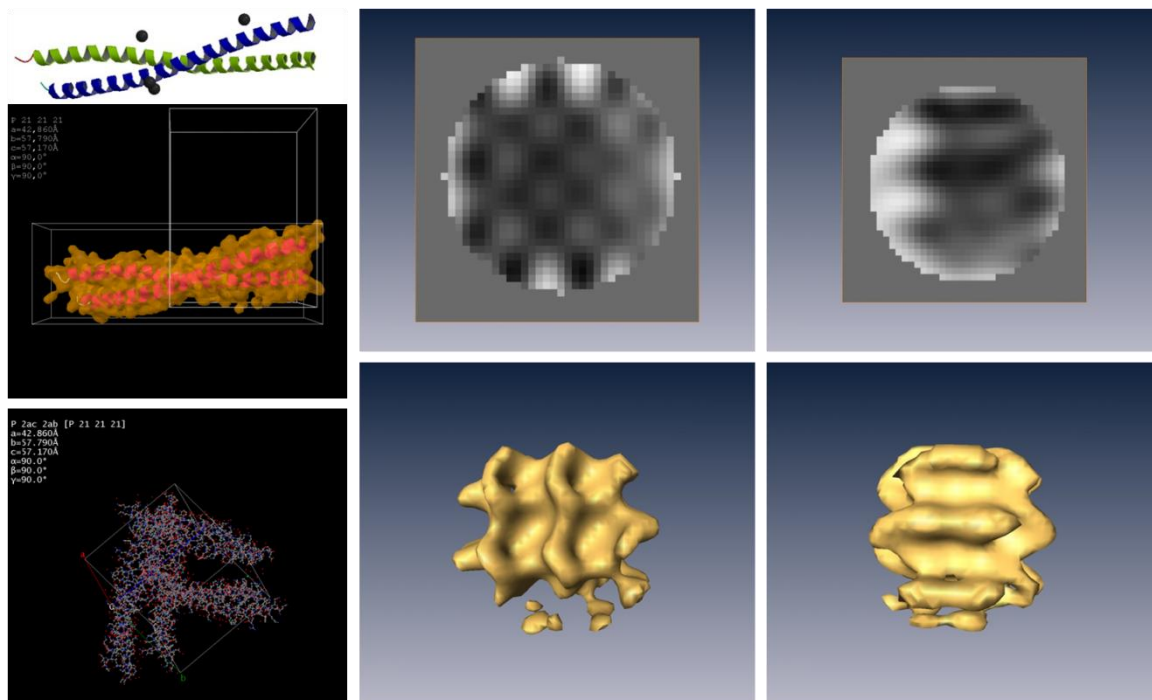


Figure 37 : Spc42-centralCrystalStructure - From the protein data bank, we could create the putative electron microscopic density map. We used this EM density as a visual reference to comparatively recognize regions of the SPB which could be the Spc42 central crystal. This structure was also used for further template matching attempts.

The pattern generated in the centre of the crystal fits well with the structure observed previously<sup>55,62,107</sup> and the one we observed during our preliminary observation (Figure 37).

E. Bullitt<sup>62</sup> calculated that the central crystal was composed of approximately 1000 molecules of Spc42, arranged in trimmers of dimmers, resulting in approximately 167 sub-volumes within the central crystal. To localize them and to reduce the computational time, the densities were identified on the binned tomogram, marked and used as central averaging points for the sub-tomogram averaging on the full resolution tomogram. Only the CP and the OP could be retrieved (Figure 38) with this averaging but the regular lattice described previously<sup>55,62,107</sup> could never be identified or averaged. A similar approach was taken on all other tomograms where the SPB could be identified. Only the OP and the CP could be averaged in the very best case, never the IP.

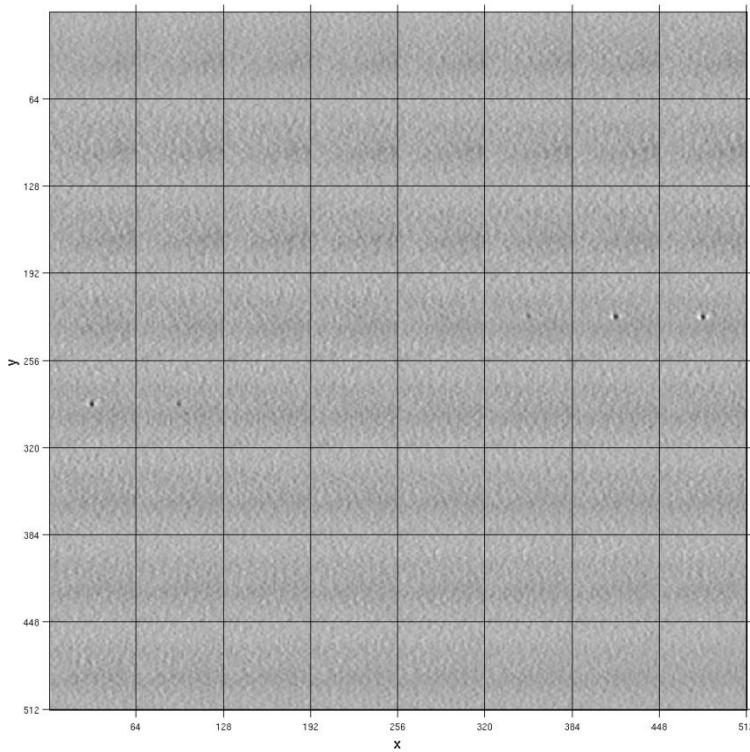


Figure 38 : Sub-tomogram averaging of the Spc42 central crystal using the striations as central reference. The OP and the CP can be recovered but no homogeneous structure.

## 2. The half bridge

Another key structure of the SPB is the HB. Central organ of the SBP duplication, the major work of Sam Li<sup>59</sup> gave new insights on the potential organization of the HB. As for the Spc42 protein, a crystal structure of the Sfi1p-centrin complex was available and could be used to dock into an EM density.

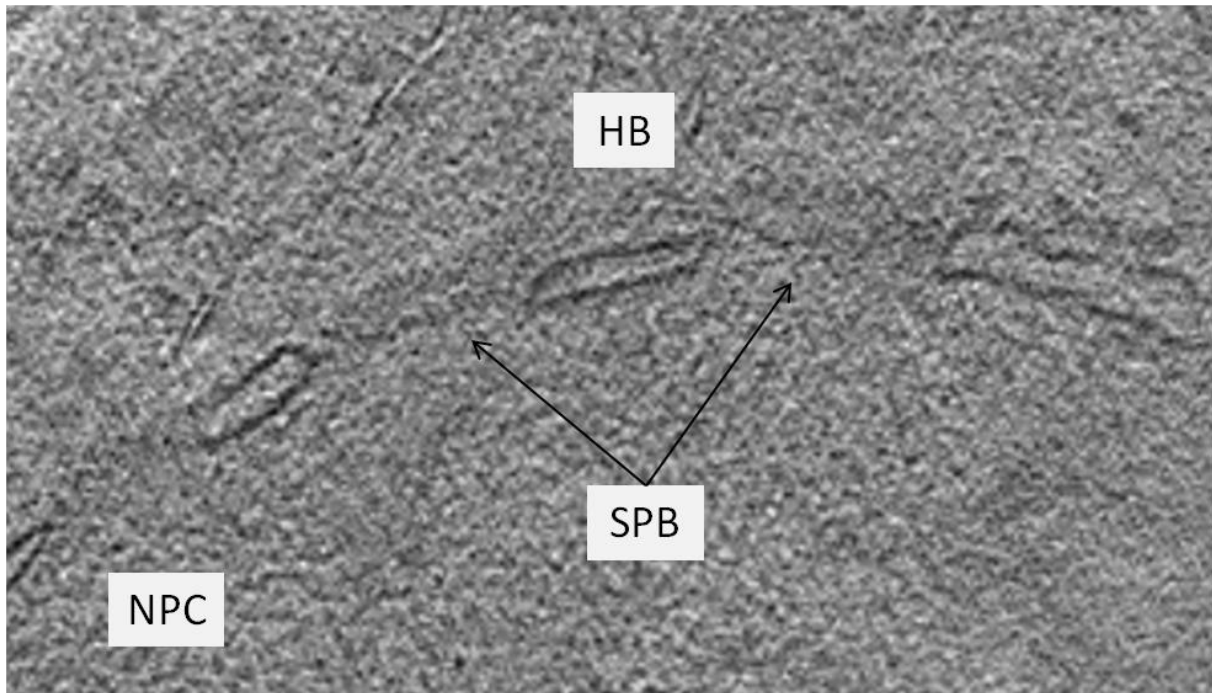


Figure 39 : The two SPBs are side by side, linked by the HB. The CP and the OP of both SPB can be recognized, but no regular lattice could be identified. The HB is not as densely marked as in the text books. Alignment error 1.92 pixels. Defocus -6 $\mu$ m. Pixels size 1.194nm.

On this tomogram, the clear recognition of the two SPBs (OP and CP clearly marked, MT pointing towards them in other orientation of the electronic slice), made unambiguous the location of the HB. Heavy beam damages towards the end of the tilt series lead to a precipitation of the proteins, increasing their contrast while reducing the amount of high frequency information. The HB cannot be identified in this sample or in any of the collected data. Sub-tomogram averaging was therefore not possible.

### *3. Nuclear microtubules*

While focusing on the SPBs, many MTs in every orientation were imaged. Two strategies were tried to extract information about the lattice.

#### *a. The microtubule central line*

Manually selecting the MT midline, sub-tomograms were extracted and manipulated to recover the 13 protofilaments lattice of the MTs. Different strategies were adopted, taking into account the missing wedge or not, changing the mask to spheres, cylinders, tubes of different sizes, did not converge to a coherent averaging.

### b. The microtubule helix

Using the previously selected MT midline, a 13 pitch helix reproducing the MT lattice was used to extract the sub-tomograms used for the averaging. The use of this strong template resulted in creating a MT rather than extracting it from the dataset. The use of various masks shapes for the averaging could not overcome the too strong bias induced by the initial helix. Different pitches and lattices always resulted into this strong template bias.

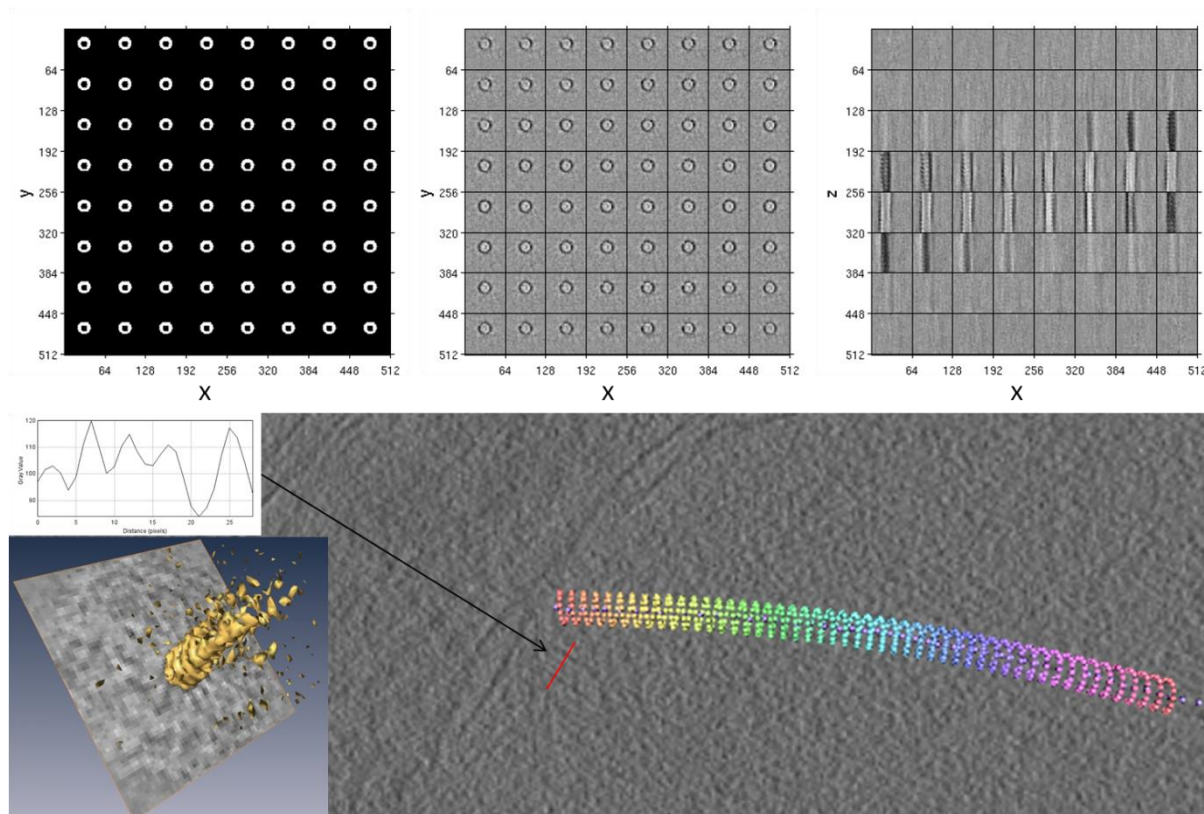


Figure 40 : The use of a strong filter or a constrained template to average the MTs leads to a template bias. Less constraining parameters did not converge either. The red line corresponds to the plot profile axis. Four distinct peaks can be seen, corresponding to the outer wall and the lumen of the MT.

The quality preservation of the sample could however be assessed. As an example, the MT pointed by the arrow to the red line shows a similar structure to previous study<sup>130</sup> and diverges from plastic tomography by the characterization of two densities within the MT lattice.

### f. Plunge freezing of isolated of SPBs or Nucleus

In parallel to the cryosectioning strategy, we collaborated with the Pr Dr Schiebel laboratory at ZmbH, Heidelberg. Linda Gombos, post-doctorate in the lab, purified yeast nuclei and SPBs. We aimed to isolate SPBs with less background to acquire tomogram from which to

extract sub-tomogram for averaging and matching with the cryo-sectioned samples <sup>62</sup>. Several attempts to purify the SPB were performed. The sample purity and the complex assembly were verified by western blotting.

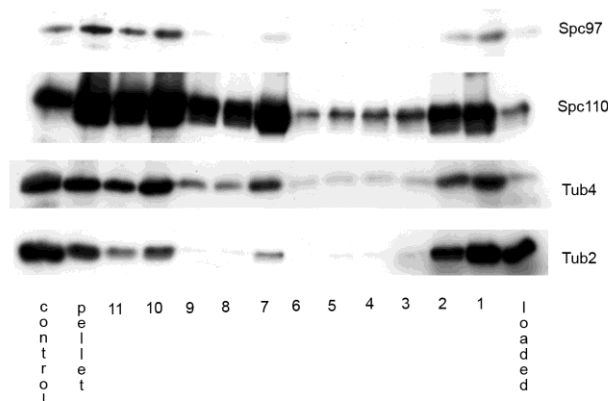


**Figure 41 : Westernblot of the purified SPB. The fraction 7 contains all the desired markers of the SPB (courtesy of Linda Gombos).**

However the protein complex was no longer structured when we looked at them in the electron microscope. Negative stain and plunge freezing of native and fixed sample were tried. Plunge freezing of whole yeast nuclei or lysed by brief osmotic shock were also attempted unsuccessfully.

### **g. Discussion**

The functioning of complex machinery is often hard to understand although the physiology can easily be described. For example, a car can be identified by its characteristic shape and by taking snapshots of it in different situations. Without knowing how the mechanics work, it is easy to figure out its role. But not to understand how it literally works and how it was constructed.

Following the idea that the identification of each sub-unit of a structure could lead to a clearer understanding of its functioning, we decided to get a molecular map of the structure of the SPB in *S. cerevisiae*. Not only taking one static superficial image (2D), but by acquiring three dimensional images of the SPB, at molecular resolution in different stages of the life cycle. Our overreaching goal was to identify some of the key proteins, their arrangement

with regard to each other in three dimensions to get new insights into the SPB duplication, insertion into the plasma membrane and separation.

To address this question, the sole method to date that combines a molecular imaging in a cellular (or natural) context was, and is still, the acquisition of three dimensional images (tomograms) on hydrated sections collected from vitrified sample (CEMOVIS/CETOVIS). We decided to focus the first part of our work on a sample that could be used as a reference for the later stages (the four stages described in the introduction). Therefore, the use of samples that were physiologically affected by mutations was ruled out for the first step.

The Cdc20 mutant is characterized by a strong increase in the number of MTs, but the size of the SPB is also affected to compensate it. This consideration prevented us from using this sample for our study. However, for training purposes, the larger structure (4 times more MTs and 2.3 times bigger SPB <sup>3</sup>) facilitated the identification of the SPB and MTs. The larger structure of the SPB in this mutant could have been used as a template, scaling the extracted values accordingly, for the later parts of this study. However the divergence from the native structure would have been hard to characterize. Therefore, we selected the Cdc4 mutant. The Cdc4 mutant is not described in the literature with a physiological alteration of the SPB and the two structures stay side by side, connected by the HB, increasing the chances to have two WT structures in the same imaging frame (Figure 39).

After the selection of the mutant, the sample preparation was considered. The stress induced on the cells might be deleterious and special care needed to be taken to reduce the stress on the cell prior the cryo-immobilization. The state of the art in sample fixation of entire cells is HPF. However, stress can be induced prior to this high quality fixation: some of the stresses often presented are the centrifugation for pelleting the cells, the use of toxic carriers (copper, aluminium) that rapidly affect the cells, dehydration or more generally osmotic shocks and finally temperature shifts.

The yeast paste presents very good freezing quality and has been used as a cryo-protectant for some studies in the past. To be sure that most of the cells would be adequately frozen the use of cryoprotectant was suggested. We tried ficoll and Dextran and tested the cell behaviour in solution containing 20% cryo-protectant. Our results showed that the cells grow properly in both of them and no significant alteration of the growth could be observed.

The filtering of the yeast to collect the yeast paste took more time and special care had to be taken to keep the thermo-mutant cells at the restrictive temperature during the filtering and until the actual cryo-fixation. The yeast paste was then collected and placed into gold plated membrane carriers that, to our knowledge, were not intoxicating the cells. The use of the rapid transfer system (RTS) ensured a rapid manipulation between the yeast paste collection and the freezing.

The sections collected were typically 110 nm thick. This thickness is enough to contain one entire SPB and yet does not compromise the resolution. To locate the SPB, we relied on the presence and orientation of MTs aligned towards the cell bud. The textbook pictures of stained sections describe the SPB as a denser region in the nuclear membrane. But our work of cryosections of SPB shows it rather homogeneous and with a lower density, comparable to that of nuclear pores. The necessity to acquire the lowest dose possible images for the structure identification prior to the tomographic acquisition was a limiting factor for the initial mapping. This resulted in having several tomograms containing only partially longitudinal MTs pointing outwards from the section and having no SPB in the final reconstructed volume. This significantly slowed down the data collection process and the selection of the best sample was done *a-posteriori*.

The use of gold fiducial markers at the surface of the section, deposited after the collection of the sections in the ultra-cryo-microtome was used for a short period according to the procedure described by *Masich et al.*<sup>131</sup>. The removal of the isopropanol with liquid ethane often resulted in having a layer of liquid ethane at the surface of the section and this significantly affected the SNR. However, in some rare cases like the SPB presented in C-e.i.1 (p81), the sample could be acquired and reconstructed despite the layer of liquid ethane. This particular tomogram was reconstructed using the marker less alignment program Alignator, giving a better alignment error and reconstruction.

The crowdedness and the high water content of the yeast resulted in a very low SNR in the tomograms. The identification of the structures was facilitated by projecting several slices along a defined axis (typically 10 electronic slices). This artificial enhancement was meant to facilitate the structure's recognition "by-eye". Identified proteins like Spc42 (forming the central crystal) were then manually marked to proceed further with sub tomogram

averaging and protein structure docking or template matching approaches. The aforementioned crowdedness prevented us from identifying regions of interest or to match 3D EM structures within the SPB. Our approach relied essentially on our ability to initially isolate the Spc42 central crystal to further recognize the proteins tethered to it. We could formally identify some sub-elements of the Spc42 central crystal by measuring the spacing of the sub-units (107Å) and comparing it with the results obtained by E. Bullitt (110Å)<sup>62</sup>. The small difference could result from the measurement method combined with the compression of the sections (sectioning orientation orthogonal to the SPB causes the compression in the width of the SPB). Also, the layers composing the SPB are not as clearly identifiable as in FS material<sup>55</sup>. Averaging procedure could not converge to the three plaques bound by the two IL. The thickness of the SPB could therefore not be confirmed from our samples. Finally, the IP was not identifiable in our data and the corresponding region was not homogeneous and dense. It appeared more amorphous than layered. We could imagine that the contrasting of the plastic sections increases the density of the IP, also explaining the later discovery of the IP with the use of HPF and the improvement of the FS procedures.

To extract other information from the tomogram that were collected, we also worked on the easily identifiable MTs. As it was used as a marker for all the tomogram acquisitions, all the collected datasets contained at least one MT. We tried to recover the MT lattice also by subtomogram averaging. The fundamental difference between plunge frozen MTs and cryosectioned MTs is the biological environment in which they are placed. The intensive work on the MT associated proteins showed that proteins have preferential localization along the MT. By recovering the MT lattice, we were planning to use the alignment parameters to align sub-regions of the MTs and to compare them. The goal was then to differentiate the MTs ends and to characterize potential subregions. Unfortunately, the SNR resulted in averaging the MTs along the initial template and could not converge to an existing structure of the MT.

Finally, to improve our SNR and generate a model that could be used comparatively with our tomograms from sections, we collaborated with Pr Elmar Schiebel's lab to obtain purified SPBs and isolated nuclei for plunge freezing. We could not obtain structured SPBs and all the

purified solutions were unstructured aggregates of SPB proteins. The isolated nuclei were generally too thick and resulted in a low SNR that could not be used for reconstruction.

Overall, the project faced mainly the limit of the SNR that is found low in yeast, due to very high water content and protein density. Extracting the cells prior to the HPF would be an efficient solution to improve the SNR of the sample, but the “close-to-native” state that is aimed at in cryo-sectioning would be then lost.

To my knowledge, only two publications so far were able to produce sub-tomogram averaged structures and protein docking in vitreous sections. Those structures of interest were extra cellular material where the water and protein content is significantly lower than in intra-cellular material, resulting in a higher SNR and limited diversity of native structures<sup>122,132</sup>.

In the field of the SPB, new proteins still remain to be discovered and the dense packing is an obstacle to the CEMOVIS approach.

## Part IV: the mitotic spindle in *Xenopus laevis* is organized at a higher level of complexity

---

*«On fait la science avec des faits, comme on fait une maison avec des pierres : mais une accumulation de faits n'est pas plus une science qu'un tas de pierres n'est une maison.»*

*[Henri Poincaré]*

## D- The meiotic Spindle in *Xenopus laevis*

### a. The Meiotic spindle self assembly in the egg extract

The meiotic spindle is a complex machinery, tightly regulated in space and time throughout the cell cycle to ensure a proper equal segregation of the genetic material from the mother cell into the two daughter cells. A failure happening during the chromosome segregation would lead to aneuploidy and altered phenotypes for the daughter cells. A number of key molecules are part of the regulatory system that controls meiosis and mitosis. The fine tuning and regulation processes of spindle assembly and function prevents the occurrence of defects that would also impair the development of the organismus <sup>91</sup>. To study this machinery, the meiotic spindle of *X. laevis* have been extensively used over the past decades <sup>36,91</sup>. The capacity to reproduce the cell cycle into a test tube has been a major advantage as protein depletion can be used in this semi-*in vitro* system to study protein function and regulation in the spindle assembly <sup>36</sup>. Major discoveries were done by making analogies between the meiotic spindle of *X. laevis* and other vertebrate lineages like mammalian cells <sup>91</sup>. Despite understanding how proteins function in the mitotic spindle, many crucial aspects of the spindle assembly remains elusive: the architecture of the spindle remains largely unclear and several attempts were done to characterize and to understand more precisely this large and complex structure <sup>1,2,36,60,133</sup>.

In the case of the meiotic spindle, the highly dynamic structure is reaching a steady-state where all the MTs grow and shrink constantly, in a relatively unlimited environment (1 mm diameter eggs, or eppendorf). The size and shape are comparable from one extract experiment to another and from different experimentalists within the same species <sup>8,60,134,135</sup>. However, evidence showed that dose dependent cytoplasmic factors are responsible for the scaling of the spindle <sup>136</sup>.

One of the fundamental building blocks of the spindle is the MT pool. The MT polymer is a complex assembly of  $\alpha$  and  $\beta$ -tubulin sub-units, aligned to form a protofilament. Thirteen of those protofilaments are then organized into the tubular structure. The MTs interact with each other to generate pulling and pushing forces within the spindle at various stages of the cell cycle. The head-to-tail arrangement of  $\alpha$  and  $\beta$ -tubulin sub-units result in a polar tubular structure where both ends have different characteristics. Both subunits incorporate

guanosine triphosphate (GTP). Shortly after, the  $\beta$  tubulin hydrolyzes the GTP into a guanosine diphosphate (GDP) that favours a curvature to the protofilament outwards from the MT<sup>137</sup>. The hydrolysis of the GTP confers several properties to the MTs<sup>138</sup>. First, the distinction between the plus and the minus end, second the differences in the protofilaments lattice. The MTs interact laterally through molecular motors<sup>36</sup> and bundling proteins<sup>41,139</sup> in parallel and anti-parallel fashions, the orientation being recognized via the  $\alpha\beta$ -tubulin orientation. The end which incorporates most of the tubulin dimmers and is the most dynamic is defined as the “plus end”, opposite to the more stable end, often capped by protein complexes, called “minus end”. The difference in the dynamics of the two ends has been characterized by ET, using the 3D morphology of the MT end on tomograms<sup>140</sup>.

The spindle is a bipolar array of MTs. The interaction between all the MTs creates a scaffold where the majority of their plus ends points towards the chromosome mass while the minus ends point towards the spindle poles and are focusing onto the centrosome. The bipolar organization of the spindles results in a homogeneous overlapping of the MTs in facing orientations at the midzone around the chromosome mass<sup>5</sup>. Speckle microscopy studies also gave evidence of poleward flux of tubulin, confirming the dynamic instability, where the plus ends of the MT continuously grows while the MT itself goes backwards<sup>36,141</sup>. LM studies using the End Binding protein 1 (EB1) converged with the previous EM analysis regarding the preferential orientation of the MTs within the spindle<sup>142-144</sup>. However, no direct LM method to detect the minus end is currently available<sup>19,60</sup>. Combined with the relative difficulty in imaging individual MTs within the spindle<sup>60</sup>, very little is known about the average length of MTs<sup>145</sup>, preferential nucleation region<sup>60</sup>, subpopulations of MTs, relative orientations with each other and the organisation at the poles.

Nucleation of MTs, although preferentially happening at the centrosomes, is also observed at the chromosome mass region and from the KTs<sup>30,54</sup>. This phenomenon combined with the stabilization of the MTs around the chromosome<sup>146</sup> mass contributes to the geometrical integrity and assembly of the spindle.

The molecular motors, bundling, nucleating and depolymerising proteins also play a role in the spindle formation as detailed in the introduction (p21 §A-d). However, the method used

in this study does not allow us to identify these proteins within the structure, but solely the MT ends morphologies to deduce their polarity.

Overall, the relative crowdedness, the absence of reliable MT minus end markers<sup>19,60</sup> and the high dynamicity of the spindle in steady-state, also called dynamic instability, despite partial understanding of dynamic event, did not provide data on individual MTs within the spindle as well as the length distribution, the MT nucleation preferential location. Therefore, a more appropriate method would require an ET approach on the whole spindle and to identify and characterize individual MTs (orientation, length, origin and end, end morphology and relative localization in regard to the neighbouring MTs). In this chapter, I will elaborate on the method developed to address the previously mentioned questions, present some of the preliminary results obtained so far and the limitations of our approach.

#### **b. High Pressure Freezing of an in vitro system sensitive to pressure**

In the early stages of the project, we have carefully considered the cryofixation procedure and the correlative approach that followed. We already knew that other scientists tried to freeze the spindle in different ways and didn't succeed in retrieving them afterwards in the electron microscope. Following the advice from Kent McDonald<sup>95</sup>, Claude Antony and David Liebl successfully retrieved a centrosome accordingly to carbon landmarks in a plastic block. Taking inspiration for the freezing on the method mentioned by P. Hawes<sup>95</sup>, they trapped mitotic spindle in between two sapphire disks, separated by a gold spacer ring (p50 §B-b.ii.1.e) and loaded the assembly into the high pressure freezer HPM010 between two aluminium B carriers(in p51 §B-b.ii.1.g, replace the PDMS ring by B carrier, similar to the bottom one). However, those results were not reproducible.

We decided to test the assembly of the sample into the HPM010 holder. We used a sapphire disk assembly as described previously (p50 §B-b.ii.1.e), containing assembled spindles. We then mounted them into the HPM010 clamp with rigid spacers on top and bottom of the sapphire disk assembly as previously done. After re-opening of the clamp without freezing and recovery of the sapphire disk assembly, we imaged the same location according to the carbon landmarks. The spindle had in most cases changed location and/or disappeared (Figure 42), allowing only the DNA to be observed. By replacing the rigid spacer on top of the

assembly by an elastic ring (PDMS ring), we could prevent the disassembly of the spindle and the MT structure.

In addition, we observed (data not shown) that the spindles that were lying on top of the carbon were not easy to retrieve in the plastic bloc as they had in most cases turned or shifted. This observation leads us to focus our sectioning efforts on the spindles that were exclusively lying on regions free of carbon. We therefore developed an alternative carbon-coating method to reduce the surface covered by the carbon (p47 §B-b.ii.1.b.ii).

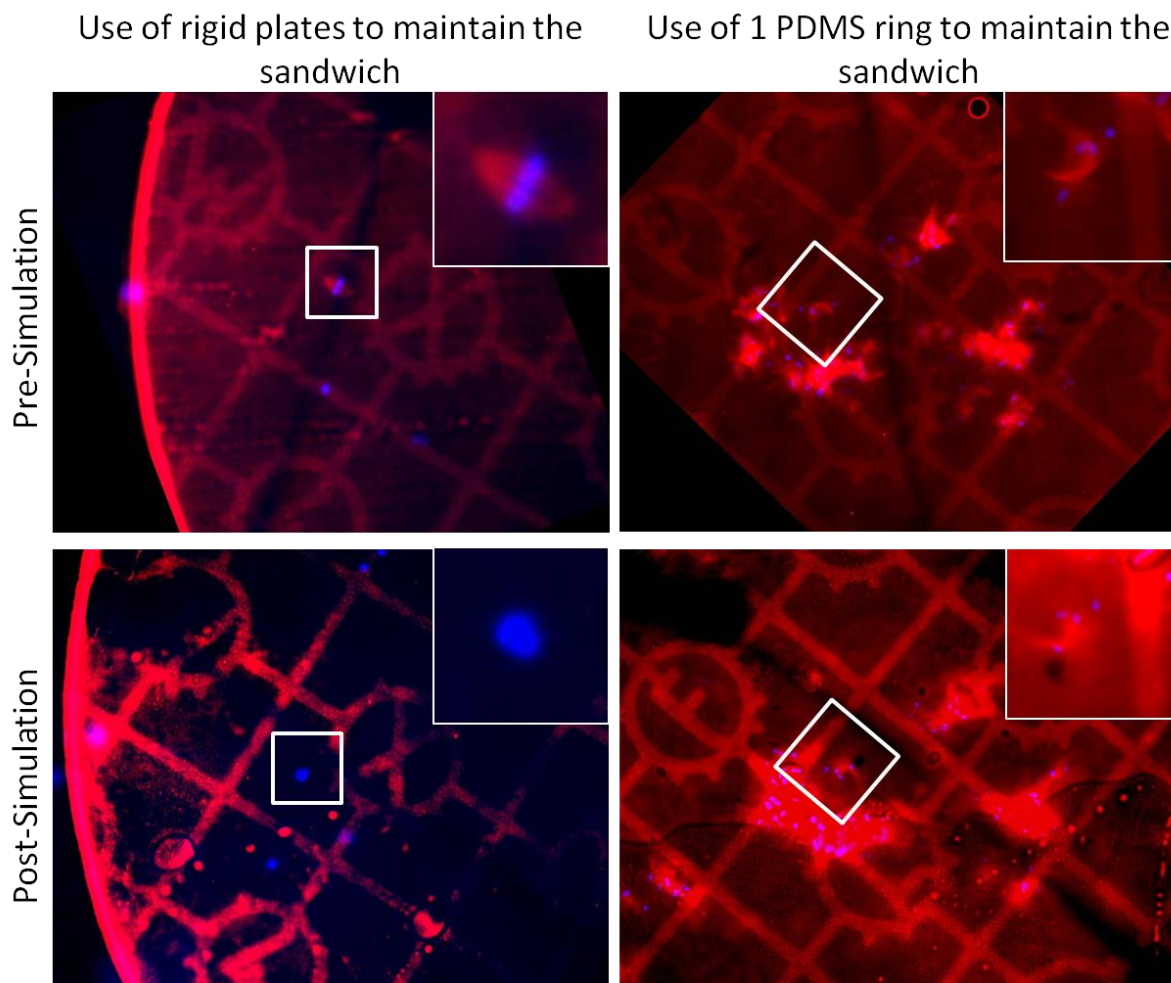


Figure 42 : Pressure Sensitivity: By simulating the freezing, we could test the impact of the positioning of the sample in the clamp onto the sample preservation.

To facilitate the sectioning steps, we took inspiration from a method presented at EMBL by Yannick Schwab <sup>70</sup>, drawing squares around the region potentially containing the spindle, using a laser etching dissecting microscope. However, in practice with our sample, this did not improve the trimming procedure and therefore we didn't continue along this line (data not shown).

Another important aspect of the trimming and sectioning steps lies in our incapacity to observe the spindles at any time by LM after the EPON resin embedding. We tried to image the embedded spindles by phase contrast (where the spindles are known to create a very strong interference), Nomarski contrast, fluorescence imaging by *a-posteriori* labelling the DNA using Hoechst on EPON block or on thin sections. The use of fluorescent spheroids was also attempted, but the vast majority of these probes are made of poly-styrene and dissolve rapidly in acetone (used along the whole FS procedure), making impossible to retrieve them. So the trimming was done blindly, relying exclusively on the carbon patterns.

### **c. Identification of the spindles**

Once the serial sections were collected, it became necessary to identify precisely the spindle within the 400 to 600 sections (typical number of serial sections acquired due to the blind sectioning). A first observation was the absence of mitochondria around the regions containing high density of MTs, independently of the presence of a real spindle. We took this first observation to orient ourselves into the plastic sections as no cell borders or macrostructures can be used for pre-mapping. A second but major observation was our ability to efficiently identify the chromosome masses within the sections. Their darker densities on large areas were easy to identify even at low magnification on the biotwin electron microscope (Figure 43).

Another important aspect to identify a good spindle is our ability to determine from the 2D images the orientation of the MTs. For technical reasons discussed later, we preferred to have the MTs oriented mainly parallel to the sections. The thick sections are normally an obstacle to identify the MTs without tomography. However, we could observe a few times that the MTs in the spindle are largely organized into large bundles of several MTs. This tight arrangement makes the MTs observable even in thick sections.

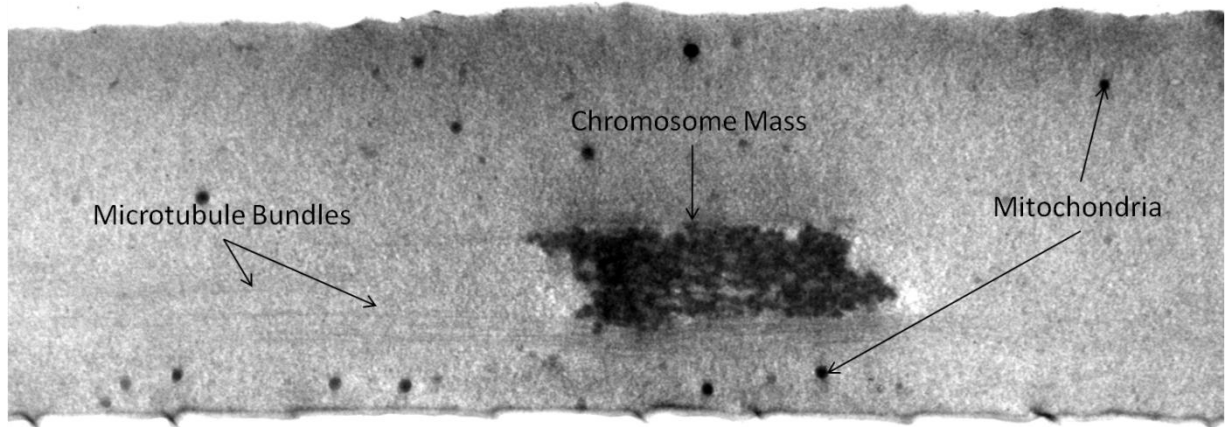


Figure 43 : Low magnification electron micrograph of a plastic section through a spindle. The denser chromosome mass in the centre was used as a reference for identifying the spindle structure. The horizontal fibrous structures around the chromosome mass are the MT bundles. The black dots are sparse mitochondria.

#### d. Selection of the acquisition parameters

In parallel to the development of the sample preparation and identification, we had to anticipate the acquisition parameters that would be required to successfully image, reconstruct and analyze the *X. laevis* spindle. As we refined our trimming/sectioning strategy, we produced serial sections through identified regions containing MTs and chromosome masses, on which we decided to test our acquisition parameters to preserve the spindles that we considered as being suitable for our work. During this preparation, we tested the post-staining and the thickness parameters extensively. We acquired single frame tomograms of sections ( $-60^{\circ}$   $+60^{\circ}$ ,  $1^{\circ}$  tilt increment, 12000x). Regarding the thickness, we quickly converged to the previous parameters used by the lab: the thickness of 300nm per section is the best compromise between resolution and sectioning efficiency (we tried 300, 350 and 400nm, combined with the post-staining parameters explained in the next paragraph).

However, the post-staining parameters proved to be very different from the previous studies<sup>55,102,147</sup>. We tried all the possible combinations of uranyl acetate (UA) and lead citrate (LC) contrasting time ranging from 0 to 20 minutes of UA (2% in Methanol or 0.5% in Methanol) crossed with the same contrasting times for LC (0,3,5,7,10,12,15,20 minutes of UA and LC, 2 different concentrations of UA, 3 different section thicknesses) and selectively acquired and reconstructed tomograms of the most promising staining results. All these parameter were tested on the same sample block to be comparable.

The presence of UA gave intensity gradient from the application surface towards the depth and added too much background without improving the contrast. This reduced our ability to identify the MTs located deeper in the section and to assign end morphologies (Figure 44).

The use of very long exposure to LC gave us a very clear and homogeneous contrasting of the MTs in all the 3 dimensions. We therefore established that the best conditions to contrast our sections were to use no UA and 12 minutes LC on 300nm thick sections.

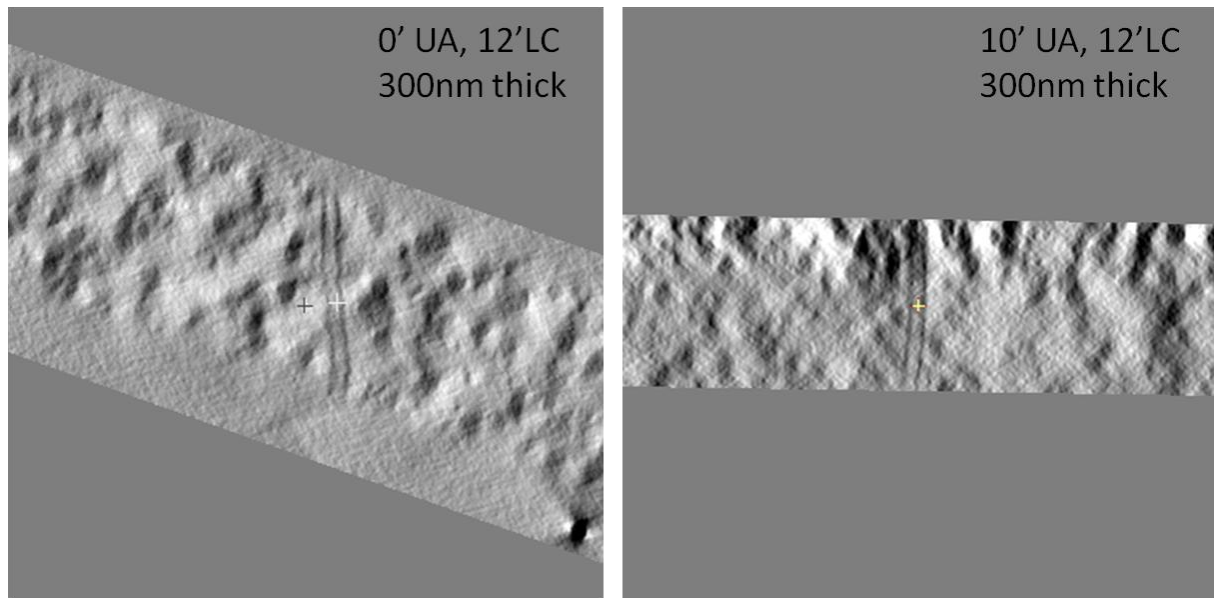


Figure 44 : Comparative images of post-staining parameters. The contrast is homogeneous when no UA is used for the post-staining of the plastic sections. When UA is used, the contrasting is gradually modified, reducing our ability to track individual MT.

To determine the microscope settings, we based our parameters on our ability to visually assess MT ends morphologies combined with the most time/volume dataset efficient acquisition parameters: at 12000x single frame single axis, we could identify the individual MTs and ends morphologies on our test samples (the sections were done on MT arrays around chromosome masses).

#### **e. Data acquisition of the midzone of a precisely identified spindle**

##### **i. The correlative microscopy proof of principle**

The sample we have been focusing on for the rest of this work gave us also the opportunity to unambiguously prove the principle of the efficient vitrification, using the PDMS ring on our sapphire disk assembly. The vicinity of two chromosome masses, totally isolated in the sample were extremely encouraging. Those chromosome masses correspond to two

spindles, somehow merged along two poles. In the LM, the distance between the centres of mass of the two chromosome masses was measured to be 26 micrometers ( $\mu\text{m}$ ). The distance from the main isolated pole (pointing towards the bottom in the figure) to the centre of the DNA was measured to be 21  $\mu\text{m}$ . The distance between the two main poles was measured to be 49.5  $\mu\text{m}$ . Finally, the width of the chromosome mass was measured to be 14  $\mu\text{m}$ .

On the electron micrograph, using a relative central section of the series (one out of approximately 45), the distance between the chromosome masses, was measured to be 27  $\mu\text{m}$ , the pole (in this sample, no centrosome could be located, but the MTs were still focusing towards a place that we named the pole) to chromosome was measured as 21  $\mu\text{m}$ , from "pole" to "pole" 49.5  $\mu\text{m}$ , and finally the chromosome mass height was measured as 11.5  $\mu\text{m}$ .

Here, the chromosome mass was measured in height as the sectioning axis (xz through y) is orthogonal to the wide field LM imaging (xy through z), giving us access to a width measurement (for a space orientation please refer to B-b.v.2.). Although we are measuring along two different axes, the relatively close values confirm all the previous ones. Moreover, the chromosome mass spans 45(+/-1) sections (hard to precisely determine due to heavy precipitation of LC on the last slot grid containing three sections). If the nominal sectioning value of 300 nanometre (nm) was correct over the 45 sections, we could therefore calculate a width (along the y axis) of 13.5 $\mu\text{m}$  (+/- 300 nm), confirming the LM measurement of 14  $\mu\text{m}$ .

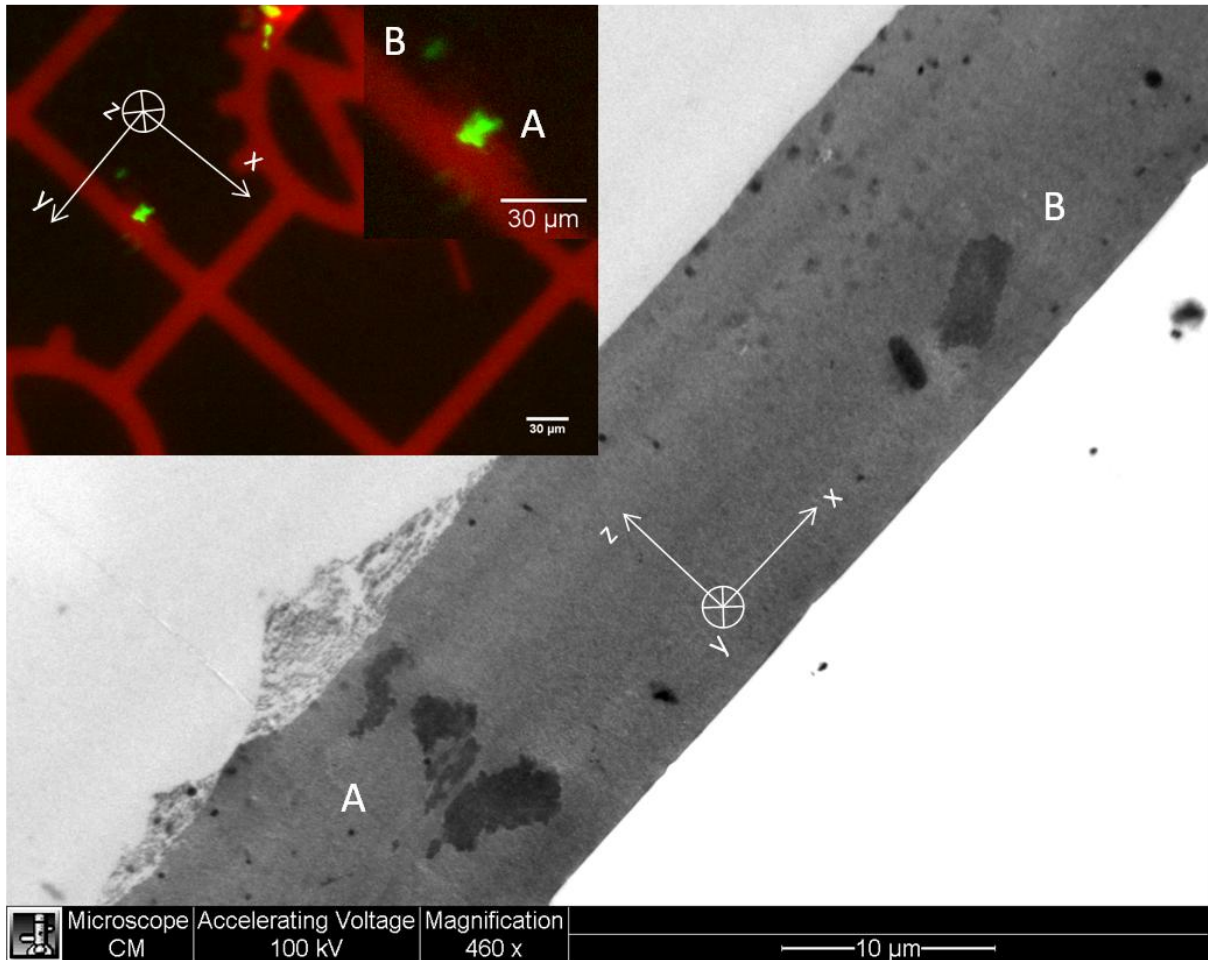


Figure 45 : The spindle identified by LM could be retrieved through the serial sections in the electron microscope. The orientation of observation though is rotated by 90° along the spindle axis (abscise).

## ii. Montaging and joining of the tomograms

With the accurate identification of this first spindle, we could proceed further, following the strategy commonly established with Claude Antony and Erin Tranfield. After acquiring the spindle midzone, reconstructing and joining it, many observations were made.

### 1. Radiation damage

The acquisition of montages is the only method available with the state of the art material available in EM for this large area project. The drawback of this method is the increase of the exposure of the sample to the electron beam. The electron beam is circular and is parameterized to cover the field of view of the camera during the whole tilt series. As we decided to keep the electron dose constant by condensing the electron beam along the tilt series, the initial C2 value (B-b.vi.1), corresponding to the width of the electron beam, was large enough so that at the end of the acquisition the condensed beam would still cover the collection field of the camera. As a consequence, some of the overlapping areas of

acquisition were exposed 2 to 4 times longer to the electron beam during the montage acquisition procedure, provoking a non-linear shrinkage of the section. Changing the exposure time instead of the C2 value to keep the electron count constant would also have resulted in non linear radiation damages. The tilting of the sample exposes more area with a comparable C2 area value (exposed area at 60° is:  $C2width/\cos60^\circ$ ).

Also, when we considered acquiring the complementary part of the spindle composing the pole (toward the opposite side of the chromosome mass B), we were not able to acquire new data, from the same data set, of equivalent quality. The parts that were not already exposed to the electron beam were extremely noisy and extracting information with a sufficient SNR proved to be impossible. A suggestion from Mikhail Eltsov was that the electron beam creates heavy contamination around itself, reducing therefore our ability to image the second part of the sample aiming for one spindle midzone plus one spindle pole. An example of this data alteration can be observed in Figure 46.

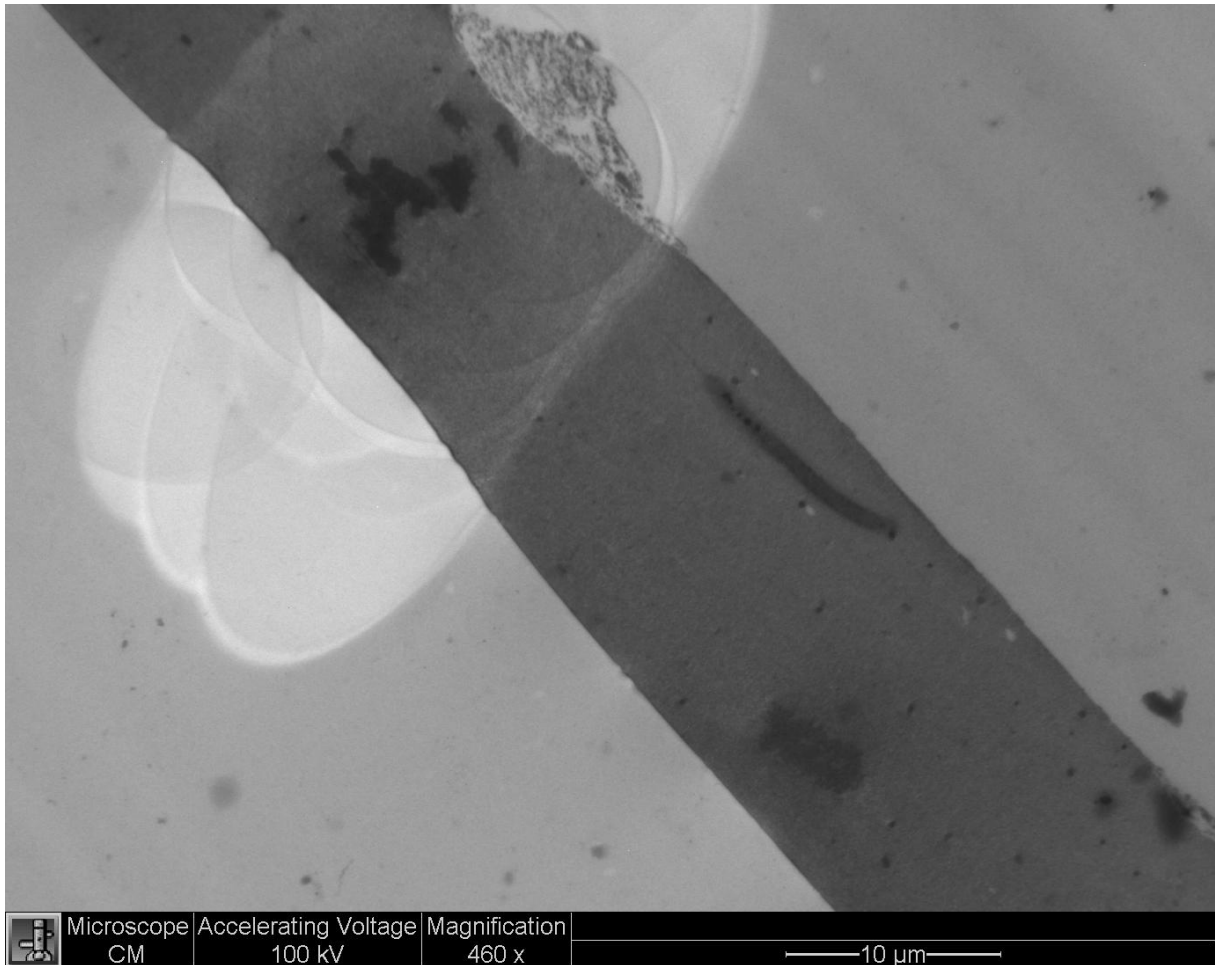


Figure 46 : After the acquisition of a 3x3 montage, the radiation damage of each row can be identified. The overall shrinkage of the section also becomes apparent.

## 2. *Non parallel microtubules*

If the vast majority of the MTs are organized into bundles, during the tracking of the MTs (manual, low resolution bundle tracking, semi-automatic and automatic) we could identify single isolated MTs that were not following directly the trend. Two types of non parallel MTs were identifiable: some were located directly inside the spindle (Figure 47a) and manual tracking would have been advisable to understand their organization. However, due to time constraints and the limitations of manual tracking, we could not model these MTs thoroughly. The second group of non parallel MTs was located at the periphery of the bundle (Figure 47b), mainly close to where the carbon coated sapphire disk was formally located. Those non parallel MTs could then be independent MTs lying on the sapphire disk, attached by PLL at the surface of the sapphire disk. Another potential interpretation would be the existence of pre-nucleated MTs progressively integrated in the spindle prior to their elongation<sup>36</sup>.

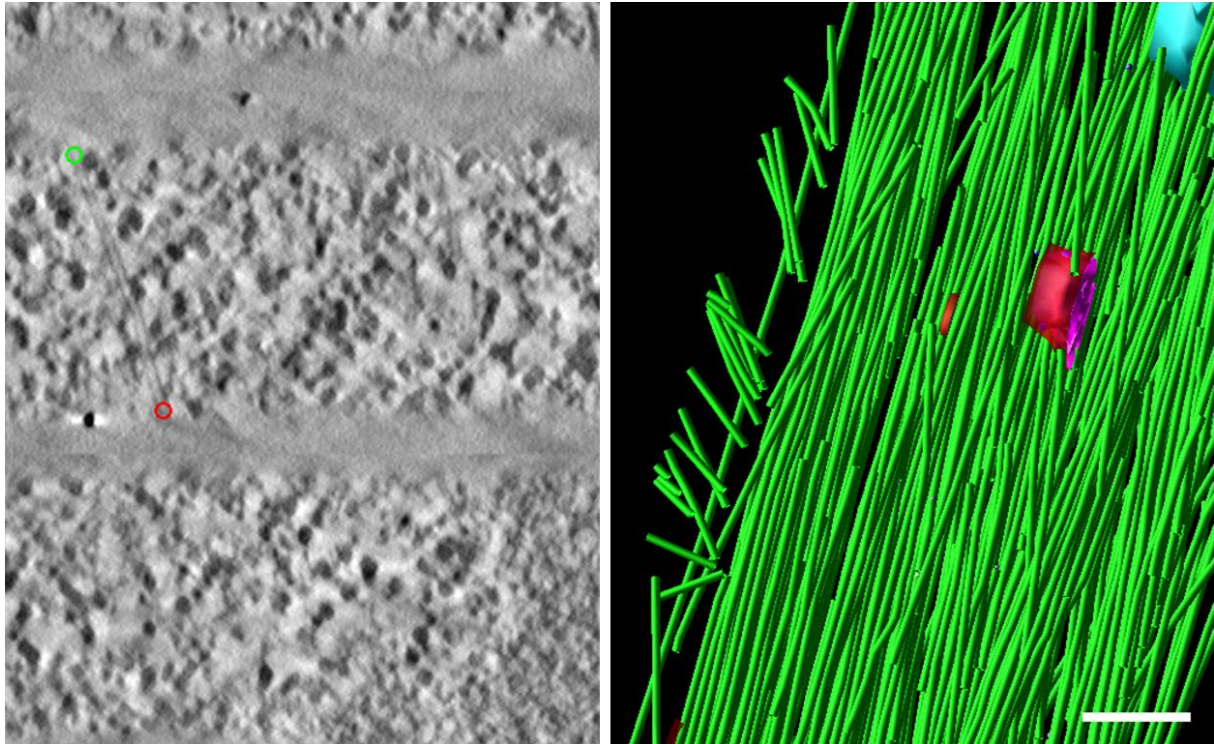


Figure 47 : A single MT orthogonal to the main MT axis. The horizontal gray lines represent the joining plane between 2 tomograms. The green and red circles were landmarks used to get the corresponding MTs within the previous and the following sections. The left panel is a model view where several MTs are oriented orthogonally to the majority of the MTs. The red and pink mass are mitochondria; the blue mass at the top is part of the chromosome mass.

### 3. *One single chromosome mass*

After the pre-mapping done at low magnification on the biotwin electron microscope, the chromosome mass seemed to be one single mass and it was not possible to distinguish the chromosomes from one another. The finer analysis done on the join tomogram confirmed this first observation. The 36 chromosomes seem to blend into each other and are not clearly identifiable. Therefore we keep the term “chromosome mass”, corresponding more precisely to the actual physiology. The calculation of the chromosome mass surface cannot be done realistically with our modeling method. Only the calculation of the volume would be appropriate.

The total volume was calculated from the outlines of the chromosome mass using FIJI and represents  $356,4\mu\text{m}^3$  out of the theoretical  $2650,7\mu\text{m}^3$  of the full spindle (Double cone,  $h=22,5\mu\text{m}$ ,  $r=7,5\mu\text{m}$ ). However, the sample do not cover the whole chromosome mass. Knowing we acquired 32 sections out of 45, and that the theoretical shape of the spindle is a double cone, the potential full volume of the chromosome mass shall be  $501\mu\text{m}^3$ .

#### 4. Bundles

Looking closely at the tomograms individually and in the join region, a striking observation was the existence of bundles with tightly packed MTs. These large bundles go through the chromosome mass, interconnecting with each other in a complex manner. Those bundles have various morphologies. When located outside of the chromosome masses, they were rather straight as described most often in the literature<sup>36,141</sup>. However, while going through the chromosome mass, they were strongly bent and deformed. The observed deformation is restricted to the chromosome area and happens in all directions, even within each independent tomogram, suggesting that these deformations are not the consequence of a sectioning artefact. Sectioning artefacts are generally crevasses and knife marks and therefore generally linear.

Freezing artefacts when they occur create damage at the protein level and result in protein segregation, where the water content separates from the proteins.

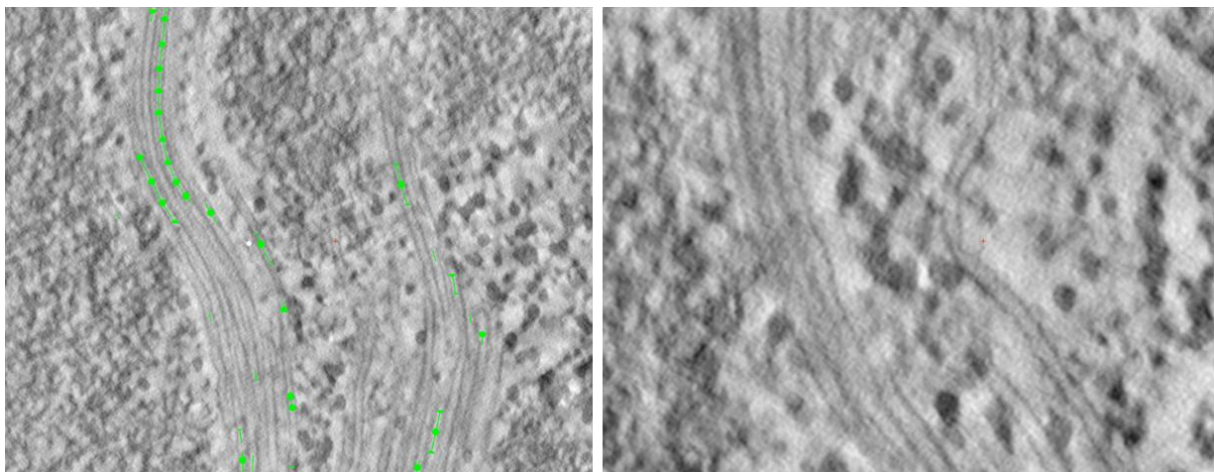
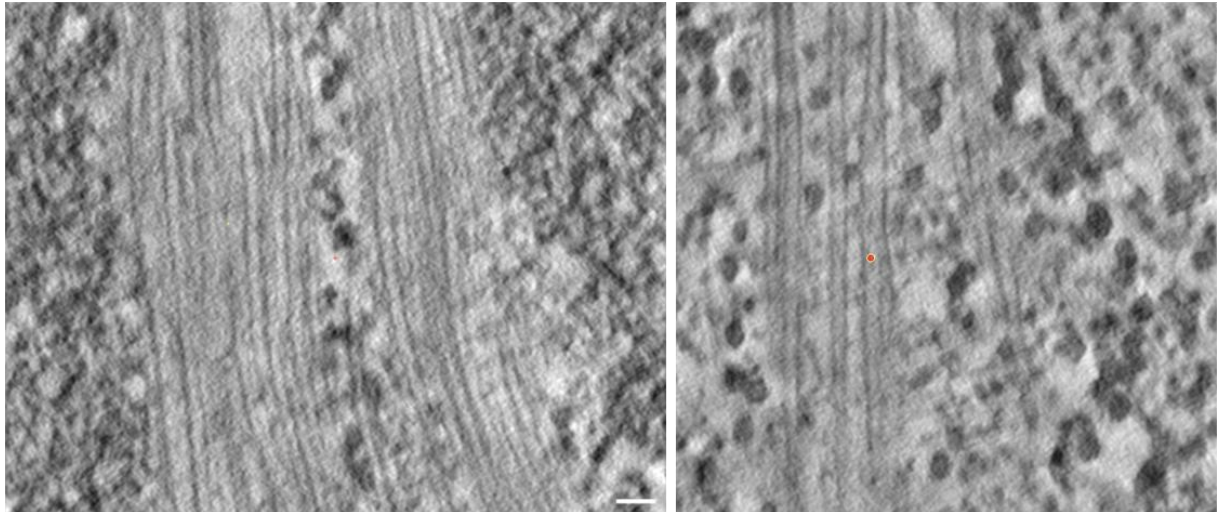


Figure 48 : MT deformations within the chromosome mass, in and out of large bundles.

To approach and understand the organization of these bundles we took two approaches. The first one consisted of manually modeling every individual MT within the join. To do so, we opened sub-regions of the join, spanning a whole individual tomogram and manually traced the MTs using the slicer. Accurate tracking was impossible: the tight proximity of the MTs within the bundles, combined with the missing wedge and the pixel size of 2 nm were a limiting factor that could not be overcome at the time of this work.



**Figure 49 : The MTs are tightly bound within the bundles. This results in ambiguous identification of the individual MTs during the tracking.**

However, to get an impression of the overall organization of the MTs, we manually tracked the MTs in 3 consecutive sections with Erin Tranfield and Willis Pinaud (summer trainee). This way we obtained a good appreciation of the organization trend. As initially observed, the bundles are going through the spindle and do not stop at a central position. Some MTs are leaving one bundle to reach another and some independently stop in the chromosome mass.

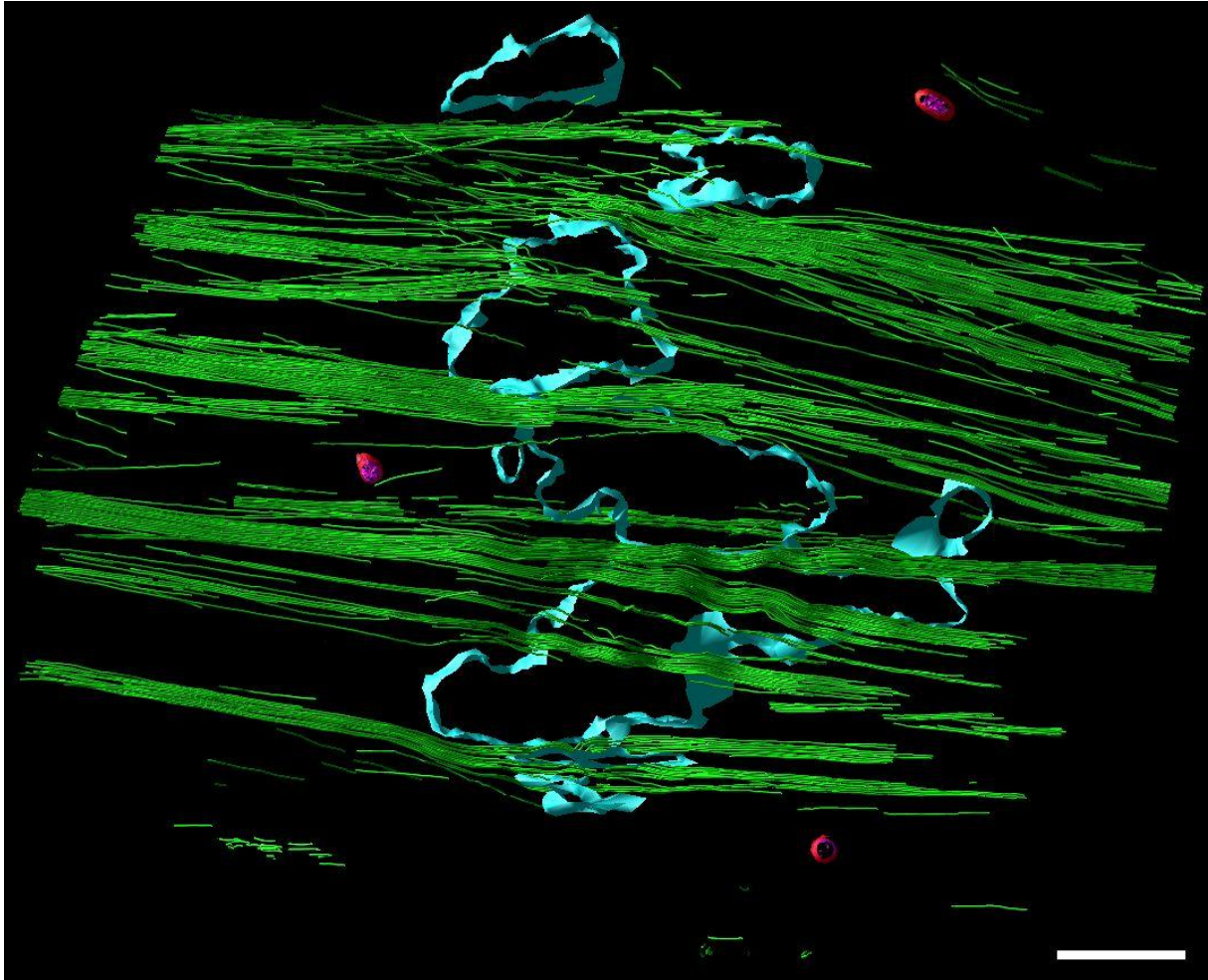


Figure 50 : Overview of the manually tracked model through 3 consecutive tomograms of the join.

The final join, 32 montage tomograms, is a too large volume to realistically manually track all the MTs it contains. However it represents a valuable initial dataset to understand the organization of the spindle on a large scale. Considering the challenges that the individual MT tracking represents, it might be fruitful to establish an initial very low resolution model of the whole structure. This is also a way to ensure before starting the detailed analysis that the selected spindle corresponds to a physiologically proper spindle (**Erreur ! Source du envoi introuvable.**).

### 5. *Microtubule / chromosomes interactions*

One of the key targets of this work was to identify the kMTs. The literature describes the KT as a dense plaque where MTs meet, originating from the two poles<sup>141</sup>. During the low resolution tracking of the MT bundles and of the chromosome mass, no such structure could be identified.

## 6. *Microtubules ends in the spindle*

During the manual tracking, we could sometime observe clear MT ends and identify their morphology. As most of the MTs are in bundles, it was not surprising to observe ends within the bundles. Here we present a gallery of ends, although no measurement about their localization and proportions has yet been carried out.

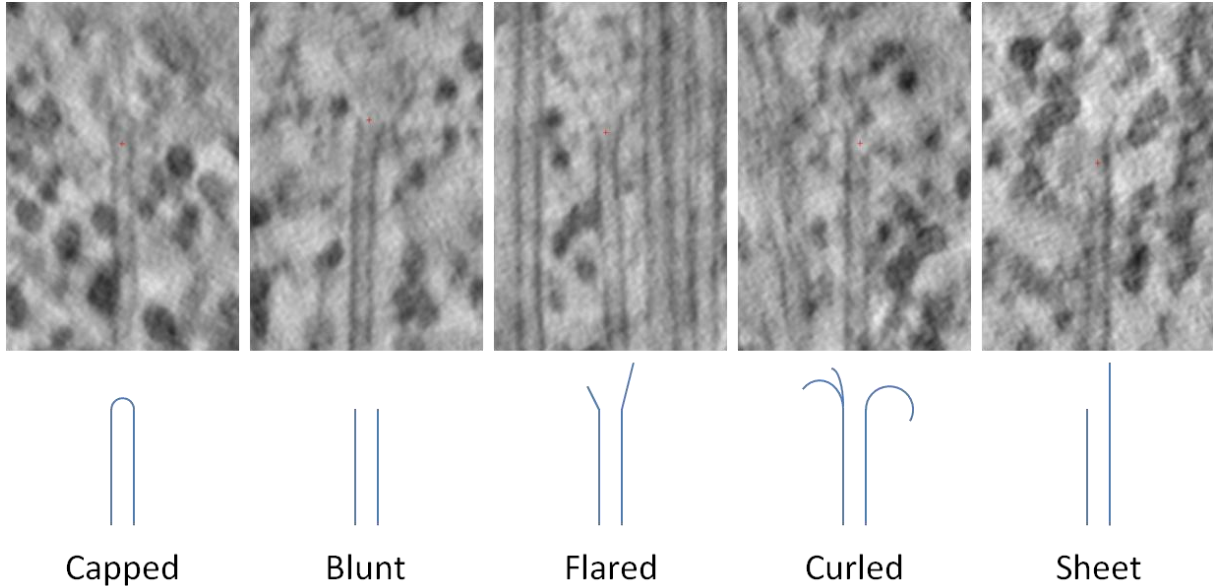


Figure 51 : The five types of MT ends can be observed in the spindle. The low SNR reduces our ability to identify precisely all the MTs end morphologies.

## 7. *Modeling of the whole midzone*

As previously introduced, a low resolution model of the join was produced following the procedure described in the material and methods. The MTs are running along the chromosome mass with lateral connections, going tightly associated through it.

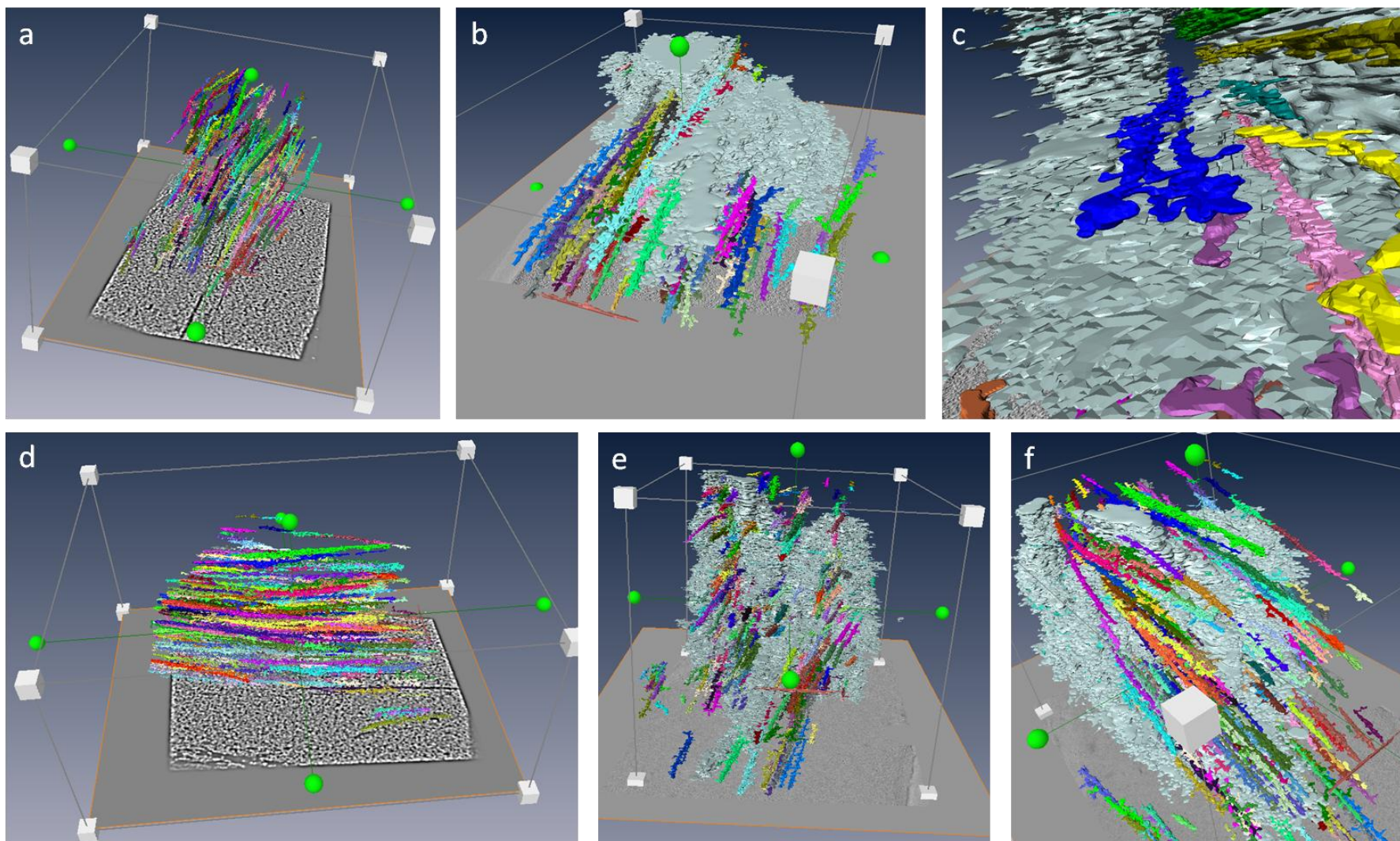
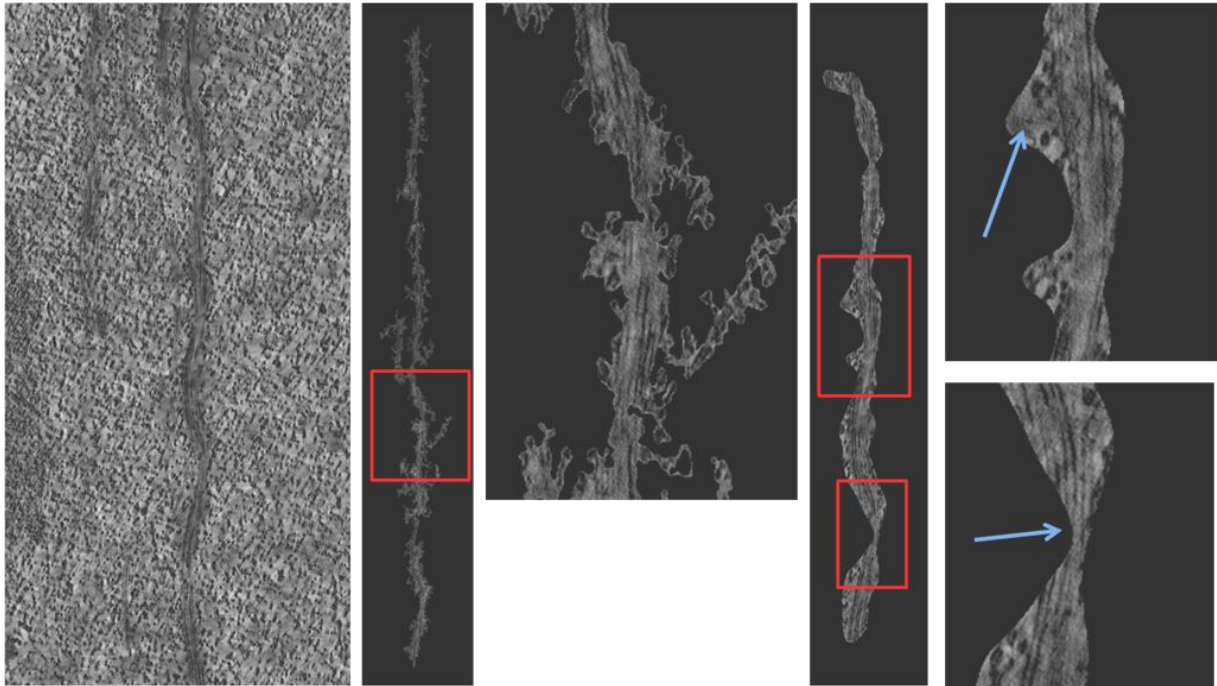


Figure 52 : Model overview of the midzone: the MT bundles are organised in parallel and focussing towards the poles is not yet distinguishable (a,d). The MT bundles are running around and through the chromosome mass (b,c,f). The chromosome mass appears in grey-blue. At the bottom of every model is an electronic slice of the tomogram. In a and d, the electronic slices are the filtered for the bundles (BundleStack). b,c,e,f are presented with the OriginalStack electronic slice at the bottom.

This overview is a good estimate of the organization of the MTs into bundles in the midzone area, and permits the identification of isolated bundles as described with more details in D-e.ii.8.



**Figure 53 :** The segmentation used presents some limitations for quantitative measurements and shall only be used for qualitative observation.

The parameter used for this quick manual segmentation presents however limitations when trying to get a quantitative measurement. First, the individual MTs are systematically eliminated from the detection as the filtering used focuses on large areas with a low variance. Typically, the centre of the MTs in cryo-substituted material is homogeneous, as opposed to MTs observed in cryosections<sup>130</sup>. The combination with the regular walls of the MTs plus their regular spacing helps the detection with the Fourier filter transform (FFT, bandpass filter). As observed previously, the larger the bundle gets, the higher the homogeneity is, while still keeping the parallel lines detected by the FFT. This combination of successive filters is efficient to segment quickly the bundles with more than 3 parallel MTs per plane.

Some limitations of this filtering can be observed in the Figure 53: a zone deprived of ribosomes nearby large bundles will be included into the variance filtering and will not be excluded by the bandpass filter, resulting in including MT free regions into the segmentation

mask of the bundle. Similarly, when MTs are too narrow or too close to each other, the variance filtering width excludes the MTs and those are not rescued by the bandpass filter. These two limitations are not significant for a qualitative observation, as they compensate each other along the 3 dimensions. However using this mask to characterize the bundles quantitatively might not be advisable.

### *8. Morphology of the bundles*

Quantitative measurements of the bundles might be misleading, due to the limitations of the model mentioned above. But three distinct qualitative features were easily identified during the modeling. The first class corresponds to very tight and large bundles, composed of more than thirty MTs. They are large, wavy near the chromosome mass and are independent from the surrounding bundles in the imaged region (Figure 54).

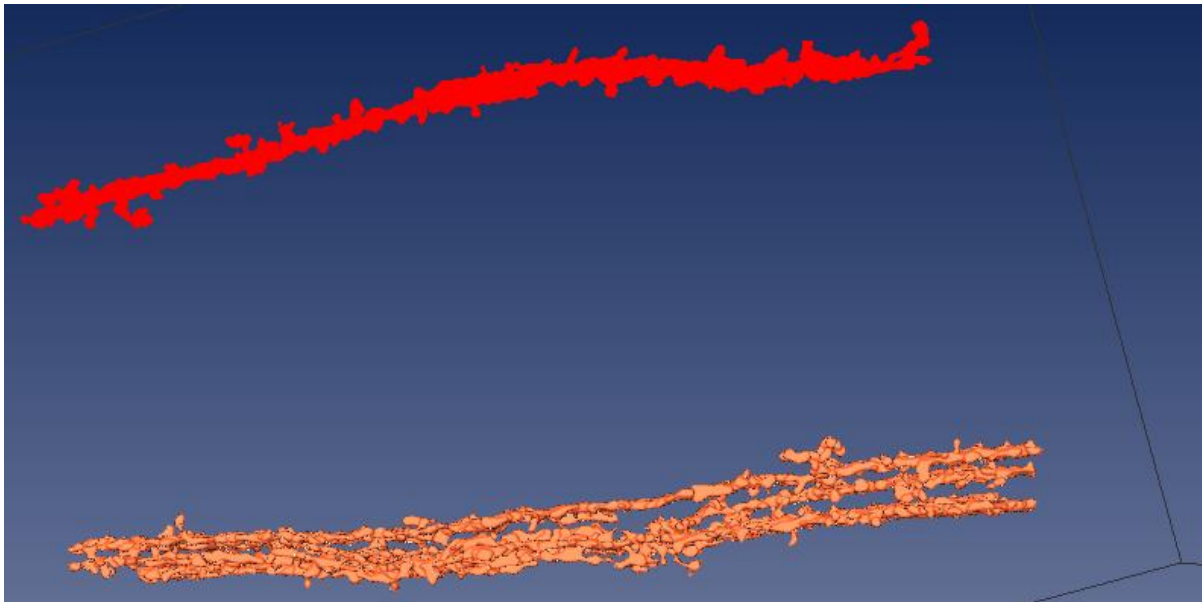


Figure 54 : In red, a large bundle composed of more than thirty MTs is going through the whole volume without interacting with other bundles. In orange, the second class of bundle can be seen, where several medium bundles are connected to each other in different locations.

The second class is more heterogeneous and is composed of middle size bundles, containing ten to twenty MTs. They are closer to each other and are connected by the third class of bundles. The third class is essentially composed of less than five MTs and is usually branching from one medium size bundle to another. This second and third class are connected to each other and do not interact directly with the first class. Due to our segmentation strategy, the third class wasn't properly segmented and could be observed on the raw images but not on the filtered images.

In the current model, 25 bundles could be classified by eye in the first class; the second and third class could not be quantified individually and were grouped. 68 bundles of the second and third classes were then counted.

#### **f. Acquisition of the full spindle**

##### **i. Super montaging at low magnification**

Anticipating the challenges that the acquisition of the whole spindle represents, an alternative solution might be considered. Instead of acquiring the whole spindle at very high resolution, an initial low magnification imaging could be done and modelled in a reasonable amount of time. A systematic acquisition of the full volume completed with further modeling would be done, while later on high resolution regions of interest, that were primarily identified and located within the spindle, would be acquired.

The strategy relies on adopting a magnification of 4700x, with a binning of 2. The resulting pixel size would therefore be 4.97nm. The MTs would then be covered with 5 pixels (25nm in diameter) but the bundles would be larger with a characteristic signature in the Fourier space, facilitating their detection.

We validated this strategy by acquiring one super-montage at 4700x of 3 times 2x2 montages, reconstructing the whole tomogram and applying the image filtering as previously described.

#### ***1. Results and Model***

The limited number of sample available for our test forced us to acquire our low magnification dataset on the previously imaged sample. Two consecutive super montages were acquired at 4700x, reconstructed, flattened independently, super montaged, and then joined.

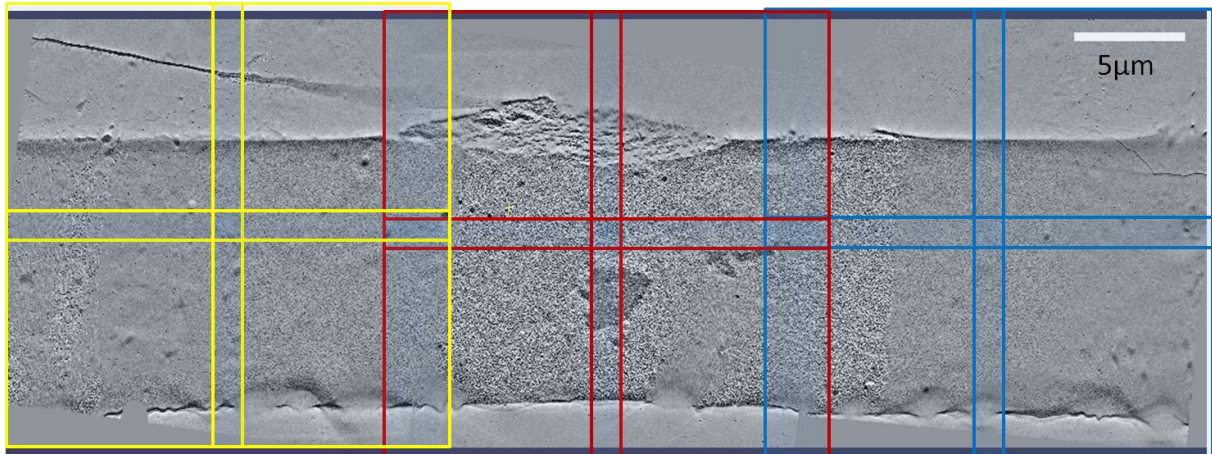


Figure 55 : Electronic slice through the super montage acquired at 4700x with a schematic representation of the overlapping 3x2 montages.

The contamination of the regions surrounding the midzone (D-e.ii.1) were an obstacle to proceed with the fast segmentation as a dramatic SNR decrease occurs. Therefore, the segmentation of the chromosome mass and the bundles was proceeded only on the non contaminated region (red montage), despite our acquisition of the whole region.

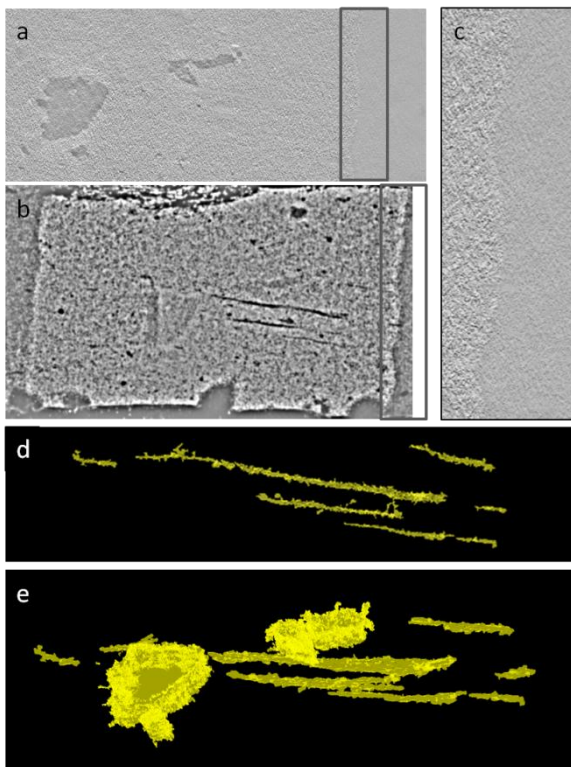


Figure 56 : From the low magnification supermontage (a), contamination artefact can be observed (c): The squared region (a) magnified (c) illustrates the decrease of SNR between the pre-acquired region, (non-contaminated) and the contaminated region. After filtering, the MT bundles appear denser (b) and more structured than the other regions. The region with a good SNR was segmented in two steps: first the chromosome mass was segmented from the non filtered dataset (a) and then, the bundles were segmented (d) from the filtered images (b). The two models were then combined to give a 3D overview of the dataset (e).

The appropriate method to pursue the low magnification rapid segmentation would consist of acquiring the whole spindle, from pole to pole using supermontages along all the collected serial sections. A rapid reconstruction, supermontaging and joining would allow for generation of a Z-stack, every 4 sections (5nm/pix) to ensure the proper capture of every MTs within each bundle, but reducing the data volume to process by a factor of 4. These sections will then be processed as already described by batch processing. The different Z-stacks generated will then be used to adequately model the chromosome mass and then the MT bundles (Figure 56).

From this low resolution model, the general geometry of the spindle would be assessed to ensure that the material is suitable for a high resolution acquisition and quantification. Regions of interest: poles, bundles, midzone will then be accurately located on the sections and acquired.

This two step approach will allow us to select our structure of interest in a reasonable amount of time prior to a more advanced time consuming high resolution approach.

#### **g. Summary of the biological outcomes and interpretation/discussion**

The *X. laevis* spindle has been extensively studied over the past decades by scientists to address biochemical, structural and functional questions about the spindle dynamics and its assembly<sup>36,60,91</sup>. The unique opportunity for scientists to assemble a mitotic spindle *in vitro* and to cycle it (semi-*in vitro* egg extract system) has been a major achievement to study specific events of the cell cycle of a vertebrate<sup>91,92</sup>. The ability to create mitosis in an open system has allowed the community to carry out protein depletion, down-regulation, over expression and mutation to specifically perturb the system and investigate protein function in the spindle assembly process<sup>135</sup>. The *in vitro* system has been extensively used by the community to broaden our knowledge on mitosis, but important structural information at EM resolution is still missing<sup>8,60</sup>. The organization of the spindle at single MT resolution remains unclear<sup>19,60</sup>. The method of choice to date to image precisely individual MTs within a biological system is ET<sup>55,148</sup>. Until recently, the computing capacity did not enable scientists to handle datasets in a range superior to a couple of gigabytes<sup>101,102,148</sup>. The recent advances in informatics and in image processing are now giving us a first opportunity not only to produce high resolution large datasets, but also to handle and analyze them.

If the specific dimensions of the *X. laevis* spindle (45µm x 20µm x 20 µm) are facilitating image analysis at the LM level, they are a major challenge for ET where a pixel size of 2nm or lower is commonly used to identify independent MTs and their end morphologies<sup>55,96,102</sup>. Not only has the computing capacity been a limit to study this model organism by ET, but the optimal sample preservation required for this type of study was also challenging. Previous electron microscopic studies on the *X. laevis* spindle were made using chemical fixation<sup>5,141,149</sup>. Optimal methods to preserve biological specimens are cryo-fixation methods, and the only method to date to cryo-immobilize structures with the dimensions cited above is the HPF. We therefore used it as a base for the whole study.

Rapidly, we realized that the meiotic spindle structure, after FS, could not be observed in the plastic embedding resin (EPON) by LM. Our attempts with bright field, interference and fluorescence light imaging were not successful and lead us to develop a correlative light to electron microscopic method where we could use other markers than the biological sample to retrieve our structure of interest. Inspired from previous works<sup>129,150</sup> we used the evaporation of a carbon film through finder masks combined with PLL coating to enable us to localise the spindles on the sapphire disk substrate prior to HPF. Our serial sectioning method following the carbon finder mask proved unsuccessful as we did not manage to retrieve reliably the high-pressure-frozen spindles. The reason for that lays in the preliminary steps of the HPF. The pressure upon locking one sample in the HPF clamp imposed a deleterious stress onto the biological material between the fluorescent imaging and the HPF. The HPF clamp applied a heterogeneous pressure leading to the disassembly of the spindles. We opted for the use of a PDMS polymer ring on one side of the sapphire disk chamber that could maintain it without applying a deleterious pressure leading to the disassembly and relocation of the biological specimen within the sapphire disk assembly. A suggested solution was to accurately measure all the parts used for each individual freezing and therefore accurately select the optimal elements that would fit perfectly inside the clamp, in order to avoid the deleterious pressure. Therefore the use of an elastic layer, which could compensate for the variation in the elements size greatly facilitated our work and finally gave convincing results. To improve the reproducibility of this technique, we created sheets of PDMS polymer with various thicknesses. The selection of the appropriate PDMS ring was done by eye prior to the freezing, relying on its elasticity to compensate the right height. This

low precision of the total thickness of the sapphire assembly (sapphire disk chamber, B carrier and PDMS ring) and the poor alignment inside the clamp resulted in a success rate of approximately 50% sapphire disk assembly not breaking during the freezing process.

The samples were then taken through FS processing and the sapphire disk chambers were opened just prior to the flat embedding. Taking advantage of the cylindrical shape of the spindle, we chose a flat embedding approach. Precise rotation of the EPON flat embedded block in the microtome allowed us to systematically serial section the spindle along its longitudinal axis. Progressive trimming of the flat sample allowed us to reach the spindle one by one on every flat block, improving therefore the number of potentially good spindle per flat block. On block sectioning would have limited us to one or two sample per sapphire disk chamber, forcing us to proceed with a re-embedding of every sub-block and reducing our orientation ability.

We also considered the sectioning orientation carefully. Two major solutions were considered. Either sectioning with the MT orthogonal to the sectioning axis, meaning from one pole through the spindle until the second pole. This approach would have required collecting 150 serial 300nm thick sections. The advantage could have been the tracking of the MTs cross sections using a simple template matching of a circle. However, the orientation of the MTs along the missing wedge would have prevented us from recognising the ends morphologies. Also the joining of 150 sections might have been a limiting step considering the poor amount of cross correlating factors between the sections. The second solution that we decided to adopt was the sectioning along the pole-to-pole axis, with the MTs organized longitudinally in the sections (data used). This approach required 50 serial sections to collect the whole spindle. The MT morphologies are then discernable as they are in the optimal orientation regarding the missing wedge. Also the manual tracking is optimal in this longitudinal orientation.

Our difficulty to obtain serial sections of well preserved sample lead us to establish all our test phases on well vitrified biological material like asters or spindle aggregates but not on individual spindles. The selected parameters that we considered optimal to distinguish the individual MTs and their end morphologies later proved to be inadequate for the bundles we observed in the actual spindles. The tracking of individual MTs within bundles poses

problems to track individual MTs within the bundles and the image acquisition parameters need to be precisely defined to successfully track every single MT. Moreover, the number of individual MTs requires computational methods that can automatically track individual MTs throughout the tomograms. Our collaboration with a laboratory specialised in image processing programs, Zuse Institute Berlin Amira (ZIB Amira, Berlin, Britta Weber and Steffen Prohaska) is meant to use their MT automatic tracking program for our project and help them to improve their program by providing them useful feedback and samples. One striking result obtained so far is that the most efficient parameters for the automatic tracking do not correspond with the best parameters for manual tracking. The finest pixel size is required to accurately track most of the MTs within each bundle as a larger pixel size is more adequate to human eyes. Those results not shown in this thesis are however important parameters to take into account for the following paragraphs of this discussion.

The dimensions of the spindle combined with the required acquisition parameters imply having to deal with a new level of data volume. If the storage is not a limiting factor, our ability to process the data needs to be carefully anticipated. First of all, the acquisition time: acquiring the full spindle with the pixel size needed for the automatic tracking (1nm/pix) requires working at high magnification or without binning the camera. The binning of the camera is strongly recommended with the Eagle camera (FEI) as the sensitivity of the detector is inferior to half of the Nyquist frequency, resulting in a very low SNR on the single tilt images used to the later reconstruction. A low SNR reduces the contrast and the alignment accuracy using the patch tracking method. To reach the adequate pixel size, a magnification close to 20.000x is needed. To cover then the full spindle width, a 5x5 montage is required. The electron beam shall then be tilted on a long range and the microscope aperture shall be accordingly selected. Larger aperture reduces the contrast and results into a lower SNR. Alternatively, to keep small apertures for high contrast, we need to acquire a 2x2 super-montage of individual 3x3 montages, which is equivalent to a 6x6 montage. To cover the whole spindle length (45 $\mu$ m), 4 to 5 of these super-montages will be necessary. This shall be acquired over the 50 to 60 serial sections. The acquisition time of one single 3x3 montage takes 4 to 5 hours and generates an 8 gigabytes (Gb) tomogram. The acquisition strategy at 20.000x would then mathematically require at least 4000 hours of acquisition and generate 8 Tb of raw data.

A similar approach using no binning at 12.000x would need 3 to 4 super-montages in length, each 2x2 super-montage being composed of 2x2 montages. The acquisition time per single 2x2 montage unbinned is approximately 6 hours and 15 Gb per reconstructed tomogram. This would then require at least 4800 hours of acquisition and generate 12Tb of data.

As an alternative, a more selective approach can be taken and was tested in this work. Acquiring the whole spindle at low magnification (5nm/pixel), could enable to acquire the spindle volume with a 3 to 4x1 supermontage of 2x2 montages. Using a binned camera, each 2x2 montage is acquired in 3 hours and generates a 2.5 Gb tomogram. Acquiring the whole spindle would then take 600 hours and generate 500 Gb of data. From the full volume, a quick segmentation of the MT bundles and the chromosome mass can be generated to identify regions of interest. A precise location of these regions can be then retrieved on the sections and a detailed acquisition can be done at higher magnification with the desired pixel size. This approach is less time consuming but cannot give the same exhaustive answers as the higher resolution. This two step approach is therefore important to consider prior to acquire the full spindle at high resolution. Furthermore a potential drawback is the contamination of the section around the acquired area as shown in D-e.ii.1 (p102) and D-f.i.1(p113). The contamination has not occurred in every case of acquisition, but it would impair the two step acquisition strategy.

Based on our initially established parameters (D-d), we acquired the midzone of the spindle with a pixel size of 2nm at 12.000x. We reconstructed three quarter of a spindle midzone by acquiring montage tomograms along 32 serial sections. A first general observation of the volume revealed significant information to us. Firstly, the spindle region dramatically lacks mitochondria compared to the surrounding regions. Still this exclusion zone is not total and sparse mitochondria can be seen. So considering the energy required maintaining a structure as dynamic and large as a mitotic spindle, the dramatic separation appeared striking. In our first steps in this project, we used the absence of mitochondria as a sign of the presence of MTs. Secondly, the chromosome mass, centre of gravity of the spindle, appeared much denser compared to the surrounding regions. This was used later to accurately localise the spindles we were aiming for. Third, the chromosome mass looked like one single mass, where chromosomes were not distinguishable. This was confirmed by the rapid segmentation done with FIJI. All the chromosomes at the stage of HPF were compacted into

one single mass, confirming our light microscopic observations. We could not use individual chromosomes to reduce our field of investigation (identification of KTs, for example). The last observation done without detailed modeling concerned the MTs themselves. They were generally tightly bound into bundles but a minority was acting as connectors between the MT bundles or totally independent from the bundles at the periphery of the spindle. Moreover, the very strong bending of the bundles within the chromosome mass was a surprise for us. The good preservation of the fine structures without protein segregation and the high quality of contrast obtained were a sign of good sample vitrification and FS. A closer observation revealed that the bending was happening only within the chromosome mass or at the very close periphery; no such strong bending could be observed in the rest of the structure. Moreover, no trend for the bending could be observed that would lead to the deformation of the structure: no knife marks or compression, no torque of the EPON block or the sample. This specific localization of the deformation lead us to conclude that indeed the chromosome mass most likely exert a force onto the MT bundles that has not been described before. The absence of a wider overview of the entire spindle prevents us from any further conclusions.

To further analyse the structure, the modeling was done in two steps. The low resolution modeling of the whole structure, including the chromosome mass and the bundles, was adopted to get an overview. The bundles are generally organized into three different categories. The first one is composed of large bundles, containing more than twenty MTs. These bundles in the volume are independent and structured as unique independent masses. The second category, composed of five to twenty MTs is not so dense and is usually networking. The cross-bridging with other bundles of the same second class is made by the third class of bundles, composed of less than five MTs. The proportion of the first two classes is equivalent, as the third class is harder to quantify due to its connecting nature. However, these observations are limited to one single reconstructed spindle so far and to the spindle midzone. We cannot exclude that these bundles are connected and interact strongly in the farther ends of the spindle, towards the poles. Furthermore, we have used PLL during the sample preparation and Dan Needleman raised the point that PLL may cause MTs to bundle. This later suggestion led us to remove the PLL from the sapphire disks to compare our results and observations. Currently, Erin Tranfield is doing experiments to assess the actual

bundling effect on the MT bundles. The first results showed that high concentration of PLL in solution collapses spindles while low concentrations do not show clear effects. Intermediate states will be tested in the near future to determine whether there is a progressive effect or if it is a critical concentration that causes spindles to collapse.

Also, we have traced manually the MTs through three tomograms in the centre of the join. Each individual tomogram was modelled by a separate user. The number of MTs traced was comparable in each tomogram, but our ability to trace individual MT within the bundles proved to be challenging and inaccurate tracking happened regularly. Typically, while tracing a MT, an overlap could be observed with a MT already traced, as if one MT had divided into two MTs. Taking a closer look at the two MTs that seemed to blend into each other, it was generally hard to decide which MT should be favoured to continue the tracking. As already mentioned the PLL used might cause a densification of the existing bundles, so removing it from the initial experimental parameters might reduce the clustering and therefore facilitate the tracking of individual MTs. Furthermore, the improvement of the programs developed to automatically track the MT bundles should improve the accuracy of the tracking.

From the different models generated throughout this PhD work, we aimed at identifying sub-categories of MTs. One important question was regarding the kMTs-MTs, supposedly reaching distinct regions of the chromosome mass. This population represents 5% of the total MT population<sup>36</sup>. We expected to observe a clear ending of several MTs upon a globular denser chromosome region as described in the literature (Figure 6,<sup>36</sup>). However we could not identify such regions upon the modeling process. Considering that we covered 75% of the mitotic midzone in the volume presented in this work, it is unlikely that no kMT-MT was located within the observed area. To understand why we could not observe any kMT-MT, several aspects shall be considered. First of all, our sample preparation is dramatically different from the previous studies by the novel fixation used. The vitrification of native sample followed by the gentle process of FS does not extract the sample. The ribosomes are preserved as all the protein material. A faint density variation becomes therefore less obvious. Second, tomography was attempted for the very first time on this biological specimen and interpretation of 3D data has to be carefully made. Previous EM work was done using thin sectioning of chemically fixed specimen. The projection of such fine structures through 70nm (thin sections) can result in projecting intensity that could not

be observed by tomography. In order to understand more precisely what we are given to see, more tomography work will be required to generate a library of reference micrographs. They will facilitate our understanding and interpretation of the whole spindle structure. Third and most important point, the acquired volume is not optimal and the resolution needs to be improved. By precisely modeling individual MTs, the identification of specific MT by end morphology and distance towards the chromosome mass should help us identifying the desired MTs.

Another population of MTs, the structural MT represent most probably the large majority of MTs within the spindle. They organise into bundles of various structures, emanate from the MTOCs and overlap at the spindle midzone. The three categories of structures observed by the rough modeling suggest that all bundles are not equal and might have different functions within the spindle, but no such difference have been mentioned to my knowledge so far in the literature. The constant remodeling of the spindle might also prevent the actual specialisation of individual bundles and the observation of different subclass could be an instant snapshot ready to rearrange totally within a short time. Furthermore, the acquired region corresponds exclusively to the midzone and the bundles of the “class 1” could easily bundle tightly to become a bundle of the “class 2”. This classification is therefore arbitrary and limited to the restricted observed area. The reconstruction of the full spindle, or at least one hemi-spindle would be important to further characterize the bundles. Also, quantifying the number of MTs belonging to each bundle class after fine modeling among several samples would be critical for a clearer understanding. Fine MT modeling would also bring insights into the overlapping of anti-parallel MT, coming from opposite poles. The presence of MTs crossing totally the midzone to reach the opposite MTOC might also be observed by fine modeling.

Scientists have also postulated the existence of “short MTs”<sup>8,19,35,141</sup>. Those MTs, nucleated at the periphery of the spindle or at the chromosome mass periphery would be progressively incorporated into the spindle.

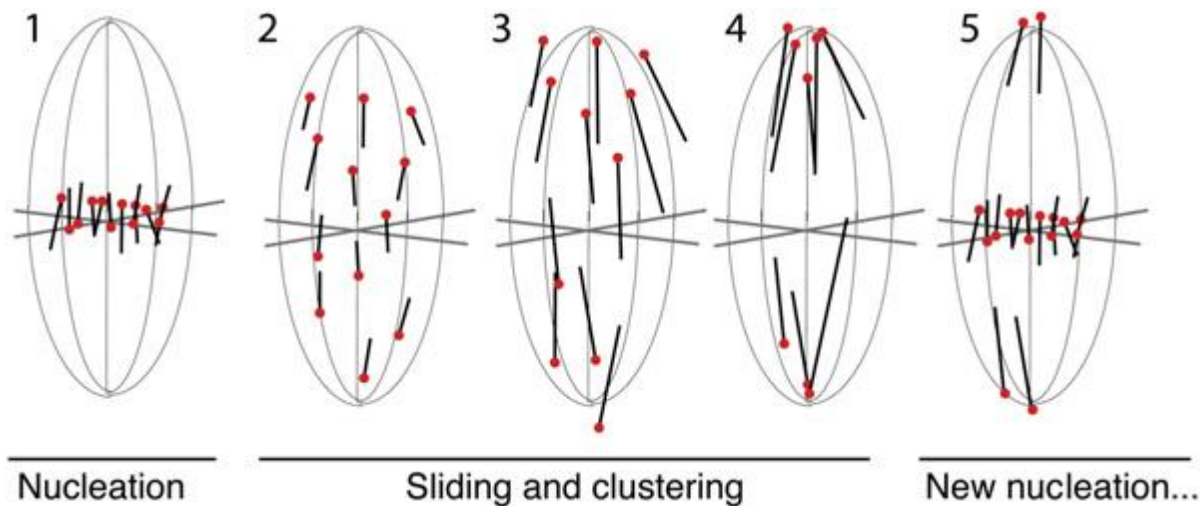


Figure 57 : Slide and cluster scenario: the MTs are nucleated at the chromosome region, get polarized and progressively slide towards the pole while new MTs are generated at the chromosome region. Taken from Burbank *et al.* 2007.

But recent observations postulated that the MTs are constantly generated throughout the whole spindle <sup>60</sup>.

Random short MT could not be observed in our current volume, however we observed non parallel MTs (p104 §e.ii.2) and we can postulate that this corresponds to a MT that has not been completely integrated in the spindle at the freezing time. But to confirm it, the tracking of the whole MT pool would be necessary, to ensure that this particular MT is not an isolated case. Also the notion of short MT shall be carefully considered. To keep the spindle coherent with even short MTs, 10 to 15µm long would be necessary. The volume we acquired is approximately this length but is centred on the chromosome mass. A 10µm long MT would still end outside of the volume therefore the existence of these short MT requires at least the reconstruction of a hemi-spindle and obviously a proper segmentation of each individual MT.

Finally, a last element of the spindle will require a close attention: the poles. The MTs are converging towards the MTOCs at the spindle poles. Their ends identification should be a majority of capped and blunt ends <sup>11</sup> but we could imagine having MTs plus ends coming from either the chromosome region <sup>151</sup> or from the opposite MTOC and serve as spindle length sensors. To get proper interpretations a clear modeling should again be done with a proper identification of the MT end morphologies. Also the general organisation of the MTs at the poles should be observed. As the MTOCs sometimes fall off the spindle <sup>5</sup> it would be

interesting to analyse if this affects the focusing of the MTs around the pole, or alters the general morphology of the MTs.

#### **h. Perspectives**

This ambitious project is a long term one and in a developmental phase. Methods still need to be developed as well as the data analysis. We have been able to vitrify and process spindles by developing a new method of correlative microscopy which will serve to study the mitotic spindle organisation after accurate modelling of the individual MTs. Although the current results are promising, the reproducibility is pending and a standardisation of the sample preparation is required. The automation of the modeling also needs further improvements and combination of different approaches might be appropriate. To date, only one partially isolated spindle could be acquired for tomography purposes. The acquired spindle allowed us to address several technical issues that are to be anticipated when working on an optimal specimen.

About standardizing the sample cryo-fixation followed by FS, a first step in this direction has been initiated with the cryo capsule that is presented in the part V of this thesis work. The success of the *X. laevis* project relies on our ability to process enough samples, acquire and analyze them.

Regarding the image acquisition procedure, a decision on the strategy mentioned in the above discussion will also depend on our ability to produce enough samples and to precisely analyse the collected data.

Once the acquisition will be overcome, the processing will be addressed. In this thesis, I did not mention in details the automatic segmentation of the MTs as I have not been involved deeply into this part of the work and the program was mainly developed by our collaborators in Berlin. However, the program used is internally limited by the amount of data it can process at a time. The intrinsic large dimensions of the biological sample result in volume that modern computers can hardly handle at once. Fractionation of the data processing is necessary. One first strategy could be to work on the individual tomograms before the joining and then to join the models. A second strategy, more global, would be to segment the bundles within the joined full volume (as done in this thesis work). Then use the

segmentation as references to extract sub-tomograms for the automatic MT tracking. As already mentioned the filtering method used in this work is not optimal and misses the individual MTs as well as the fine bundles. A manual segmentation of the missing MT could be imagined, using the capacity of the human brain to identify structures faster than a computer. This way, the computing power could be optimally used for systematic restricted area automatic tracking, and the human capacity could also be optimally used to identify isolated structures.

The MT ends identification will also be challenging. Assuming that all the MTs can be automatically tracked, an automatic end morphology identification strategy should be developed using learning algorithms or template matching approaches.

# Part V: the correlative microscopy challenge requires new tools to standardize the procedure

---

*«La chance ne sourit qu'aux esprits bien préparés.»*

*[Louis Pasteur]*

## **E- The cryo-capsule: a new versatile tool to facilitate correlative microscopy approaches.**

### **a. Introduction**

Conducting the *Xenopus* project revealed technical limitations that could not be overcome with the available material at the time of this study. As previously presented, the very low success rate of the freezing, followed by a low success rate of FS and sectioning affected our capacity to produce enough samples for a statistically relevant study. One of the main limitations was the low reproducibility of the freezing.

To address this question, a more standardized material is necessary. Ideally, this material would be easily manipulated throughout the whole experiments, would not affect the biological specimen and could be readily available prior to the experiment. The sapphire disk and the spacer ring would need a supporting non toxic material, not interfering with the light path for the live cell imaging, and the transfer to the high pressure freezer should be facilitated.

Overmolding technologies were used since the early 70s at industrial scale production to standardize the production of various materials<sup>152</sup>. Daily examples of overmolded parts are electric plugs. The metallic pins (inserts) that are conducting the electricity are surrounded by an isolating plastic layer (over moulding). To achieve this, we used injection overmolding technology.

Polymer injection overmolding is an efficient method to combine the high productivity of moulding technologies and the use of specific materials like sapphire disks or spacer ring as inserts. The polymer is usually melted into a heated screw-barrel system prior to the injection into the closed mould containing the inserts. The viscous polymer flows into the mould at a defined speed and temperature until the cavity is filled. After cooling by heat diffusion through the mould (optionally thermo-regulated), the polymer solidifies into the given shape. To reduce polymer shrinkages, a pressure is applied to the cavity during the cooling to induce a post-filling. The part can then be ejected after opening the mould.

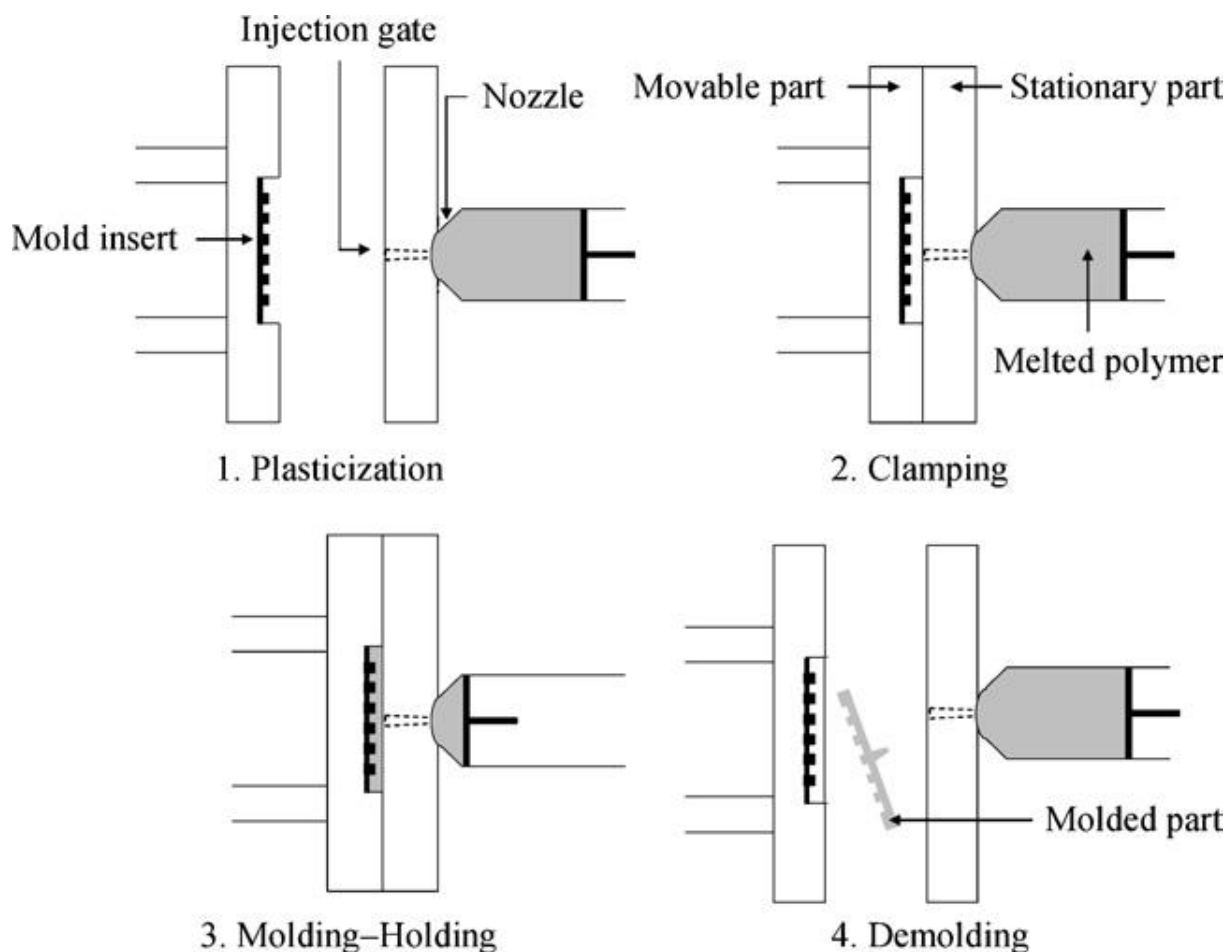


Figure 58 : Schematic drawing of the injection moulding process<sup>153</sup>

This technology, largely used in industry to produce large series of parts at minor cost, has been limited to the scale of mini-injection until recently. Most machines are able to inject comparatively large volumes of polymer from which a minor part is used for mini-moulding. Often, over 90% of the polymer used is wasted, and the cost factor increases consequently. Moreover, the cooling time increases along as well as the production cycle time.

Secondly, overmolding brittle or flexible parts (such as a sapphire disk or a gold ring) requires a gentle and precise material flow control. The mini-injection methods, using large amounts of polymer, lack precision and the polymer flow inside the mould is poorly controlled. Recent advances in micro-injection moulding ( $\mu$ IM) allow injection of lower amounts of polymers, down to less than a gram. This smaller amount of handled material permits a better control of the pressures that arise around the overmolded inserts.

Taking advantage of this recent advance in the field, we designed a device that could facilitate our biological experiments and used the discovery done during the *Xenopus*

project. The sample does not need to be tightly held, but just maintained prior to the freezing (use of the PDMS ring). We also designed the cryo-capsule to be easily manipulated by the experimentalist at all the different stages required by a correlative microscopy study.

### b. The design

Some important aspects in the design of the part had to be considered. First of all, the window of imaging defined by the inner diameter of the gold spacer ring had to remain clear from plastic on both sides of the sapphire disk for a later optimal light imaging. A second critical parameter was to keep the carbon coated sapphire disk as low as possible in the capsule to allow imaging with regular light microscope air objectives. Third, a second sapphire disk should easily be placed on top of the assembly, after the biological specimen has been placed into the cavity of the capsule, to preserve the sample from drying and external damages. Fourth, the manipulation of the capsule should be simple. And finally, the whole capsule should fit within the specimen holder (the clamp) of the high pressure freezer (HPM010).

Taking these parameters into account the first design of the capsule was adopted as follows.

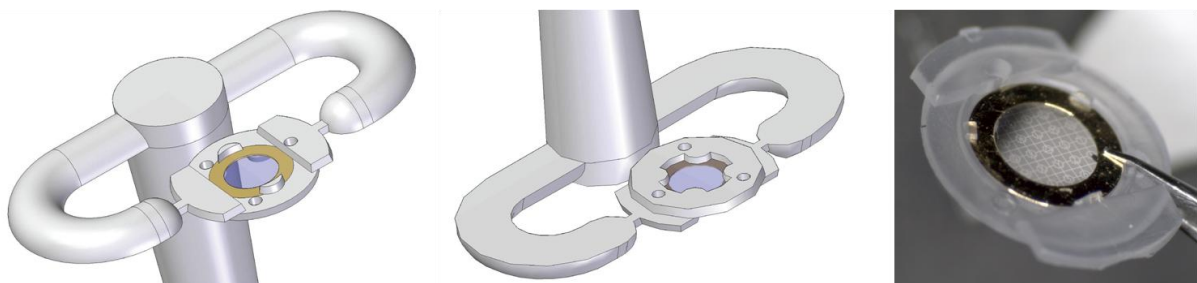


Figure 59 : Top and bottom view drawings of the cryo-capsule after overmoulding injection. The right panel show a picture of the cryo-capsule V1. The carbon coated sapphire disk is clearly land marked. The gold spacer ring shows no obvious deformation due to the overmoulding procedure.

Two ears were designed at each part of the capsule to facilitate the manipulation. The gold spacer ring was maintained by three notches (only two half moons on the schematic view) and the covering sapphire disk deposited in between them. This initial design, although very attractive at the first glance because very open and presenting many anchoring points, was not optimal to manipulate as could only be placed in two different positions in the clamp (asymmetry of the ears). We designed a second cryo-capsule completely round, removing the ears to gain orientation freedom.

For the cryo-capsule V2, we used two types of sapphire disk available: the laser etched sapphire disk (170 $\mu$ m thick, Wohlwend) and regular carbon coated sapphire disks (50 $\mu$ m thick). The mechanical resistance of the thicker sapphire disk facilitates greatly the overmoulding procedure and improves the mechanical resistance of the sapphire disk assembly during the HPF shot. It implies also a lower thermal conductivity, potentially preventing proper vitrification of the biological sample. Assuming that the freezing property is adequate, the etching of the sapphire disk leaves a negative 3D print of the correlative landmarks on the EPON block, facilitating greatly the later sectioning.

The thinner carbon coated sapphire disk already proved to have optimal freezing properties. The proper set-up of  $\mu$ IM allowed us to produce those capsules as well.

To maintain the capsule in the HPF chamber during the HPF procedure, the conventional clamp needed to be modified adequately. The tests done on the cryo-capsule V1 revealed that the presence of a metallic supporting part was necessary to freeze the biological material in the cryo-capsule without breaking the sapphire disks. On the cryo-capsule V2, the clamp was modified accordingly to be filled on one side, replacing therefore the formally used aluminium B-carrier.

### **c. The material selection**

When designing the cryo-capsule, the consideration for the material composing it was necessary. The use of sapphire disk and gold spacer ring already proved to be suitable for biological analysis. The capsule had to contain a third material: a plastic polymer which should be biological friendly, but should still support the HPF and the post-processing.

Among the constraints imposed by the experiment were the use of various chemicals (described in the material and methods) during FS. Two strategies were considered: either the capsule should dissolve quickly in the very first acetone rinses, leaving the sapphire disks completely free or, taking the opposite approach, using an inert material which would last intact throughout the whole experiment, from the LM to the FS.

Polymers rigid at 20°C that can instantly dissolve at -90°C in acetone are too complex to manipulate in a first place. We therefore took the second approach and used a High Density Polyethylene (HDPE), a commonly used component in industrial application for its low

interaction with other material due to the very low molecular polarity (plastic bottles, syringes and medical systems), and its low reactivity with solvent (inert to acetone). Moreover, HDPE is a semi-crystalline polymer for which the amorphous phase remains rubbery until -120°C, therefore stresses induced by large temperature variations are more able to relax.

#### **d. Cell growth**

The cryo-capsule was initially designed using all the experience accumulated on the *Xenopus* project and was developed to support the project in order to facilitate the HPF process of the sample using a sapphire disk assembly. However, *X. laevis* egg extracts are not trivial samples to produce and test phase should be carried out on simple systems so as not to accumulate difficulties. Therefore, the first freezing tests were done on HeLa cell, which easily grow on sapphire disks and are easy to identify by LM in an EPON plastic block, prior to the sectioning process.

Prior to the cell seeding on the cryo-capsules, the bottom of the cryo-capsules were coated with a thin film of silicon live-imaging grease to physically stick the capsules at the bottom of the Petri dishes (the capsules are cup like and float if not properly sunk into the medium). This prevented the capsules to float on the surface of the medium, and avoided the growth of cells under the sapphire disk. To ensure the adhesion of the HeLa cells at the surface of the carbon coated sapphire disk, a layer of PLL or of fibronectin was added the day prior to the cell seeding. One hour before the cell seeding, the capsules were glow discharged. The cells were adherent and didn't show obvious cell growth defects.

#### **e. Correlative microscopy**

The correlative live pictures were acquired on a Zeiss Observer Z1 microscope at 10x with an air objective. Several pictures were taken to cover the field of the capsule. The frames were then manually stitched together using MosaicJ. The printouts were used later to identify the cells of interest on the lowicryl block face.

The biological specimen was imaged relative to the carbon landmarks at 10x and 63x air objective. The low magnification was used to identify the cell of interest with respect to the

neighbouring cells and the higher magnification was used to identify precisely the phenotype of interest.

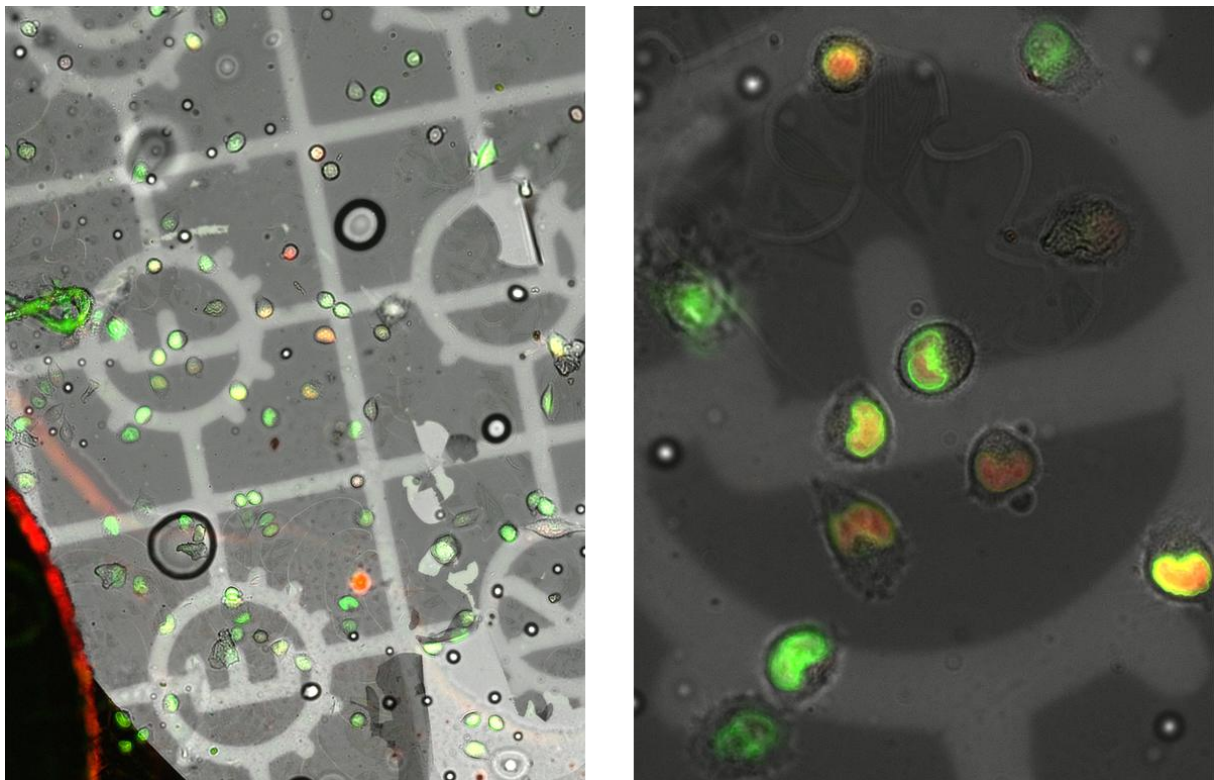


Figure 60 : Light microscopic images of HeLa cells grown at the surface of the cryocapsule. The right panel is an overview acquired at 10x where the relative organisation of all the cells can be appreciated. The left panel was acquired with a 63x air objective to avoid deposition of oil on the cryo-capsule prior to the HPF. The phenotypes can be clearly identified for the later investigation.

In some cases, the carbon landmark was damaged during the freeze substitution procedure, leaving only the embedded cells as landmarks to identify the cell of interest.

#### **f. High Pressure Freezing**

After imaging, the samples were transferred into the HPM010 clamp and directly high pressure frozen. The transfer of the cryo capsule into the HPM-clamp was done under the binocular to ensure proper positioning prior the closure. Inadequate positioning of the cryo-capsule in the HPM-clamp lead systematically to breaking one of the two sapphire disks.

We have tried to do correlative microscopy using the cryocapsule V1. The HPM-clamp holding the capsule during the HPF jet was designed to expose both sides of the capsules to the HPF jet.



Figure 61 : The clamp V1 barred or loaded with the cryo-capsule V1. On the left panel, we can observe both open sides of the clamp. The LN<sub>2</sub> jet arrives directly on the sapphires of the cryo-capsule through the holes on both sides. The two ears of the cryo-capsule need to fit within the 2 cavities of the clamp (left panel); only two possible orientations are left to load the capsule (right panel).

This direct exposition to a powerful jet of LN<sub>2</sub> leads to a systematic destruction of the sapphire disks. To prevent the destruction, we have re-oriented the clamp 90° from the LN<sub>2</sub> jet. The sapphire disks were not broken anymore during the HPF. However, the HPF chamber is filled with EtOH prior to the freezing to slow down the freezing during the pressure raise. This EtOH leaked into the cryo-capsule, lysing the cells prior to the freezing. Therefore, the cells that could be retrieved were lysed and could not be used for electron microscopic studies (Figure 62).

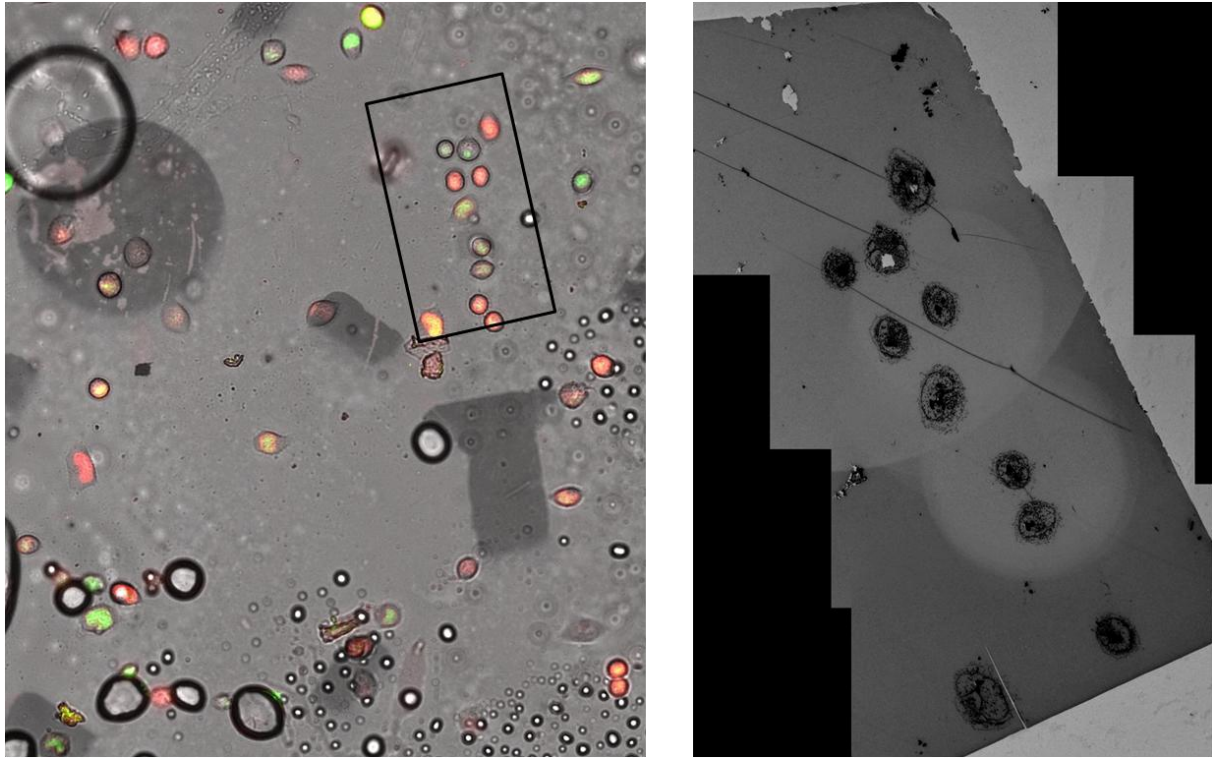


Figure 62 : Correlative imaging of HeLa cells. On the left panel, a small colony of HeLa cells have been imaged and localised. These cells were retrieved on the plastic bloc and serial sectioned (right). The structures are damaged and only the outline of the cells can be identified.

We therefore designed the cryo-capsule V2 to correct the performances of the first cryo-capsule. We removed the single axis symmetry (the two ears) and designed a new clamp to protect the cryo-capsule during the HPF jet and prevent the sapphires disks from breaking. The clamp V2 is made of aluminium, asymmetric, with one side closed with a 200 $\mu$ m thick membrane (equivalent to the conventional B carrier) used as a support for the closing sapphire disk. The flexible element of the clamp is folding on the bottom of the cryo-capsule V2, maintaining it closed and tight from EtOH infiltration.

By lack of time, we have not been able to test this new cryo-capsule and the tests shall be proceeded in the near future.

#### **g. Physical properties of the cryo-capsule**

The following calculations were kindly done by Pr Dr Gilles Régnier.

The heat penetration can be estimated by the following equation:

$$\theta \cong \frac{e^2}{a}$$

where “e” is the thickness and “a” the diffusivity (for polymers like PEHD,  $10e^{-7}m^2/s$ )

The diffusivity “a” is defined by:

$$a = \frac{\kappa}{\rho C_p}$$

where “κ” is the conductivity, “ρ” the and “Cp” the heat capacity.

	Sapphire	Aluminium
Volumic mass (kg/m <sup>3</sup> )	4000	2700
Cp (J.kg <sup>-1</sup> .K <sup>-1</sup> )	800	900
Conductivity (W.m <sup>-1</sup> .K <sup>-1</sup> )	40	200
Diffusivity (m <sup>2</sup> /s)	1.3E-05	8.2E-05

Table 1: Thermal properties order of magnitude of sapphire and aluminium.

	Thickness (m)	Time (s)
Sapphire	5.00E-05	2.00E-04
Sapphire	1.70E-04	2.31E-03
Aluminium	2.00E-04	4,86E-04

Table 2: Heat penetration time of sapphire and aluminium according to their thickness (kindly calculated by Pr Dr Gilles Régnier).

The conventional procedure of HPF with the HPM010 requires using two aluminium carriers with a 200µm thick support membrane. The heat penetration time for these carrier walls is approximately 0.5ms.

The heat penetration time in 50µm and 170µm thick sapphire disks are 0.2 and 2.3ms respectively. This varies with the square of the thickness. The 170µm therefore clearly slows down the cooling time.

For the capsule V1, two 50µm thick sapphires are used so the heat penetration time is theoretically better than in the conventional procedure using the two aluminium carriers. Using the capsule V2, two different configurations are used: the substrate sapphire is either 50µm thick with a carbon land marking or 170µm thick with a laser etched land marking. In both cases, a 50µm thick sapphire is used to close the capsule. As the capsule is closed on one hand by a 200µm thick aluminium membrane, we can assume that the thin capsule should have good freezing properties from the bare sapphire side. This will require experimental confirmation. The freezing properties of the 170µm thick sapphire disk V2 cryo-capsule should also be experimentally established.

## **h. Conclusion and perspectives**

As we discussed in the chapter IV, the *X. laevis* meiotic spindle have been extensively used and studied by scientist to understand the underlying mechanisms of mitosis. Our investigations lead us to develop a new correlative light and electron microscopic method which allowed us to HPF, for the first time to our knowledge, an in vitro specimen and to retrieve it after FS for EM work. However, this method is not reliable and many attempts were necessary to obtain one single sample that we could use for our project. This low reproducibility rate is a major limiting factor and we have therefore investigated new ways to achieve a high reproducibility of sample freezing, using the knowledge accumulated during this PhD period.

The necessity to have a chamber that we could easily manipulate during the whole CLEM experiment, from HPF to EM, was a limiting step in our work. To achieve reproducibility, standardisation of parts is mandatory and industrial processes can play a key role in this standardisation. Industries have used for long the “tailor-made” advantages of thermo-plastic transformation to create identical parts at large scale for minor cost and reduced production times. Our collaborators in Paris have recently developed a new technology that allows them to precisely transform very small amounts of melted plastic polymer with a sharp control on the pressure and material flow within the mould during the moulding process. Maintaining such small and fragile inserts without breaking it (not too much pressure prior to the over-moulding) while avoiding leaks of the melted polymer on top of the sapphire (keeping enough pressure on top of the inserts to avoid irregular over-moulding) was challenging. In both designs, the sapphire disk and the gold spacer ring were maintained in an adequate shape for the cryocapsule to be used.

The cryo-capsule project has not yet reached its conclusion and the most important part remains to be obtained: the proof of principle that vitrification occurs adequately. This project was initiated very late during this PhD work but milestones have already been reached like the production of the capsule in two different designs. The correlative microscopy will then need to be realized to prove the efficiency of this new technology.

Further developments will then be necessary to improve the transfer time between the LM and the HPF down to 10 seconds. This limit, although arbitrary also fits many biological

phenomenon. Indeed most biological processes occur very fast, generally within the range of the millisecond. Correlative microscopy will also need further developments like the ability to overlap the LM and the EM images and do some best fitting to accurately correlate the LM signal in 3D, relative to the EM dataset collected.

The capsule will also require some remodeling evolution like the increase in thickness of the gold spacer ring to 100 or 200 $\mu\text{m}$ . Increasing the cavity depth, the number of samples that could be observed will also increase. Starfish oocytes, typically around 175 $\mu\text{m}$  could be followed live before HPF to study early stage developments, like with *C. elegans* early embryonic development.

Using micro-patterning techniques, selective reverse transcription could be applied to cell cultures and siRNA experiments could be followed to accurately immobilise the cells at a given time following fluorescent markers. Likewise, cell migration on pattern could be developed to study the cytoskeleton in defined staged of the migration.

Using concanavalin A, monolayer of yeast cells could also be followed prior to immobilisation.

Finally, the cryo-capsule should be adapted to fit with the two other existing HPF machine on the market: the HPM100 and the EMPACT 2 from Leica. Broadening its use would also bring new ideas and perspective to use the cryo-capsule adequately.

## Part VI: Electron tomography is an emerging central player for structural cellular biology

---

## **F- General discussions on the three projects, their limitations and their potential**

In this thesis, the questions raised by each project have been discussed in the corresponding chapters. Therefore, I would like to finish with a more general discussion regarding the main technology used throughout this PhD: electron microscopy.

ET has been used since the 1930s in medicine to improve the imaging quality for diagnostics. However, it became more accessible with the development of computing power since the 90s<sup>90</sup>. This accessibility opened a new branch in the EM field. Our ability to identify structures and proteins in their native 3D environment at resolutions down to 2nm is a major breakthrough for our understanding of physiological phenomenon at the cellular level. Several existing techniques have been adapted to optimally use this new ability, like cryo sectioning of high pressure frozen samples to identify individual proteins with respect to their surrounding neighbours; also using the optimal sample preservation of HPF, the use of the FS promoted studies on larger scales, up to the cellular level<sup>148</sup>. Interpreting these new types of 3D images has also been a challenge. A new resolution brings a new level of understanding and complexity; nowadays, visual interpretation needs to be completed with a more systematic computational interpretation. In this thesis work, the visual interpretation reached two times a limit where computational interpretation became inevitable. The structure of the SPB, without its intrinsic biological limitations, could be observed to a comparable level of understanding with formal studies where samples could not be observed in their native environment<sup>55,62</sup>. This approach, without improving the formally established results, could confirm previous observations and interpretations. We can therefore anticipate that the combination of better imaging capacity, precise biological specimen selection and computing interpretation improvement, will lead to a complete new level of molecular mechanism understanding.

When working at the cellular level, the molecules are not native anymore due to the FS, but the physiology is so close to the native state that the interpretation is less subject to protocols artefacts. In such conditions, understanding complex networks like mitotic

spindles become achievable even on large scales such as in the *X. laevis* mitotic spindle. However, technical limitations are not yet all overcome and much is left to standardize protocols and systematize the experiments. Automation shall become a key player in most experiments to reduce the human factor to its strict necessity and it shall be considered at every step through the intellectual path of research. Industrial players are pushing in this direction, like Leica with the automation of the FS procedure (AFS 2) or the improvement of the HPF. The microscopes are also getting automated, through their acquisition programs (micro-manager, SerialEM), but more recently also in the sample handling (Titan Kryos Microscope, FEI; 3View SEM Microscope, Gatan-FEI). This automation will not only reduce the human error, but will also lead to faster and more reliable data production. The need will then progressively be shifted towards the analysis of the information rather than its production.

This systematization will also give us more freedom in the design of our experiments and analyzing a phenomenon from different approaches will be accessible. One of these approaches will be correlative microscopy. Reducing the time resolution between the dynamic and specific LM and the cryo-immobilization is one of the key elements today to improve our understanding of dynamic phenomenon. The cryo-capsule designed in the frame of this PhD work is meant to be one potential solution to ease and reduce the manipulations between the sample preparation and the cryo-immobilisation. By this, we shall be able to improve the sample preparation reproducibility and thus generate more samples, improving thereafter the statistical relevance of our observations.

When the technical factor will be mastered, we will be able to work more with the biology: mutating, silencing, down or up regulating proteins in the *X. laevis* mitotic extract like is done with light microscopic experiments. Also new imaging it at high resolution, detecting colocalization to highlight phenotypes, like it is currently done on a daily basis with smaller organisms (Höög, 2007; M252üller-Reichert, Greenan, O'Toole, & Martin Srayko, 2010; Roque & C Antony, 2010; Roque, Ward, Murrells, Brunner, & Claude Antony, 2010).

# Bibliography

---

## G- Bibliography

1. Wühr, M., Dumont, S., Groen, A., Needleman, D.J. & Mitchison, T.J. How does a millimeter-sized cell find its center? *Cell cycle (Georgetown, Tex.)* **8**, 1115-21 (2009).
2. Wühr, M. et al. Evidence for an upper limit to mitotic spindle length. *Current biology : CB* **18**, 1256-61 (2008).
3. O'Toole, E.T. et al. Three-dimensional analysis and ultrastructural design of mitotic spindles from the cdc20 mutant of *Saccharomyces cerevisiae*. *Molecular biology of the cell* **8**, 1-11 (1997).
4. Heald, R. et al. Self-organization of microtubules into bipolar spindles around artificial chromosomes in *Xenopus* egg extracts. *Nature* **382**, 420-5 (1996).
5. Heald, R., Tournebize, R., Habermann, A., Karsenti, E. & Hyman, A.A. Spindle assembly in *Xenopus* egg extracts: respective roles of centrosomes and microtubule self-organization. *The Journal of cell biology* **138**, 615-28 (1997).
6. Karsenti, E. & Vernos, I. The mitotic spindle: a self-made machine. *Science (New York, N.Y.)* **294**, 543-7 (2001).
7. Walczak, C.E., Vernos, I., Mitchison, T.J., Karsenti, E. & Heald, R. A model for the proposed roles of different microtubule-based motor proteins in establishing spindle bipolarity. *Current biology : CB* **8**, 903-13 (1998).
8. Loughlin, R., Heald, R. & Nédélec, F. A computational model predicts *Xenopus* meiotic spindle organization. *The Journal of cell biology* **191**, 1239-49 (2010).
9. Kollman, J.M. et al. The structure of the gamma-tubulin small complex: implications of its architecture and flexibility for microtubule nucleation. *Molecular biology of the cell* **19**, 207-15 (2008).
10. Moritz, M., Braunfeld, M.B., Guénebaut, V., Heuser, J. & Agard, D.A. Structure of the gamma-tubulin ring complex: a template for microtubule nucleation. *Nature cell biology* **2**, 365-70 (2000).
11. O'Toole, E.T. et al. Morphologically distinct microtubule ends in the mitotic centrosome of *Caenorhabditis elegans*. *The Journal of cell biology* **163**, 451-6 (2003).
12. Amos, L. & Klug, A. Arrangement of subunits in flagellar microtubules. *Journal of cell science* **14**, 523-49 (1974).
13. Nogales, E., Whittaker, M., Milligan, R. a & Downing, K.H. High-resolution model of the microtubule. *Cell* **96**, 79-88 (1999).
14. Li, H., DeRosier, D.J., Nicholson, W.V., Nogales, E. & Downing, K.H. Microtubule structure at 8 Å resolution. *Structure (London, England : 1993)* **10**, 1317-28 (2002).

15. Chrétien, D., Metoz, F., Verde, F., Karsenti, E. & Wade, R.H. Lattice defects in microtubules: protofilament numbers vary within individual microtubules. *The Journal of cell biology* **117**, 1031-40 (1992).
16. Howard, J. & Hyman, A. a Dynamics and mechanics of the microtubule plus end. *Nature* **422**, 753-8 (2003).
17. Kristofferson, D., Mitchison, T.J. & Kirschner, M. Direct observation of steady-state microtubule dynamics. *The Journal of cell biology* **102**, 1007-19 (1986).
18. Howard, J. & Hyman, A.A. Growth, fluctuation and switching at microtubule plus ends. *Nature reviews. Molecular cell biology* **10**, 569-74 (2009).
19. Burbank, K.S., Groen, A., Perlman, Z.E., Fisher, D.S. & Mitchison, T.J. A new method reveals microtubule minus ends throughout the meiotic spindle. *The Journal of cell biology* **175**, 369-75 (2006).
20. Gard, D.L. & Kirschner, M.W. A microtubule-associated protein from *Xenopus* eggs that specifically promotes assembly at the plus-end. *The Journal of cell biology* **105**, 2203-15 (1987).
21. Gard, D.L. & Kirschner, M.W. Microtubule assembly in cytoplasmic extracts of *Xenopus* oocytes and eggs. *The Journal of cell biology* **105**, 2191-201 (1987).
22. Tournebize, R. et al. Control of microtubule dynamics by the antagonistic activities of XMAP215 and XKCM1 in *Xenopus* egg extracts. *Nature cell biology* **2**, 13-9 (2000).
23. Popov, A.V., Severin, F. & Karsenti, E. XMAP215 is required for the microtubule-nucleating activity of centrosomes. *Current biology : CB* **12**, 1326-30 (2002).
24. Wordeman, L. & Mitchison, T.J. Identification and partial characterization of mitotic centromere-associated kinesin, a kinesin-related protein that associates with centromeres during mitosis. *The Journal of cell biology* **128**, 95-104 (1995).
25. Goodwin, S.S. & Vale, R.D. Patronin regulates the microtubule network by protecting microtubule minus ends. *Cell* **143**, 263-74 (2010).
26. Belmont, L.D., Hyman, A.A., Sawin, K.E. & Mitchison, T.J. Real-time visualization of cell cycle-dependent changes in microtubule dynamics in cytoplasmic extracts. *Cell* **62**, 579-89 (1990).
27. Wittmann, T., Boleti, H., Antony, C., Karsenti, E. & Vernos, I. Localization of the kinesin-like protein Xklp2 to spindle poles requires a leucine zipper, a microtubule-associated protein, and dynein. *The Journal of cell biology* **143**, 673-85 (1998).
28. Wittmann, T., Wilm, M., Karsenti, E. & Vernos, I. TPX2, A novel *xenopus* MAP involved in spindle pole organization. *The Journal of cell biology* **149**, 1405-18 (2000).
29. Schatz, C. a et al. Importin alpha-regulated nucleation of microtubules by TPX2. *The EMBO journal* **22**, 2060-70 (2003).

30. Carazo-Salas, R.E., Gruss, O.J., Mattaj, I.W. & Karsenti, E. Ran-GTP coordinates regulation of microtubule nucleation and dynamics during mitotic-spindle assembly. *Nature cell biology* **3**, 228-34 (2001).
31. Gruss, O.J. et al. Ran induces spindle assembly by reversing the inhibitory effect of importin alpha on TPX2 activity. *Cell* **104**, 83-93 (2001).
32. Gruss, O.J. & Vernos, I. The mechanism of spindle assembly: functions of Ran and its target TPX2. *The Journal of cell biology* **166**, 949-55 (2004).
33. Mahoney, N.M., Goshima, G., Douglass, A.D. & Vale, R.D. Making microtubules and mitotic spindles in cells without functional centrosomes. *Current biology : CB* **16**, 564-9 (2006).
34. Gennerich, A. & Vale, R.D. Walking the walk: how kinesin and dynein coordinate their steps. *Current opinion in cell biology* **21**, 59-67 (2009).
35. Burbank, K.S., Mitchison, T.J. & Fisher, D.S. Slide-and-cluster models for spindle assembly. *Current biology : CB* **17**, 1373-83 (2007).
36. Mitchison, T.J. Mechanism and function of poleward flux in *Xenopus* extract meiotic spindles. *Philosophical transactions of the Royal Society of London. Series B, Biological sciences* **360**, 623-9 (2005).
37. Miyamoto, D.T., Perlman, Z.E., Burbank, K.S., Groen, A.C. & Mitchison, T.J. The kinesin Eg5 drives poleward microtubule flux in *Xenopus laevis* egg extract spindles. *The Journal of cell biology* **167**, 813-8 (2004).
38. Sharp, D.J. et al. The bipolar kinesin, KLP61F, cross-links microtubules within inter-polar microtubule bundles of *Drosophila* embryonic mitotic spindles. *The Journal of cell biology* **144**, 125-38 (1999).
39. Kapitein, L.C. et al. The bipolar mitotic kinesin Eg5 moves on both microtubules that it crosslinks. *Nature* **435**, 114-8 (2005).
40. Carter, A.P., Cho, C., Jin, L. & Vale, R.D. Crystal structure of the dynein motor domain. *Science (New York, N.Y.)* **331**, 1159-65 (2011).
41. Roque, H., Ward, J.J., Murrells, L., Brunner, D. & Antony, C. The fission yeast XMAP215 homolog Dis1p is involved in microtubule bundle organization. *PloS one* **5**, e14201 (2010).
42. Loughlin, R., Riggs, B. & Heald, R. SnapShot: motor proteins in spindle assembly. *Cell* **134**, 548-548.e1 (2008).
43. Lyle, K., Kumar, P. & Wittmann, T. SnapShot: Microtubule Regulators I. *Cell* **136**, 380, 380.e1 (2009).
44. Bettencourt-Dias, M. & Glover, D.M. SnapShot: centriole biogenesis. *Cell* **136**, 188-188.e1 (2009).

45. Pelletier, L., O'Toole, E.T., Schwager, A., Hyman, A.A. & Müller-Reichert, T. Centriole assembly in *Caenorhabditis elegans*. *Nature* **444**, 619-23 (2006).
46. Adams, I.R. & Kilmartin, J.V. Spindle pole body duplication: a model for centrosome duplication. *Trends Cell Biol* **10**, 329-335 (2000).
47. Lim, H.H., Zhang, T. & Surana, U. Regulation of centrosome separation in yeast and vertebrates: common threads. *Trends in cell biology* **19**, 325-33 (2009).
48. Jaspersen, S.L. & Winey, M. The budding yeast spindle pole body: structure, duplication, and function. *Annual review of cell and developmental biology* **20**, 1-28 (2004).
49. Ohi, R., Coughlin, M.L., Lane, W.S. & Mitchison, T.J. An inner centromere protein that stimulates the microtubule depolymerizing activity of a KinI kinesin. *Developmental cell* **5**, 309-21 (2003).
50. Maddox, P., Straight, A., Coughlin, P., Mitchison, T.J. & Salmon, E.D. Direct observation of microtubule dynamics at kinetochores in *Xenopus* extract spindles: implications for spindle mechanics. *The Journal of cell biology* **162**, 377-82 (2003).
51. DeLuca, J.G. et al. Hec1 and nuf2 are core components of the kinetochore outer plate essential for organizing microtubule attachment sites. *Molecular biology of the cell* **16**, 519-31 (2005).
52. Dong, Y., Vanden Beldt, K.J., Meng, X., Khodjakov, A. & McEwen, B.F. The outer plate in vertebrate kinetochores is a flexible network with multiple microtubule interactions. *Nature cell biology* **9**, 516-22 (2007).
53. McEwen, B.F., Dong, Y. & VandenBeldt, K.J. Using electron microscopy to understand functional mechanisms of chromosome alignment on the mitotic spindle. *Methods in cell biology* **79**, 259-93 (2007).
54. Khodjakov, A., Copenagle, L., Gordon, M.B., Compton, D.A. & Kapoor, T.M. Minus-end capture of preformed kinetochore fibers contributes to spindle morphogenesis. *The Journal of cell biology* **160**, 671-83 (2003).
55. O'Toole, E.T., Winey, M. & McIntosh, J.R. High-voltage electron tomography of spindle pole bodies and early mitotic spindles in the yeast *Saccharomyces cerevisiae*. *Molecular biology of the cell* **10**, 2017-31 (1999).
56. Pereira, G., Knop, M. & Schiebel, E. Spc98p directs the yeast gamma-tubulin complex into the nucleus and is subject to cell cycle-dependent phosphorylation on the nuclear side of the spindle pole body. *Molecular biology of the cell* **9**, 775-793 (1998).
57. Elliott, S., Knop, M., Schlenstedt, G. & Schiebel, E. Spc29p is a component of the Spc110p subcomplex and is essential for spindle pole body duplication. *Proceedings of the National Academy of Sciences of the United States of America* **96**, 6205-10 (1999).

58. Muller, E.G.D. et al. The organization of the core proteins of the yeast spindle pole body. *Molecular biology of the cell* **16**, 3341-52 (2005).
59. Li, S. et al. Structural role of Sfi1p-centrin filaments in budding yeast spindle pole body duplication. *The Journal of cell biology* **173**, 867-77 (2006).
60. Needleman, D.J. et al. Fast microtubule dynamics in meiotic spindles measured by single molecule imaging: evidence that the spindle environment does not stabilize microtubules. *Molecular biology of the cell* **21**, 323-33 (2010).
61. Grishchuk, E.L. & McIntosh, J.R. Microtubule depolymerization can drive poleward chromosome motion in fission yeast. *EMBO J.* **25**, 4888-4896 (2006).
62. Bullitt, E., Rout, M.P., Kilmartin, J.V. & Akey, C.W. The yeast spindle pole body is assembled around a central crystal of Spc42p. *Cell* **89**, 1077-86 (1997).
63. Heuser, J.E. et al. Synaptic vesicle exocytosis captured by quick freezing and correlated with quantal transmitter release. *The Journal of cell biology* **81**, 275-300 (1979).
64. Dubochet, J. & Sartori Blanc, N. The cell in absence of aggregation artifacts. *Micron (Oxford, England : 1993)* **32**, 91-9 (2001).
65. McDonald, K.L., Morphey, M., Verkade, P. & Müller-Reichert, T. Recent advances in high-pressure freezing: equipment- and specimen-loading methods. *Methods in molecular biology (Clifton, N.J.)* **369**, 143-73 (2007).
66. McDonald, K.L. & Müller-Reichert, T. Cryomethods for thin section electron microscopy. *Methods in enzymology* **351**, 96-123 (2002).
67. McEwen, B.F., Hsieh, C.E., Mattheyses, a L. & Rieder, C.L. A new look at kinetochore structure in vertebrate somatic cells using high-pressure freezing and freeze substitution. *Chromosoma* **107**, 366-75 (1998).
68. Moor, H., Bellin, G., Sandri, C. & Akert, K. The influence of high pressure freezing on mammalian nerve tissue. *Cell and tissue research* **209**, 201-16 (1980).
69. Moor, H. *Cryotechniques in biological electron microscopy.* 297 (1987).doi:OL2393773M
70. Kolotuev, I., Schwab, Y. & Labouesse, M. A precise and rapid mapping protocol for correlative light and electron microscopy of small invertebrate organisms. *Biology of the cell / under the auspices of the European Cell Biology Organization* **102**, 121-32 (2010).
71. Verkade, P. Moving EM: the Rapid Transfer System as a new tool for correlative light and electron microscopy and high throughput for high-pressure freezing. *Journal of microscopy* **230**, 317-28 (2008).

72. Rijnsoever, C.V., Oorschot, V. & Klumperman, J. Correlative light-electron microscopy (CLEM) combining live-cell imaging and immunolabeling of ultrathin cryosections. *Cell* **5**, 973-980 (2008).
73. Grabenbauer, M. et al. Correlative microscopy and electron tomography of GFP through photooxidation. *Nature Methods* **2**, 857-862 (2005).
74. Müller-Reichert, T., Srayko, M., Hyman, A., O'Toole, E.T. & McDonald, K.L. Correlative light and electron microscopy of early *Caenorhabditis elegans* embryos in mitosis. *Methods in cell biology* **79**, 101-19 (2007).
75. Kukulski, W. et al. Correlated fluorescence and 3D electron microscopy with high sensitivity and spatial precision. *The Journal of cell biology* 1-10 (2011).doi:10.1083/jcb.201009037
76. Nixon, S.J. et al. A single method for cryofixation and correlative light, electron microscopy and tomography of zebrafish embryos. *Traffic (Copenhagen, Denmark)* **10**, 131-6 (2009).
77. Müller-Reichert, T., Hohenberg, H., O'Toole, E.T. & McDonald, K.L. Cryoimmobilization and three-dimensional visualization of *C. elegans* ultrastructure. *Journal of microscopy* **212**, 71-80 (2003).
78. Roque, H. & Antony, C. Fission yeast a cellular model well suited for electron microscopy investigations. *Methods in cell biology* **96**, 235-58 (2010).
79. Dubochet, J. et al. Cryo-electron microscopy of vitrified specimens. *Quarterly reviews of biophysics* **21**, 129-228 (1988).
80. Richter, K. A cryoglue to mount vitreous biological specimens for cryoultramicrotomy at 110K. *Journal of microscopy* **173**, 143-7 (1994).
81. Al-Amoudi, A., Studer, D. & Dubochet, J. Cutting artefacts and cutting process in vitreous sections for cryo-electron microscopy. *Journal of structural biology* **150**, 109-21 (2005).
82. Al-Amoudi, A. et al. Cryo-electron microscopy of vitreous sections. *The EMBO journal* **23**, 3583-8 (2004).
83. Al-Amoudi, A., Dubochet, J., Gnaegi, H., Lüthi, W. & Studer, D. An oscillating cryo-knife reduces cutting-induced deformation of vitreous ultrathin sections. *Journal of microscopy* **212**, 26-33 (2003).
84. Pierson, J. et al. Improving the technique of vitreous cryo-sectioning for cryo-electron tomography: electrostatic charging for section attachment and implementation of an anti-contamination glove box. *Journal of structural biology* **169**, 219-25 (2010).
85. Rout, M.P. & Kilmartin, J.V. Components of the yeast spindle and spindle pole body. *The Journal of cell biology* **111**, 1913-27 (1990).

86. Kohl, L.R.H. *Transmission Electron Microscopy*. **36**, 15 (Springer New York: New York, NY, 2008).
87. Zheng, Q.S., Braunfeld, M.B., Sedat, J.W. & Agard, D. a An improved strategy for automated electron microscopic tomography. *Journal of structural biology* **147**, 91-101 (2004).
88. Zheng, S.Q., Sedat, J.W. & Agard, D.A. Automated data collection for electron microscopic tomography. *Methods in enzymology* **481**, 283-315 (2010).
89. Castaño-Díez, D., Scheffer, M., Al-Amoudi, A. & Frangakis, A.S. Alignator: a GPU powered software package for robust fiducial-less alignment of cryo tilt-series. *Journal of structural biology* **170**, 117-26 (2010).
90. Kremer, J.R., Mastronarde, D.N. & McIntosh, J.R. Computer visualization of three-dimensional image data using IMOD. *Journal of structural biology* **116**, 71-6 (1996).
91. Cross, M.K. & Powers, M.A. Learning about cancer from frogs: analysis of mitotic spindles in *Xenopus* egg extracts. *Disease models & mechanisms* **2**, 541-7 (2009).
92. Desai, A., Murray, A., Mitchison, T.J. & Walczak, C.E. The use of *Xenopus* egg extracts to study mitotic spindle assembly and function in vitro. *Methods in cell biology* **61**, 385-412 (1999).
93. Folch, a, Jo, B.H., Hurtado, O., Beebe, D.J. & Toner, M. Microfabricated elastomeric stencils for micropatterning cell cultures. *Journal of biomedical materials research* **52**, 346-53 (2000).
94. Folch, A., Ayon, A., Hurtado, O., Schmidt, M.A. & Toner, M. Molding of deep polydimethylsiloxane microstructures for microfluidics and biological applications. *Journal of biomechanical engineering* **121**, 28-34 (1999).
95. Hawes, P., Netherton, C.L., Mueller, M., Wileman, T. & Monaghan, P. Rapid freeze-substitution preserves membranes in high-pressure frozen tissue culture cells. *Journal of microscopy* **226**, 182-9 (2007).
96. McIntosh, J.R. et al. Fibrils connect microtubule tips with kinetochores: a mechanism to couple tubulin dynamics to chromosome motion. *Cell* **135**, 322-33 (2008).
97. Mastronarde, D.N. Automated electron microscope tomography using robust prediction of specimen movements. *Journal of structural biology* **152**, 36-51 (2005).
98. Mastronarde, D.N. Dual-axis tomography: an approach with alignment methods that preserve resolution. *Journal of structural biology* **120**, 343-52 (1997).
99. Luther, P.K., Lawrence, M.C. & Crowther, R.A. A method for monitoring the collapse of plastic sections as a function of electron dose. *Ultramicroscopy* **24**, 7-18 (1988).
100. Hayward, S.B. & Glaeser, R.M. Radiation damage of purple membrane at low temperature. *Ultramicroscopy* **04**, 201-10 (1979).

101. Höög, J.L. & Antony, C. *Cellular Electron Microscopy. Methods in cell biology* **79**, 145-67 (Elsevier: 2007).
102. Höög, J.L. et al. Organization of interphase microtubules in fission yeast analyzed by electron tomography. *Developmental cell* **12**, 349-61 (2007).
103. Byers, B. & Goetsch, L. Duplication of spindle plaques and integration of the yeast cell cycle. *Cold Spring Harbor symposia on quantitative biology* **38**, 123-31 (1974).
104. Byers, B. & Goetsch, L. Behavior of spindles and spindle plaques in the cell cycle and conjugation of *Saccharomyces cerevisiae*. *Journal of bacteriology* **124**, 511-23 (1975).
105. Robinow, C.F. & Marak, J. A fiber apparatus in the nucleus of the yeast cell. *The Journal of cell biology* **29**, 129-51 (1966).
106. Adams, I.R. & Kilmartin, J.V. Localization of core spindle pole body (SPB) components during SPB duplication in *Saccharomyces cerevisiae*. *The Journal of cell biology* **145**, 809-23 (1999).
107. Donaldson, a D. & Kilmartin, J.V. Spc42p: a phosphorylated component of the *S. cerevisiae* spindle pole body (SPD) with an essential function during SPB duplication. *The Journal of cell biology* **132**, 887-901 (1996).
108. McIntosh, J.R. & O'Toole, E.T. Life cycles of yeast spindle pole bodies: getting microtubules into a closed nucleus. *Biology of the cell / under the auspices of the European Cell Biology Organization* **91**, 305-12 (1999).
109. Souès, S. & Adams, I.R. SPC72: a spindle pole component required for spindle orientation in the yeast *Saccharomyces cerevisiae*. *Journal of cell science* **111** ( Pt 1, 2809-18 (1998).
110. Vinh, D.B.N., Kern, J.W., Hancock, W.O., Howard, J. & Davis, T.N. Reconstitution and characterization of budding yeast gamma-tubulin complex. *Molecular biology of the cell* **13**, 1144-57 (2002).
111. Kilmartin, J.V. & Goh, P.Y. Spc110p: assembly properties and role in the connection of nuclear microtubules to the yeast spindle pole body. *The EMBO journal* **15**, 4592-602 (1996).
112. Knop, M. & Schiebel, E. Spc98p and Spc97p of the yeast gamma-tubulin complex mediate binding to the spindle pole body via their interaction with Spc110p. *The EMBO journal* **16**, 6985-95 (1997).
113. Nguyen, T., Vinh, D.B., Crawford, D.K. & Davis, T.N. A genetic analysis of interactions with Spc110p reveals distinct functions of Spc97p and Spc98p, components of the yeast gamma-tubulin complex. *Molecular biology of the cell* **9**, 2201-16 (1998).

114. Schaerer, F., Morgan, G., Winey, M. & Philippsen, P. Cnm67p is a spacer protein of the *Saccharomyces cerevisiae* spindle pole body outer plaque. *Molecular biology of the cell* **12**, 2519-33 (2001).
115. Zizlsperger, N., Malashkevich, V.N., Pillay, S. & Keating, A.E. Analysis of coiled-coil interactions between core proteins of the spindle pole body. *Biochemistry* **47**, 11858-68 (2008).
116. Winey, M., Goetsch, L., Baum, P. & Byers, B. MPS1 and MPS2: novel yeast genes defining distinct steps of spindle pole body duplication. *The Journal of cell biology* **114**, 745-54 (1991).
117. Kilmartin, J.V. Sfi1p has conserved centrin-binding sites and an essential function in budding yeast spindle pole body duplication. *The Journal of cell biology* **162**, 1211-21 (2003).
118. Jaspersen, S.L., Giddings, T.H. & Winey, M. Mps3p is a novel component of the yeast spindle pole body that interacts with the yeast centrin homologue Cdc31p. *The Journal of cell biology* **159**, 945-56 (2002).
119. Byers, B. & Goetsch, L. Electron microscopic observations on the meiotic karyotype of diploid and tetraploid *Saccharomyces cerevisiae*. *Proceedings of the National Academy of Sciences of the United States of America* **72**, 5056-60 (1975).
120. Roof, D.M., Meluh, P.B. & Rose, M.D. Kinesin-related proteins required for assembly of the mitotic spindle. *The Journal of cell biology* **118**, 95-108 (1992).
121. Jacobs, C.W., Adams, A.E., Szaniszló, P.J. & Pringle, J.R. Functions of microtubules in the *Saccharomyces cerevisiae* cell cycle. *The Journal of cell biology* **107**, 1409-26 (1988).
122. Al-Amoudi, A., Díez, D.C., Betts, M.J. & Frangakis, A.S. The molecular architecture of cadherins in native epidermal desmosomes. *Nature* **450**, 832-7 (2007).
123. Shenoy, S.R. & Jayaram, B. Proteins: sequence to structure and function--current status. *Current protein & peptide science* **11**, 498-514 (2010).
124. Klenchin, V. a, Frye, J.J., Jones, M.H., Winey, M. & Rayment, I. Structure-function analysis of the C-terminal domain of CNM67, a core component of the *Saccharomyces cerevisiae* spindle pole body. *The Journal of biological chemistry* (2011).doi:10.1074/jbc.M111.227371
125. Al-Amoudi, A., Norlen, L.P.O. & Dubochet, J. Cryo-electron microscopy of vitreous sections of native biological cells and tissues. *Journal of structural biology* **148**, 131-5 (2004).
126. Sartori Blanc, N., Senn, A., Leforestier, A., Livolant, F. & Dubochet, J. DNA in human and stallion spermatozoa forms local hexagonal packing with twist and many defects. *Journal of structural biology* **134**, 76-81 (2001).

127. Kaksonen, M., Sun, Y. & Drubin, D.G. A pathway for association of receptors, adaptors, and actin during endocytic internalization. *Cell* **115**, 475-87 (2003).
128. Kaksonen, M., Toret, C.P. & Drubin, D.G. A modular design for the clathrin- and actin-mediated endocytosis machinery. *Cell* **123**, 305-20 (2005).
129. McDonald, K.L. et al. "Tips and tricks" for high-pressure freezing of model systems. *Methods in cell biology* **96**, 671-93 (2010).
130. Bouchet-Marquis, C. et al. Visualization of cell microtubules in their native state. *Biology of the cell / under the auspices of the European Cell Biology Organization* **99**, 45-53 (2007).
131. Masich, S., Ostberg, T., Norlén, L., Shupliakov, O. & Daneholt, B. A procedure to deposit fiducial markers on vitreous cryo-sections for cellular tomography. *Journal of structural biology* **156**, 461-8 (2006).
132. Al-Amoudi, A. & Frangakis, A.S. Structural studies on desmosomes. *Biochemical Society transactions* **36**, 181-7 (2008).
133. Groen, A.C., Maresca, T.J., Gatlin, J.C., Salmon, E.D. & Mitchison, T.J. Functional overlap of microtubule assembly factors in chromatin-promoted spindle assembly. *Molecular biology of the cell* **20**, 2766-73 (2009).
134. Karsenti, E., Nédélec, F. & Surrey, T. Modelling microtubule patterns. *Nature cell biology* **8**, 1204-11 (2006).
135. Walczak, C.E. & Heald, R. Mechanisms of mitotic spindle assembly and function. *International review of cytology* **265**, 111-58 (2008).
136. Brown, K.S. et al. *Xenopus tropicalis* egg extracts provide insight into scaling of the mitotic spindle. *The Journal of cell biology* **176**, 765-70 (2007).
137. Gardner, M.K., Hunt, A.J., Goodson, H.V. & Odde, D.J. Microtubule assembly dynamics: new insights at the nanoscale. *Current opinion in cell biology* **20**, 64-70 (2008).
138. Wang, H.-W. & Nogales, E. Nucleotide-dependent bending flexibility of tubulin regulates microtubule assembly. *Nature* **435**, 911-5 (2005).
139. Al-Bassam, J. & Chang, F. Regulation of microtubule dynamics by TOG-domain proteins XMAP215/Dis1 and CLASP. *Trends in cell biology* (2011).doi:10.1016/j.tcb.2011.06.007
140. Höög, J.L. et al. Electron tomography reveals a flared morphology on growing microtubule ends. *Journal of cell science* **124**, 693-8 (2011).
141. Mitchison, T.J. et al. Bipolarization and poleward flux correlate during *Xenopus* extract spindle assembly. *Molecular biology of the cell* **15**, 5603-15 (2004).

142. Tirnauer, J.S., Salmon, E.D. & Mitchison, T.J. Microtubule plus-end dynamics in *Xenopus* egg extract spindles. *Molecular biology of the cell* **15**, 1776-84 (2004).
143. Tirnauer, J.S., Canman, J.C., Salmon, E.D. & Mitchison, T.J. EB1 targets to kinetochores with attached, polymerizing microtubules. *Molecular biology of the cell* **13**, 4308-16 (2002).
144. Tirnauer, J.S., Grego, S., Salmon, E.D. & Mitchison, T.J. EB1-microtubule interactions in *Xenopus* egg extracts: role of EB1 in microtubule stabilization and mechanisms of targeting to microtubules. *Molecular biology of the cell* **13**, 3614-26 (2002).
145. Yang, G. et al. Architectural dynamics of the meiotic spindle revealed by single-fluorophore imaging. *Nature cell biology* **9**, 1233-42 (2007).
146. Tanaka, T.U. & Desai, A. Kinetochore-microtubule interactions: the means to the end. *Current opinion in cell biology* **20**, 53-63 (2008).
147. Müller-Reichert, T., Mäntler, J., Srayko, M. & O'Toole, E.T. Electron microscopy of the early *Caenorhabditis elegans* embryo. *Journal of microscopy* **230**, 297-307 (2008).
148. Höög, J.L. The 3D Architecture of Interphase Microtubule Cytoskeleton and Functions of Microtubule Plus End Tracking Proteins in Fission Yeast. *Molecular Biology* (2007).
149. Groen, A.C., Coughlin, M. & Mitchison, T.J. Microtubule Assembly in Meiotic Extract Requires Glycogen. *Molecular biology of the cell* 1-47 (2011).doi:10.1091/mbc.E11-02-0158
150. McDonald, K.L. A review of high-pressure freezing preparation techniques for correlative light and electron microscopy of the same cells and tissues. *Journal of microscopy* **235**, 273-81 (2009).
151. Torosantucci, L., De Luca, M., Guarguaglini, G., Lavia, P. & Degrossi, F. Localized RanGTP accumulation promotes microtubule nucleation at kinetochores in somatic mammalian cells. *Molecular biology of the cell* **19**, 1873-82 (2008).
152. Michaeli, W. Plastics processing: an introduction. *Plastics Processing: An Introduction* 211 (1995).at <<http://www.amazon.com/Plastics-Processing-Introduction-Walter-Michaeli/dp/1569901449>>
153. Giboz, J., Copponnex, T. & Mélé, P. Microinjection molding of thermoplastic polymers: a review. *Journal of Micromechanics and Microengineering* **17**, R96-R109 (2007).
154. Müller-Reichert, T., Greenan, G., O'Toole, E.T. & Srayko, M. The elegans of spindle assembly. *Cellular and molecular life sciences : CMLS* **67**, 2195-213 (2010).

## H- Table of Illustrations:

Figure 1 :.....	20
Figure 2 :.....	21
Figure 3 :.....	24
Figure 4 :.....	25
Figure 5 :.....	27
Figure 6 :.....	28
Figure 7 :.....	30
Figure 8 :.....	38
Figure 9 :.....	39
Figure 10 :.....	46
Figure 11 :.....	47
Figure 12 :.....	48
Figure 13 :.....	49
Figure 14 :.....	50
Figure 15 :.....	50
Figure 16 :.....	51
Figure 17 :.....	51
Figure 18 :.....	53
Figure 19 :.....	53
Figure 20 :.....	54
Figure 21 :.....	55
Figure 22 :.....	58
Figure 23 :.....	58
Figure 24 :.....	59
Figure 25 :.....	62
Figure 26 :.....	63
Figure 27 :.....	65
Figure 28 :.....	67
Figure 29 :.....	70
Figure 30 :.....	74
Figure 31 :.....	75

Figure 32 : .....	76
Figure 33 : .....	78
Figure 34 : .....	80
Figure 35 : .....	82
Figure 36 : .....	83
Figure 37 : .....	84
Figure 38 : .....	85
Figure 39 : .....	86
Figure 40 : .....	87
Figure 41 : .....	88
Figure 42 : .....	97
Figure 43 : .....	99
Figure 44 : .....	100
Figure 45 : .....	102
Figure 46 : .....	104
Figure 47 : .....	105
Figure 48 : .....	106
Figure 49 : .....	107
Figure 50 : .....	108
Figure 51 : .....	109
Figure 52 : .....	110
Figure 53 : .....	111
Figure 54 : .....	112
Figure 55 : .....	114
Figure 56 : .....	114
Figure 57 : .....	123
Figure 58 : .....	128
Figure 59 : .....	129
Figure 60 : .....	132
Figure 61 : .....	133
Figure 62 : .....	134

